$t\bar{t}$ Analysis with Taus in the Final State

Carlos Osuna Escamilla

IFAE
Universitat Autònoma de Barcelona
Departament de Física
Edifici Cn E-08193 Bellaterra (Barcelona)

April 2009

Agradecimientos

En primer lugar, mi más profundo agradecimiento va dirigido a mis padres, que me han hecho sentir todo este tiempo su apoyo incondicional y, claro está, por darme esta vida con todas la oportunidades y satisfacciones que me está brindando. La investigación en física de partículas es una de ellas.

Aprecio enormemente la dedicación y el cuidado que Lluisa ha mostrado en todo momento en este trabajo. Gran parte del esfuerzo que hay en esta tesis lleva su huella. Asimismo Martine ha sido una guía y referencia en los momentos en que había que buscar algo más y encontrar nuevas ideas. Con Luca disfruté el placer de compartir el código que con entusiasmo fuimos preparando para el análisis. Y Akira siempre estuvo dispuesto a ayudar con los entresijos del excelente TopView, que tanto nos facilitó las cosas a la hora de realizar nuestro propio análisis. Gracias a Andreu, Mireia, Xavi y Jordi la experiencia con el grid fue mucho más algodonada de lo que se antojaba teniendo en cuenta su fama y mi propia experiencia anterior. Y echando la vista atrás, no podría olvidar los momentos que compartí con los compañeros del trigger, en especial Olga, de quien aprecio su capacidad de contagiar su entusiasmo y motivar el entorno de trabajo.

También le doy las gracias a Ilya, que durante una breve (pero enriquecedora) temporada me enseñó a desenvolverme con el hardware de TileCal, lo que supuso mi primera experiencia en hardware y unas vacaciones de la rutina de la programación de software. A Ulla la pasión por la física que desprende y contagia, que me enseñó un poco más cómo disfrutar con el trabajo. Y en general a todo el grupo de ATLAS del IFAE por la experiencia de trabajar en equipo.

Y un poco más atrás... Antonio y Paco me dieron en Granada mi primera oportunidad en la física de partículas, que marcaría los siguientes años de mi vida y por lo que siempre les estaré agradecido.

Durante estos años he compartido mis días en el IFAE y viajes con compañeros y amigos. Mi primera compañera de despacho, Sigrid, se convirtió en un apoyo esencial y descubrí en ella una maravillosa persona. Le agradezco que valorara mi trabajo, y toda la confianza y motivación que esto me dió. Y más tarde llegaron Estel, siempre dispuesta a ayudar y Volker, por fin! alguien en el IFAE que conoce todos los trucos de `vi`. Gracias chicos por el simpático ambiente de trabajo en el despacho. Si continúo nombrando no puedo más que dejarme a alguien, pero siento que quiero mencionar más personas con quien compartí estos años de estudiante en el IFAE: Nuria, Gabriel, Ana, Eva, Jose, Laia, Manel, Ignasi, Germano, Ester y tantos más. Con muchos de ellos disfruté (junto con Roger que siempre nos daba su preciso parte meteorológico) mezclando pasiones y llevando parte del IFAE a la montaña.

A mi abuelo, unas gracias enormes por estar aquí, aún, en un tiempo distinto al suyo, para que podamos coincidir y enriquecerme con toda su experiencia de vida antes que llevársela consigo. A mi hermana le agradezco no sólo todos estos años de hermanos, además que me vaya a regalar dentro de unos meses un hermoso cambio en mi vida. Y a la pequeña la valentía de despertarse a este mundo y elegirnos como compañía.

Y finalmente a Laura, la felicidad que me produce el caminar junto a ella.

Contents

List of Figures

List of Tables

Chapter 1

Motivation

1.1 Standard Model

The Standard Model [1] [2] [3] [4] is a unified quantum gauge theory that describes the electroweak (through the Quantum Electrodynamics (QED) theory) and the strong (through the Quantum Chromodynamics (QCD) theory) interactions. This theory that best accomodates all experimental observations to date requiring the least parameters, has been probed in many accelerator experiments, some of the most important being those carried out at the Large Electron-Positron[1)] (LEP) collider. The quantity that was measured most accurately at LEP is the mass of the Z boson [5]:

$$m_Z = 91187.6 \pm 2.1 \text{ MeV} \tag{1.1}$$

Table 1.1 presents a list (not exhaustive) of the fundamental particles of the Standard Model and some of their properties. There are two types of particles: the particles that constitute matter, known as matter particles (quarks and leptons) and the particles that mediate the interactions between matter particles (gauge bosons). The matter particles (fermions with spin $\frac{1}{2}$) are clasified into quarks, which suffer strong interactions, and leptons, which do not. The particles that mediate interactions are: one massless photon (γ) for electromagnetic force, massive bosons ($W^{\pm}$ and Z) for weak force and eight massless gluons for strong force.

[1)] LEP was the electron-positron accelerator that operated at CERN from 1989 until 2000. The largest electron-positron accelerator at the time and ever, it was built in the 27 Km long tunnel where the LHC is installed today.

Table 1.1: Fundamental particles in the Standard Model. Mass values are extracted from [6].

Particle Type	Name	Spin	Charge (e)	Mass
quark (fermion)	down (d)	$\frac{1}{2}$	$-\frac{1}{3}$	1.5 to 3.0 MeV
	up (u)	$\frac{1}{2}$	$+\frac{2}{3}$	3.0 to 7.0 MeV
	strange (s)	$\frac{1}{2}$	$-\frac{1}{3}$	95 ± 25 MeV
	charm (c)	$\frac{1}{2}$	$+\frac{2}{3}$	1.25 ± 0.09 GeV
	bottom (b)	$\frac{1}{2}$	$-\frac{1}{3}$	4.2 ± 0.07 GeV
	top (t)	$\frac{1}{2}$	$+\frac{2}{3}$	174.2 ± 3.3 GeV
lepton (fermion)	electron (e)	$\frac{1}{2}$	-1	0.511 MeV
	e-neutrino (ν_e)	$\frac{1}{2}$	0	$<<$ 1 MeV
	muon (μ)	$\frac{1}{2}$	-1	105.66 MeV
	μ-neutrino (ν_μ)	$\frac{1}{2}$	0	$<<$ 1 MeV
	tau (τ)	$\frac{1}{2}$	-1	1.777 GeV
	τ-neutrino (ν_τ)	$\frac{1}{2}$	0	$<<$ 1 MeV
gauge boson	gluon	1	0	0
	photon	1	0	0
	$W^\pm$	1	± 1	80.4 GeV
	Z^o	1	0	91.2 GeV
Higgs boson	H^o	0	0	$>$ 114.4 GeV

1.1.1 Gauge Theories

The successful incorporation of the special theory of relativity [7] into the work of Dirac [8] resulted in a generalised theoretical framework called Quantum Field Theory (QFT), in which particles are treated as excitations of quantum oscillators of the corresponding field. The crucial Noether's theorem [9], proven by Emmy Noether, introduces the concept of symmetries and conservations into the QFT, leading to the development of gauge theories of quantum fields. Noether's theorem states that any conservation law, described by a Lagrangian, is associated to a continuous symmetry in that system, establishing the concept of "local gauge invariance" that is the essence of particles interaction in the Standard Model.

A gauge theory is a theory that is invariant under a set of local transformations, i.e. transformations described by parameters that can vary in space-time. Under a local gauge transformation, the wave function that describes a particle is modified in the following way

$$\psi_o(x) \rightarrow \psi(x) = \psi_o(x) e^{i g_j \alpha_j(x) T_j} \tag{1.2}$$

where g_j is the coupling, $\alpha_j(x)$ is an arbitrary function of space-time and T_j is the generator of the symmetry group.

For each generator of the local transformation the requirement of invariance of the theory forces the introduction of a massless vector boson that is known as a "gauge boson" and is the responsible of the interaction between fermion fields. In this context, an interaction between two fermions is understood as the exchange of a gauge boson. The formalism of the gauge theory was capable of embracing the three forces of the Standard Model. QED was the first to be a successful application of the gauge invariance formalism. With only one transformation belonging to the abelian[2)] group $U(1)$, the symmetry introduces a massless vector particle identified as the photon.

In contrast to QED (or any abelian gauge theory) where the effective coupling constant increases with energy, David Politzer showed [10] in 1973 that the running coupling of a non-abelian gauge theory decreases with energy.

These were the basements of the development of the gauge theory that describes the strong interactions among quarks and gluons, QCD.

Paradoxically, as the coupling constant decreases with energy, the effective coupling was too large at the energies of the experiments running during the 1970's in order to be able to use perturbative expansions. With time, experiments have increased amazingly the energy at which collisions take place, and today, perturbative calculations can be carried out to be compared with the experimental results.

1.1.2 The Electroweak Interaction

The model of Glashow-Weinberg-Salam (GWS) [1] [2] [3] of weak and electromagnetic interactions is a gauge theory based on the "broken" symmetry group $SU(2)_L \otimes U(1)_Y$. A Dirac field, ψ, representing a fermion, can be expressed as the sum of a left-handed component, ψ_L, and a right-handed one, ψ_R.

$$\psi = \psi_L + \psi_R \tag{1.3}$$

where

$$\psi_L = P_L\psi \ , \ P_L = \frac{(1-\gamma_5)}{2} \tag{1.4}$$

$$\psi_R = P_R\psi \ , \ P_R = \frac{(1+\gamma_5)}{2} \tag{1.5}$$

As charged weak interactions are observed in nature only between left-handed fermions, only the left-handed leptons are introduced in the group, $SU(2)$, as a doublet

$$l_L = \begin{pmatrix} \nu \\ e \end{pmatrix}_L \tag{1.6}$$

while the right-handed electron,e_R, transforms as a singlet.

[2)] A gauge theory is abelian when the different transformations of the symmetry group commute with each other.

As the mass term of the Lagrangian mixes the two helicities

$$m\bar{\psi}\psi = m\bar{\psi_L}\psi_R + m\bar{\psi_R}\psi_L \tag{1.7}$$

to treat the left-handed and right-handed helicities as separated particles, fermions have to be massless (until they acquire mass through the spontaneous symmetry breaking mechanism).

The weak isospin group $SU(2)_L$ has three generators: $t_i = \frac{\sigma_i}{2}$ $(i = 1, 2, 3)$ where σ_i are the Pauli matrices. The group $U(1)$ has one generator (hypercharge): $Y = 2(Q - T_3)$ where Q is the charge and T_3 is the third component of the isospin ($T_3 = +\frac{1}{2}$ for neutrino and $T_3 = -\frac{1}{2}$ for the electron).

The gauge bosons corresponding to each generator: $W_\mu^\alpha (\alpha = 1, 2, 3)$ from $SU(2)$ and the neutral field B_μ from $U(1)$ are not the force carriers of the weak field, $W^\pm$ and Z_o (discovered in 1983 by the UA1 [11] [12] and UA2 [13] experiments) nor the carrier of the electromagnetic field, A_μ.

Through the spontaneous symmetry breaking of $SU(2)_L \otimes U(1)_Y$ and the Higgs mechanism (suggested by Peter Higgs [14] and independently by R. Brout and F. Englert [15], see Section 1.1.4) the gauge bosons acquire mass and $SU(2)$ and $U(1)$ get entangled. The carriers of the electroweak force appear as a superposition of the gauge bosons:

$$W_\mu^\pm = \frac{1}{\sqrt{2}}(W_\mu^1 \mp iW_\mu^2) \tag{1.8}$$

$$Z_\mu = \cos\theta_W W_\mu^3 - \sin\theta_W B_\mu \tag{1.9}$$

$$A_\mu = \sin\theta_W W_\mu^3 + \cos\theta_W B_\mu \tag{1.10}$$

$$\tag{1.11}$$

With all pieces in place, the total electroweak Lagrangian has the following components:

$$\mathcal{L}_{SM} = \mathcal{L}_f + \mathcal{L}_G + \mathcal{L}_{SBS} + \mathcal{L}_{YW} \tag{1.12}$$

The first term is the fermionic term

$$\mathcal{L}_f = i\bar{l_L}^T \gamma^\mu D_\mu l_L + i\bar{e_R}\gamma^\mu D_\mu e_R \tag{1.13}$$

where the covariant derivative for a weak isodoublet with weak hypercharge Y is

$$\mathbf{D}_\mu = \left(\partial_\mu + ig_W W_\mu^a T^a + ig_W \tan\theta_W Y B_\mu\right) \tag{1.14}$$

whereas for a singlet (with non-zero electric charge) is

$$D_\mu = (\partial_\mu + ig_W \tan\theta_W Y B_\mu) \tag{1.15}$$

Expanding the fermionic term out and using the physical particles $W_\mu^\pm$, Z_μ and A_μ instead

of W^i_μ and B_μ, the following interactions between fermions and gauge bosons are obtained:

- A coupling between fermions and the charged vector boson $W^\pm$

$$-\frac{g_W}{2\sqrt{2}}\bar{\nu}\gamma^\mu(1-\gamma^5)eW^-_\mu + h.c \tag{1.16}$$

(h.c. stands for hermitian conjugate and is the same term but for the corresponding antiparticles)

- A coupling between the electron and the photon

$$g_W \sin\theta_W \bar{e}\gamma^\mu e A_\mu \tag{1.17}$$

- A coupling between neutrinos and the neutral weak gauge boson

$$-\frac{g_W}{4\cos\theta_W}\bar{\nu}\gamma^\mu(1-\gamma^5)\nu Z_\mu \tag{1.18}$$

- A coupling between the electron and the neutral weak gauge boson

$$\frac{g_W}{4\cos\theta_W}\bar{e}\left(\gamma^\mu(1-\gamma^5) - 4\sin^2\theta_W\gamma^\mu\right)eZ_\mu \tag{1.19}$$

The Lagrangian for the gauge fields of eq. 1.12 is given by:

$$\mathcal{L}_G = -\frac{1}{4}W^i_{\mu\nu}W_i^{\mu\nu} - \frac{1}{4}B_{\mu\nu}B^{\mu\nu} + \mathcal{L}_{GF} + \mathcal{L}_{FP} \tag{1.20}$$

where the field strength tensors are

$$W^i_{\mu\nu} = \partial_\mu W^i_\nu - \partial_\nu W^i_\mu + g\epsilon^{ijk}W^j_\mu W^k_{nu} \tag{1.21}$$

$$B_{\mu\nu} = \partial_\mu B_\nu - \partial_\nu B_\mu \tag{1.22}$$

and $\mathcal{L}_{GF}$ and $\mathcal{L}_{FP}$ are the gauge fixing [16] and Faddeev Popov [17] Lagrangians.

Finally the last two terms, $\mathcal{L}_{SBS}$ and $\mathcal{L}_{YW}$ are the symmetry breaking term and the Yukawa Lagrangian (see Section 1.1.4).

The rest of the three families are added to the formalism as simple copies of the Lagrangian for the electron and its neutrino. Including the quarks to the electroweak theory has one particularity: the mass eigenstates are not eigenstates of the quarks weak interaction. They are mixed according to the Cabibbo-Kobayashi-Maskawa (CKM) matrix [18] [19] (parameterised by three mixing angles and one phase). This effect explains the violation of the Charge-Parity (CP) in the quark sector of the electroweak theory.

1.1.3 QCD and Strong Interactions

QCD, the theory of the strong interactions in the quark model, is based on the symmetry group $SU(3)_C$, where notation refers to the three possible colour states of the quarks. Only quarks carry colour charge and therefore are the unique matter particles within the Standard Model that interact with the strong force. The gauge invariance of the Lagrangian introduces eight massless coloured gluons, g_α (the mediators of the strong interaction).

QCD is developed as a gauge theory requiring the invariance principle like QED, with the particularity that $SU(3)$ obeys a non-abelian algebra. The covariant derivative acting on the quark field due to the strong force is:

$$\mathbf{D}q \equiv (\partial_\mu - i\alpha_S \lambda_a G^a_\mu)q \tag{1.23}$$

where

$$q = \begin{pmatrix} q_1 \\ q_2 \\ q_3 \end{pmatrix} \tag{1.24}$$

$$q_i = \text{quark fields ; } i = 1,2,3 \tag{1.25}$$

$$\alpha_S = \text{strong coupling constant} \tag{1.26}$$

$$\lambda_a = SU(3) \text{ generators; } a = 1,...,8 \tag{1.27}$$

$$G^a_\mu = \text{gluon fields; } a = 1,...,8 \tag{1.28}$$

The Lagrangian term for the gauge field (eq.1.20) for QCD is

$$F^a_{\mu\nu} F^{\mu\nu}_a \tag{1.29}$$

where $F^a_{\mu\nu}$ is the gluon field strength

$$F^a_{\mu\nu} = \partial_\mu G^a_\nu - \partial_\nu G^a_\mu + \alpha_S f^{abc} G_{\mu b} G_{\nu c} \tag{1.30}$$

and f^{abc} are the structure constants of the $SU(3)_C$ group.

Once expanded, the gauge field term contains (unlike QED) a three-gluons term and a four-gluons term. These self-interaction gluon vertices are characteristic of a non-abelian theory.

The self coupling of gluons is the reason of a particular property of QCD theory: the asymptotic freedom and confinement, that is at the same time the reason of the non-observation of free quarks. The asymptotic freedom behaviour of QCD establishes that the strong coupling, α_s, decreases with energy and vanishes at asymptotically high energies (see Figure 1.1).

Due to the asymptotic freedom property of QCD, when a quark is isolated from its original hadron, as for example due to a collision with another particle, the isolated quark tends to group wih other quarks to form a colourless particle, creating new mesons and hadrons. This process is known as “hadronisation” and its result, the collection of new particles, measured in

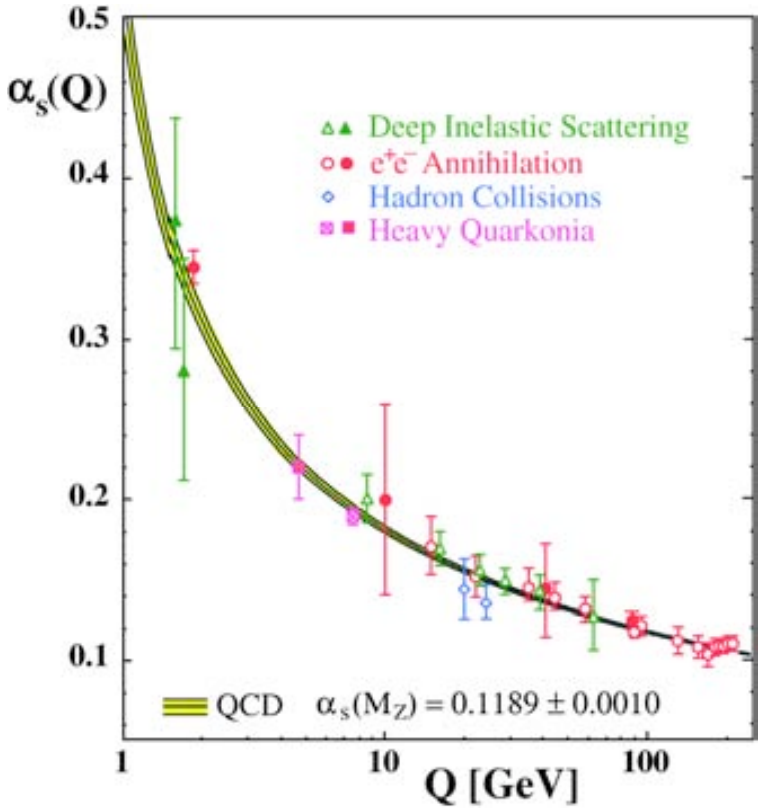

Figure 1.1: Running of strong coupling constant, α_S. Open symbols indicate NLO and filled symbols NNLO QCD calculations (Ref. [20]).

the experiments is called a "jet" [21].

1.1.4 Spontaneous Symmetry Breaking and the Higgs Mechanism.

Although the unbroken gauge theories of the Standard Model predicted the existence of gauge bosons in an elegant manner, the emerging gauge bosons must be massless. In contrast, the only observed massless boson particles are the photons. Therefore, symmetry must be broken in order to generate masses of the gauge bosons. A simple mass term violating the gauge symmetry could be added to the Lagrangian for the gauge boson, although the theory would loose the elegance acquired in its formalism. On the contrary, the called 'spontaneous symmetry breaking' is able to generate the gauge massive bosons while keeping the symmetry under a set of local gauge transformations. The breaking of the symmetry comes from the fact that the lowest energy state (the vacuum state) is not a singlet of the gauge symmetry.

The spontaneous symmetry breaking introduces a scalar doublet field into the Lagrangian of the theory

$$\mathcal{L} = \partial_\mu \Phi^\dagger \partial^\mu \Phi - V(\Psi) \tag{1.31}$$

where the potential $V(\Phi)$ is

$$V(\Phi) = \mu^2 \Phi^\dagger \Phi + \lambda |\Phi^\dagger \Phi|^2 \tag{1.32}$$

Under the conditions $\lambda > 0$ and $\mu^2 < 0$, the potential has a minimum at (see Figure 1.2)

$$\Phi^\dagger \Phi = -\frac{\mu^2}{2\lambda} \equiv \frac{\upsilon^2}{2} \tag{1.33}$$

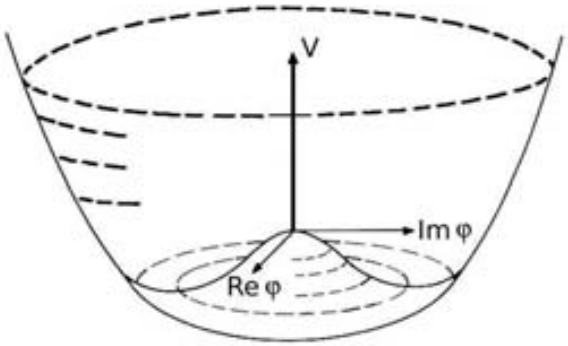

Figure 1.2: The spontaneous symmetry breaking potential

There is an infinite number of states with the same ground-state energy. By choosing one particular solution of the potential, the symmetry is broken. Expanding the scalar field around its vacuum expectation value

$$\Phi = \frac{1}{\sqrt{2}} \left(\frac{\mu}{\sqrt{\lambda}} + H + i\phi \right) \tag{1.34}$$

The mass term of the Higgs boson and a new massles particle called 'Goldstone boson' appear

in the potential

$$V = \mu^2 H^2 + \mu\sqrt{\lambda}(H^3 + \phi^2 H) + \frac{\lambda}{4}(H^4 + \phi^4 + 2H^2\phi^2) + \frac{\mu^4}{4\lambda} \tag{1.35}$$

The addition of the scalar field into the Lagrangian completes the two missing terms of the electroweak Lagrangian (Eq. 1.12)

$$\mathcal{L}_{SBS} = (D_\mu \Phi)^\dagger D^\mu \Phi - V(\Phi) \tag{1.36}$$

and

$$\mathcal{L}_{YW} = \lambda_e \bar{l}_L \Phi e_R + \lambda_\mu \bar{q}_L \tilde{\Phi} u_R + \lambda_u \bar{q}_L \Phi d_R + h.c \tag{1.37}$$

where

$$l_L = \begin{pmatrix} \nu_L \\ e_L \end{pmatrix} ; \;\; q_L = \begin{pmatrix} u_L \\ d_L \end{pmatrix} ; \;\; \tilde{\Phi} = i\sigma_2 \Phi^* \tag{1.38}$$

Introducing the expansion of the scalar around its vacuum (Eq. 1.34) into $\mathcal{L}_{SBS}$ and $\mathcal{L}_{YW}$, the fermions, gauge bosons and Higgs boson acquire their mass:

$$M_W = \frac{g_W \upsilon}{2} ; \;\; M_Z = \frac{\sqrt{g_W^2 + g_W'^2}\upsilon}{2} ; \;\; M_H = \sqrt{2}\mu \tag{1.39}$$

$$m_e = \lambda_e \frac{\upsilon}{\sqrt{2}} ; \;\; m_u = \lambda_u \frac{\upsilon}{\sqrt{2}} ; \;\; m_d = \lambda_d = \frac{\upsilon}{\sqrt{2}} \tag{1.40}$$

With some requirements on unitarity [22] the theoretical limit on the Higgs mass is

$$M_H < 860 \text{ GeV} \tag{1.41}$$

On the other hand LEP results [23] set a lower limit to the Higgs mass at 114.4 GeV at 95% confidence level.

1.1.5 The Top Quark

The top quark discovery was announced by CDF and DØ experiments in 1995 [24] [25] and since then all direct measurements of production and decay of the top quark have been made at Tevatron. The top mass measurement reported by the Particle Data Group (PDG), using a combination of published results from Run-I and Run-II at Tevatron, is $m_t = 171.2 \pm 2.1$ GeV/c^2 [6]. The most recent value provided by the Tevatron Electro Weak Working Group yields is $m_t = 172.6 \pm 1.4$ GeV/c^2 [26]. Next section summarizes the properties of the top quark with the different production and decay modes.

Production and Decay of the Top Quark

In hadron colliders there are two mechanisms of production of top quarks: $t\bar{t}$ pairs which are produced through QCD interactions, and the single tops which are produced through the weak

interaction. Thus the $t\bar{t}$ and single top production modes are sensitive to different physics effects.

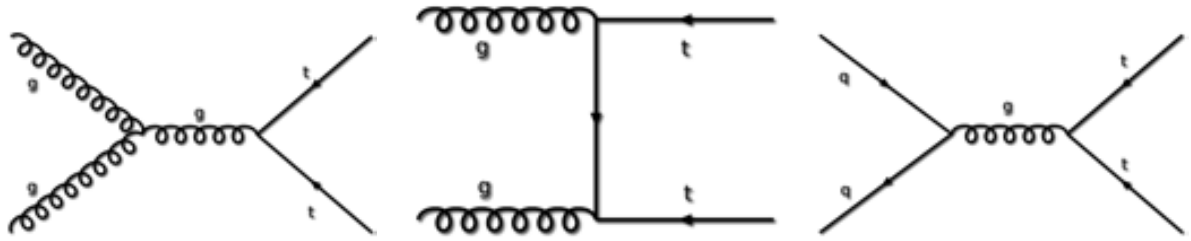

(a) (b) (c)

Figure 1.3: Top production processes at lowest order: gluon-gluon scattering diagrams (a) and (b), and quark-quark scattering diagram (c).

The production of a $t\bar{t}$ pair in a proton-proton collision is produced through gluon-gluon and quark-antiquark scattering (Figure 1.3). The relative importance of both mechanisms depends on the center of mass energy. While at the Tevatron the production is kinematically restricted to the quark-quark scattering, at the energies of the LHC, the gluon scattering process represents 90% of the cases. The large top quark mass (m_t) ensures that top quark production is a short-distance process, and that the perturbative expansion, given by a series in powers of the small parameter $\alpha_s(m_t)$, converges rapidly.

The total cross section for top quark pair production depends on the center of mass energy squared s_{had} and the top quark mass m_t [27]. It is obtained through

$$\sigma_{pp\to t\bar{t}X}(s, m_t^2) = \sum_{i,j=q,\bar{q},g} \int_{4m_t^2}^{s_{had}} d\hat{s} L_{ij}(\hat{s}, s_{had}, \mu_f^2) \hat{\sigma}_{ij\to t\bar{t}}(\hat{s}, m_t^2, \mu_f^2, \mu_r^2) \tag{1.42}$$

being $L_{ij}(\hat{s}, s_{had}, \mu_f^2)$ the parton luminosities defined as

$$L_{ij}(\hat{s}, s_{had}, \mu_f^2) = \frac{1}{s_{had}} \int_{\hat{s}}^{s_{had}} \frac{ds}{s} f_{i/p}\left(\mu_f^2, \frac{s}{s_{had}}\right) f_{j/p}\left(\mu_f^2, \frac{\hat{s}}{s}\right) \tag{1.43}$$

where $f_{i,p}(\mu_f^2, x)$ are the parton distribution functions (PDF) of the proton at a factorization scale μ_f; μ_f and μ_r are the renormalization and factorization scales and $\hat{\sigma}$ is the partonic cross section.

To obtain a theoretical prediction of the cross section to a certain order in perturbation theory it is common practice to identify the factorization scale with the renormalization scale (i.e. $\mu_f = \mu_r$) and to estimate the effect of uncalculated higher orders by varying μ in the interval $[m_t/2, 2m_t]$. The uncertainties due to PDFs are obtained from experimental data, and are computed from the variation of the cross section with respect to the parameters of the global fit [28] [29].

The cross section for $t\bar{t}$ production in proton-proton collisions at $\sqrt{s} = 14$ TeV calculated up to NLO order including NLL soft gluon resummation (assuming a top quark mass of 171 GeV and using the MRST 2006 NNLO parton densities [29]) is $\left(924\ ^{+114}_{-110}\ ^{+12}_{-12}\right)$ pb [30]. The theoretical

errors correspond to the uncertainty due to the renormalization scale (varying the scale over $m_t/2 < \mu < 2m_t$) and to the PDF uncertainty, calculated using the 30 different MRST 2006 NNLO eigensets (the kinematics uncertainty is not shown because it is much smaller than the scale uncertainty).

The value of the cross section calculated up to NNLO order including NNNLL resummation is $\left(994 \pm 5\ ^{+81}_{-52}\ ^{+13}_{-13}\right)$ pb where the theoretical errors correspond to the kinematics errors, the uncertainty due to the scale and the PDF uncertainty. The uncertainty due to the scale is considerably reduced compared to the NLO calculation.

The effect of PDF errors accounts for a few percent uncertainty in the cross section value, while varying the scale by a factor two, the uncertainty obtained is about 8%. Figure 1.4 shows the exact NLO and approximate NNLO top quark cross sections as a function of the top quark at LHC (with $\sqrt{s} = 14$ TeV) using the MRST 2006 PDFs. The plot shows for each order the central result with $\mu = m$ as well as the range of the scale uncertainty between the lower ($\mu = 2m$) and upper ($\mu = m/2$) curves. The NLO and NNLO curves exhibit a large sensitivity to the top mass, what can be used as a measurement of the consistency of the Standard Model, as any disagreement between the measurements of the cross section of $t\bar{t}$ and the top mass may indicate the presence of new physics.

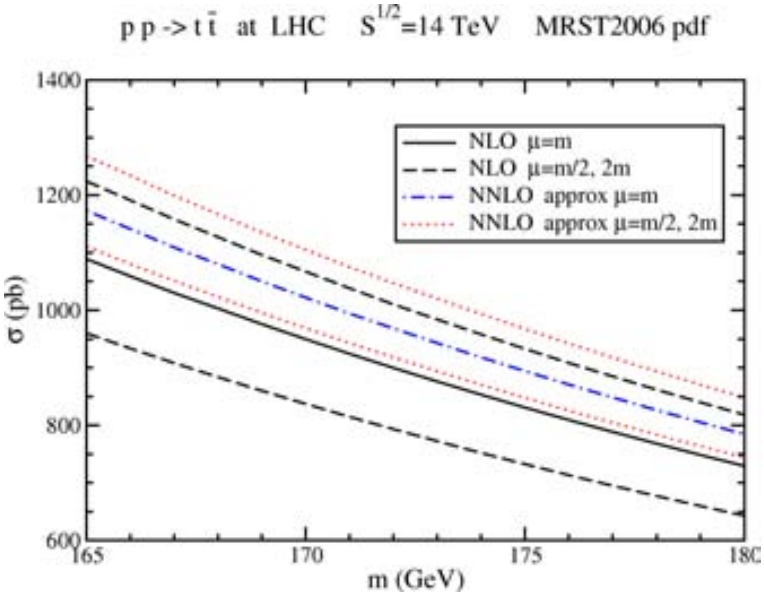

Figure 1.4: The NLO and NNLO top cross sections at the LHC using the MRST 2006 NNLO PDFs.

The existence of a single top production was observed for the first time in March 2009 [31] [32]. The single top or antitop is produced through the weak interaction with a cross section that is directly proportional to the V_{tb} CKM matrix element. Recent analyses on single top at Tevatron determine a value of the CKM matrix element $|V_{tb}| = 1.3 \pm 0.2$ by DØ collaboration [33] and $|V_{tb}| = 0.88 \pm 0.16$ by CDF collaboration [34].

The single top production has a much lower (compared to $t\bar{t}$ pair production) cross section, and it has three different channels of production: t-channel (also called "W-gluon fusion"), s-channel and W-top associated production (or just "Wt"), shown in Figure 1.5.

The theoretical cross sections [35] at the NLO for the three single top production processes (assuming a top quark mass $m_t = 171.4$ GeV and using the MRST 2004 parton densities [36]) are summarized at Table 1.2.

Table 1.2: Theoretical calculations at the NLO of the single top cross sections for the three production modes. Uncertainties are due to (in this order) the scale dependence, the top mass uncertainty (2.1 GeV), and the PDF uncertainty.

channel	**t-channel**	**s-channel**	**Wt**
NLO cross section (pb)	$150 \pm 5 \pm 2.5 \pm 3$	$7.80^{+0.58\ +0.36}_{-0.48\ -0.33} \pm 0.14$	$43.5 \pm 4.5 \pm 1.5 \pm 1.0$

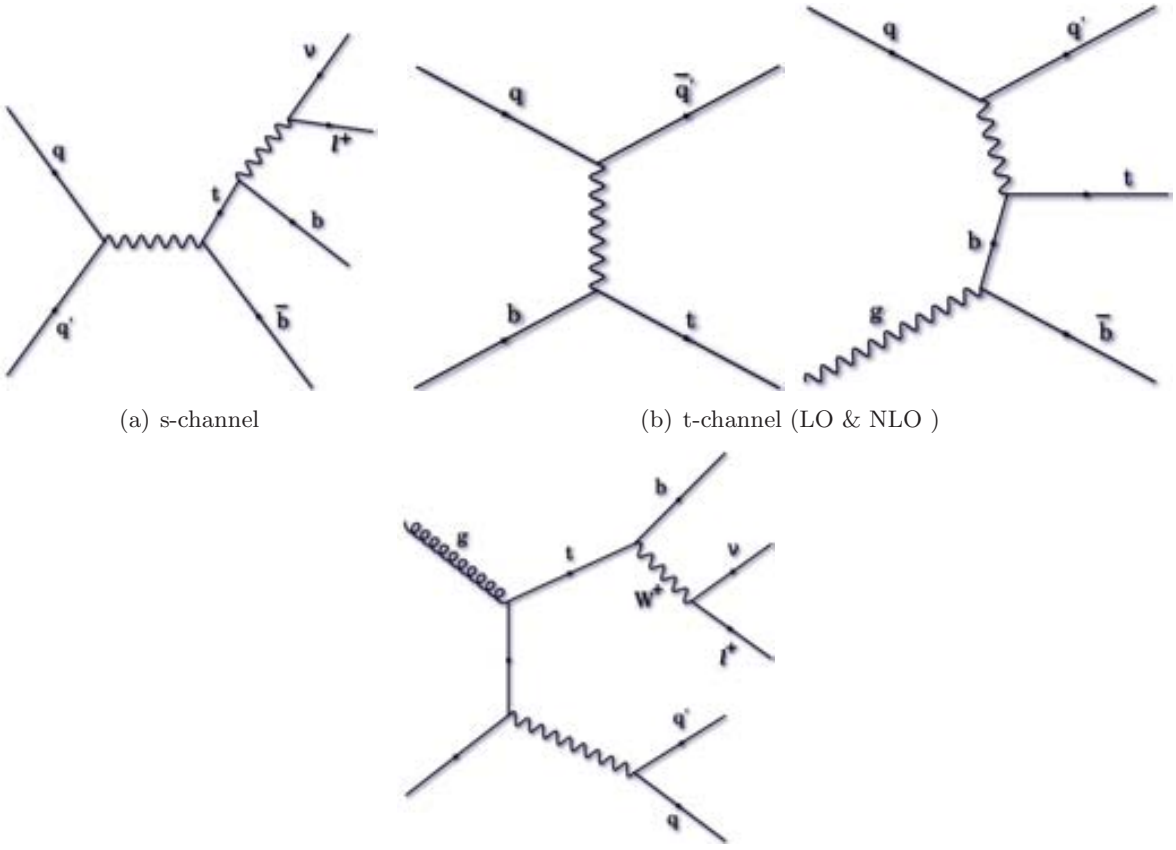

(a) s-channel

(b) t-channel (LO & NLO)

(c) Wt

Figure 1.5: Feynman diagram for single top production.

Once produced, the top quark decays quickly due to its very large mass. The top quark decays almost exclusively to a b quark and a real W boson with branching ratio ~ 0.999. The

W boson subsequently can decay leptonically ($W \rightarrow l\nu_l$, where l is e, μ or τ) or hadronically ($W \rightarrow q_1\bar{q_2}$ where (q_1, q_2) are (u,d) or (c,s)). The branching ratio of the W decaying hadronically is 67.6% while the branching ratio to decay leptonically is 32.6% (aproximately one third of it to each lepton).

1.2 Beyond the Standard Model Searches

Although the Standard Model is a successful theory that has been tested with very high precision in a wide range of experiments, there are still some weak points and unanswered questions which the different "Beyond Standard Model" models try to sort out:

- The hierarchy problem.
- The missing dark matter problem.

  What is the source (within the Standard Model) of the missing dark matter that would account for the vast majority of the mass in the observable universe? Several observed phenomena confirmed the presence of such dark matter, like rotational speeds of galaxies, orbital velocities of galaxies in clusters, gravitational lensing of background objects by galaxy clusters, etc.
- The cosmological constant problem.

  If the universe is described by the Standard Model theory up to the Planck scale, a cosmological constant of the order of M_P^4 is expected, while it is measured to be a factor 10^{-120} this value.
- The strong CP problem.

  The small CP violating term in the CKM matrix does not explain by itself the complete dominance of matter over antimatter in the universe.

1.2.1 The Hierarchy Problem

The hierarchy problem [37] [38] is one of the most serious drawbacks of the SM and appears when one tries to extend the validity of the SM to describe physics at energies higher than the electroweak scale, near the Planck scale, $M_P = (8\pi G_{Newton})^{-\frac{1}{2}} = 1.22 \cdot 10^{19}$ GeV, where quantum gravitational effects become important. The fact that the ratio $\frac{M_P}{M_W}$ is so huge (16 orders of magnitude) constitutes the ground of the hierarchy problem.

The Standard Model complex scalar Higgs field obeys the classical potential

$$V = m_H^2|H|^2 + \lambda|H|^4 \tag{1.44}$$

with the vacuum expectation value (VEV), $\langle H \rangle = \sqrt{-m_H^2/2\lambda}$. Since it is experimentally known that $\langle H \rangle$ is approximately 174 GeV, then m_H^2 is very roughly of the order $-(100\text{ GeV})^2$. But the

hierarchy problem lies in the enormous quantum corrections to this mass from the virtual effects of any particle that couples to the Higgs field (with a coupling constant that is proportional to its mass).

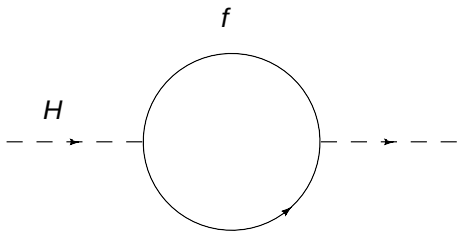

Figure 1.6: A fermion loop quantum correction to the Higgs squared mass m_H^2.

Figure 1.6 shows the quantum correction to m_H^2 from a fermion loop with mass m_f. From the Lagrangian term that couples the Higgs field to the fermion $-\lambda_f H\bar{f}f$, follows the one loop quantum correction from Figure 1.6

$$\Delta m_h^2 = \frac{|\lambda_f|^2}{16\pi^2}\left[-2\Lambda_{UV}^2 + \mathcal{O}\left(m_f^2 \ln\left(\frac{\Lambda_{UV}}{m_f}\right)\right)\right] \tag{1.45}$$

where Λ_{UV} is an ultraviolet cutoff introduced to regulate the loop integral (i.e. the energy scale at which new physics comes into play modifying the high energy behaviour of the Standard Model theory). If the Standard Model is considered a valid effective theory until the gravitational effects become important, the ultraviolet cutoff Λ_{UV} is of the order of the Planck scale M_P, and the quantum corrections become 30 orders of magnitude larger than the estimated value $m_H^2 \approx -(100\text{ GeV})^2$.

Moreover, quarks, leptons and the electroweak gauge bosons Z^o, $W^{\pm}$ of the Standard Model acquire their masses through the vacuum expectation value of the Higgs field, and therefore, the entire mass spectrum of the Standard Model is sensitive to the cutoff Λ_{UV}.

Unless there is an incredible fine-tuning cancellation between all the possible quadratic radiative corrections of the form of Equation 1.45 (in order to cancel the common factor $\frac{M_P}{M_W} \approx O(10^{16})$) the Standard Model needs to be extended. There exist several theories that solve the hierarchy problem, like Extra Dimensions, Technicolour, Little Higgs models or Supersymmetry.

If we suppose there exists a new heavy complex scalar particle S with mass m_s that couples to the Higgs with a Lagrangian term $-\lambda_S|H|^2|S|^2$, then the loop represented in Figure 1.7 gives a correction to the Higgs mass

$$\Delta m_H^2 = \frac{|\lambda_S|^2}{16\pi^2}\left[2\Lambda_{UV}^2 + \mathcal{O}\left(m_S^2 \ln\left(\frac{\Lambda_{UV}}{m_S}\right)\right)\right] \tag{1.46}$$

With this assumption, the term Λ_{UV}^2 of Equations 1.45 and 1.46 cancels out. That is the idea behind Supersymmetry, that will be introduced in more detail in the next section.

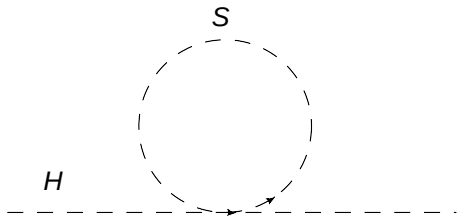

Figure 1.7: A scalar loop quantum correction to the Higgs squared mass m_H^2.

1.2.2 Supersymmetry

Supersymmetry [39] [40] [41] is an elegant theory for physics beyond de Standard Model. The main success of the theory is the natural protection of the Higgs mass from quadratically diverging radiative corrections, solving the hierarchy problem. It also provides consistency with the grand unification of the strong and electroweak forces into a simple grand unified theory, as well as a good candidate for dark matter. Supersymmetry also seems to be essential for making a consistent quantum theory of gravity based on string theory [42].

The theory assumes that for each fermion of the Standard Model with a Lagrangian term that couples to the Higgs field, responsible of the diverging quantum corrections to its mass (Eq. 1.45), there exists an equivalent boson that will introduce a quantum correction with a relative minus sign (Eq. 1.46), providing a systematic cancellation of the dangerous contributions to Δm_H^2. The operator Q that generates the symmetry transformation turns a bosonic state into a fermionic state and vice versa.

$$Q\,|Boson\rangle = |Fermion\rangle\,, \qquad\qquad Q\,|Fermion\rangle = |Boson\rangle \tag{1.47}$$

In the supersymmetric extension of the Standard Model, each of the known fundamental particles must have a superpartner with spin differing by 1/2 unit. The spin-0 superpartners of leptons and quarks are generally called *sleptons* and *squarks*. For example, superpartners of the left-handed and right-handed electron are called left- and righ- handed *selectron* and denoted as $\tilde{e}_L$ and $\tilde{e}_R$

All the supermultiplets of the minimal viable extension of the Standard Model, the Minimal Supersymmetric Standard Model (MSSM) [43], are summarized in Table 1.3, while Table 1.4 does it for the gauge supermultiplets.

Table 1.3: Chiral supermultiplets in the Minimal Supersymmetric Standard Model.

Names		spin 0	spin 1/2	$\mathbf{SU(3)_c, SU(2)_L, U(1)_\gamma}$
squarks, quarks	Q	$\left(\tilde{u}_L \quad \tilde{d}_L\right)$	$(u_L \quad d_L)$	$\left(3, 2, \frac{1}{6}\right)$
(x3 families)	$\bar{u}$	$\tilde{u}_R^*$	$\tilde{u}_R^\dagger$	$\left(\bar{3}, 1, -\frac{2}{3}\right)$
	$\bar{d}$	$\tilde{d}_R^*$	$d_R^\dagger$	$\left(\bar{3}, 1, 1\frac{1}{3}\right)$
sleptons, leptons	L	$(\tilde{\nu} \quad \tilde{e}_L)$	$(\nu \quad e_L)$	$\left(1, 2, -\frac{1}{2}\right)$
(x3 families)	$\bar{e}_R$	$\tilde{e}_R^*$	$e_R^\dagger$	$(1, 1, 1)$
Higgs, higgsinos	H_u	$(H_u^+ \quad H_u^o)$	$\left(\tilde{H}_u^+ \quad \tilde{H}_u^o\right)$	$\left(1, 2, +\frac{1}{2}\right)$
	H_d	$(H_d^o \quad H_d-)$	$\left(\tilde{H}_d^o \quad \tilde{H}_d-\right)$	$\left(1, 2, -\frac{1}{2}\right)$

Table 1.4: Gauge supermultiplets in the Minimal Supersymmetric Standard Model.

Names	spin 1/2	spin 1	$\mathbf{SU(3)_c, SU(2)_L, U(1)_\gamma}$
gluino, gluon	$\tilde{g}$	g	$(8, 1, 0)$
winos, W bosons	$\tilde{W}^\pm \quad \tilde{W}^o$	$\mathrm{W}^\pm \quad W^o$	$(1, 3, 0)$
bino, B boson	$\tilde{B}^o$	B^o	$(1, 1, 0)$

If Supersymmetry were unbroken, then there would have to be superpartners with masses exactly equal to the Standard Model particles, and therefore extremely easy to detect. As none of the superpartners have been discovered, Supersymmetry is a broken symmetry in the vacuum state.

Assuming $\Lambda_{UV} \approx M_P$, the masses of at least the lightest few superpartners should be at most about 1 TeV or so, in order to provide a Higgs vacuum expectation value resulting in $m_W, m_Z = 80.4, 91.2$ GeV without miraculous cancellations. This is the best reason to believe that Supersymmetry, if it exists, will be discovered at the Large Hadron Collider.

1.2.3 $t\bar{t}$ as Background to Supersymmetry Searches

Since the baryonic and leptonic numbers do not seem to be violated in nature (the most obvious experimental constraint comes from the non-observation of the proton decay [6]) the existence of terms in the supersymmetric Lagrangian that violate those numbers are rather disturbing.

A new symmetry, "*R-parity*" can be added to the theory in order to eliminate the B and L violating terms from the renormalizable superpotential. R-parity conserved quantum numbers are defined as:

$$P_R = (-1)^{3(B-L)+2s} \tag{1.48}$$

for each particle in the theory. Particles of the Standard Model carry R-parity number $P_R = +1$ while sparticles have $P_R = -1$. The R-parity conservation assumption in the supersymmetric

theory has three important phenomenological consequences:

- The lighest sparticle (LSP) must be stable (as it can not decay into particles with $P_R = 1$). If the LSP is electrically neutral, then it can only interact weakly with ordinary matter, turning into a candidate for non-baryonic dark matter.
- Each sparticle other than the LSP must eventually decay into a state that contains an odd number of LSPs
- In a collider experiment, sparticles can only be produced in even numbers.

If the R-parity is conserved the typical signature (Figure 1.8) of a supersymmetric event produced in a pp collision will contain large missing energy (due to the presence of neutrinos and the LSP in the event) and also a large multiplicity of jets (due to a long decay chain with quarks and leptons in the final state).

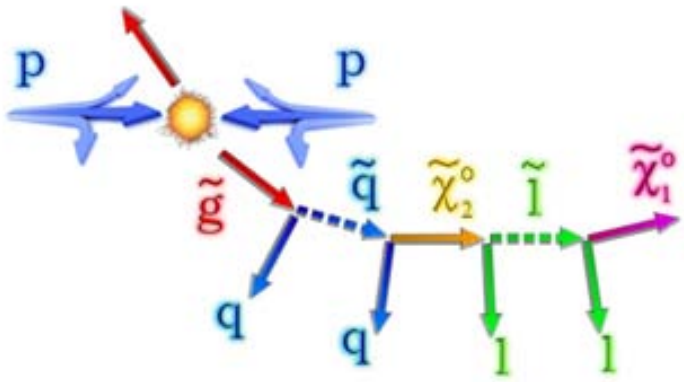

Figure 1.8: An example of supersymetric particles production and the decay chain.

Any discovery of new physics beyond the Standard Model can only be claimed when the Standard Model processes are understood and under control. In that sense, the $t\bar{t}$ production is the dominant background for the signatures produced by a large class of Supersymmetry models, as it provides a similar environment, with large jet multiplicity and missing energy. Here the importance of a dedicated study of the $t\bar{t}$ process, not only as a signal subject but rather as a background to Supersymetry searches.

While the semileptonic (where the lepton is an electron, muon or a tau that decays leptonically) channels of the $t\bar{t}$ production

$$t\bar{t} \rightarrow W\,(\rightarrow l\nu)\,b \quad W\,(\rightarrow q\bar{q})\,b \tag{1.49}$$

are important backgrounds to Supersymmetry events with a hard lepton in the final state, the

semileptonic channel with a tau that decays hadronically

$$t\bar{t} \rightarrow W\,(\rightarrow \tau\,[\rightarrow hadrons\ \ \nu_\tau]\,\nu)\,b \quad W\,(\rightarrow q\bar{q})\,b \tag{1.50}$$

is an important irreducible background to Supersymmetry events with no hard leptons in the final state. Figure 1.9 shows the missing transverse energy distribution for the ATLAS experiment applying the cuts for SUSY searches with no lepton analysis [44]. The plot shows that the major process that contributes to the SM background is the $t\bar{t}$ up to $\not\!\!E_T \sim 300$ GeV, where W and Z processes become also relatively important. If no τ veto is applied, about 65% of the total $t\bar{t}$ background in the no lepton mode corresponds to events containing one τ.

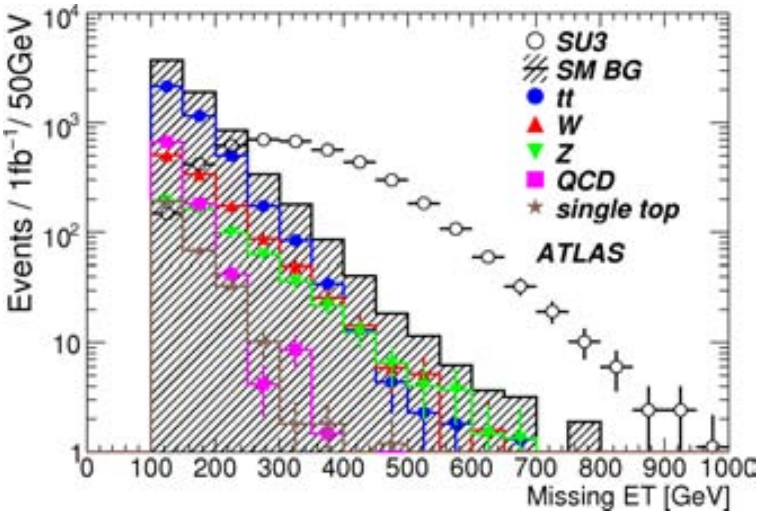

Figure 1.9: Missing transverse energy distribution for ATLAS detector after applying the analysis cuts for SUSY searches in the no lepton mode for an integrated luminosity of 1 fb^{-1}. The open circles show the SUSY signal (see Section 4.9) and the shaded histogram shows the sum of all Standard Model backgrounds.

In that sense the understanding of this last channel is of special importance for Supersymetry searches in the mode with no leptons in the final state.

In addition, if within a sample of $t\bar{t}$ events there is contamination coming from new physics, the ratio $r_\tau = \frac{t\rightarrow\tau\nu b}{t\rightarrow l\nu b}$ may be sensitive to the specific supersymmetric model (or set of parameters of a given model) and significantly different from 1, as the Standard Model predicts. This argument will be further explained in the following section.

1.2.4 Taus in Supersymmetry

Sleptons in Supersymmetry (SUSY) can be produced either directly or in the decay of other sparticles, particularly the electro-weak gauginos. Their decays often give final states containing e, μ and τ. The small Yukawa coupling of the first two generations leads to expect that the supersymmetric partners of the electron and muon, the selectron and smuon, have about the

same masses and couplings.

The larger Yukawa coupling of the $\tilde{\tau}$'s affects the mixing of the two mass eigentstates of the left and right handed $\tilde{\tau}$, $\tilde{\tau}_L - \tilde{\tau}_R$ as well as the renormalization group evolution of the soft mass terms and the $\tilde{\chi}\tilde{\tau}\tau$ couplings, the $\tilde{\chi}$ being mixtures of the electroweak gauginos and the higgsinos. Thus the physics of staus is generally quite different from that of selectrons and smuons.

The primary SUSY production processes at the LHC are $pp \to \tilde{q}\tilde{g}, \tilde{q}\tilde{q}, \tilde{g}\tilde{g}$. In each case, the decays proceed via $\tilde{q} \to q'\tilde{\chi}_1^{\pm}$ or $q\tilde{\chi}_2^o$ (or $\tilde{q}_R \to q\tilde{\chi}_1^o$); $\tilde{g} \to q\bar{q}'\tilde{\chi}_1^{\pm}$ or $q\bar{q}\tilde{\chi}_2^o$; and $g \to \bar{t}\tilde{t}_1$ or $\bar{b}\tilde{b}_1$ and their charge conjugate states, generally producing high transverse energy (E_T) jets and gaugino pairs.

The decay chain of the gaugino pairs, $\tilde{\chi}_1^o\tilde{\chi}_2^o$, $\tilde{\chi}_1^{\pm}\tilde{\chi}_2^o$ and $\tilde{\chi}_2^o\tilde{\chi}_2^o$, will depend on the particular SUSY model and the parameter space chosen. The decay into staus is specially enhanced at large $\tan\beta$ values (defined as the ratio of the vacuum expectation values of the two neutral Higgses). For the stau-neutralino ($\tilde{\tau}_1 - \tilde{\chi}_1^o$) coannihilation region of the mSUGRA[3)] model (largely used at LHC studies), characterized by a mass difference (ΔM) between $\tilde{\tau}_1$ and $\tilde{\chi}_1^o$ of about 5-15 GeV, the branching ratio of $\tilde{\chi}_2^o \to \tau\tilde{\tau}$ is about 97% for $m_{\frac{1}{2}} = 360$ GeV and $\tan\beta = 40$, and still dominant in the entire coannihilation region. The same is true for the $\tilde{\chi}_1^{\pm} \to \nu\tilde{\tau}_1$ decay mode.

In conclusion, as mentioned in Section 1.2.3, in SUSY models, the tau physics will be generally quite different from that of electrons and muons, and if new physics enhances the τ channels with respect to the rest of the lepton channels, the contamination of new physics events in the $t\bar{t} \to W(qq')W(\tau_{had}\nu)b\bar{b}$ analysis will cause a deviation of the measured ratio $r_\tau = \frac{t\to\tau\nu b}{t\to l\nu b}$ from 1 that may indicate the existence of new physics at the TeV scale and help in the understanding of the nature of the physics beyond the Standard Model.

1.2.5 Charged Higgs Searches

Charged Higgs bosons ($H^{\pm}$) are naturally predicted in many non-minimal Higgs scenarios, such as Two Higgs Doublets Models (2HDM) and models with Higgs triplets including Little Higgs models. Their discovery would be a definite signal for the existence of new physics beyond the Standard Model, and possibly the first experimental evidence for the Minimal Supersymmetric Standard Model (MSSM) if it is realised in nature, and the Supersymmetry mass scale is high enough that sparticles escape discovery.

Assuming that all supersymmetric particles are heavy enough not to play an important role in the phenomenology of $H^{\pm}$ decay, the MSSM charged Higgs will only decay into SM particles. The decay pattern is determined by the Yukawa couplings and the value of $\tan\beta$.

Charged Higgs Decay Modes

For large $\tan\beta$ values, as a result of the strong enhancement of the couplings to down-type fermions, $H^{\pm}$ with $m_{H^{\pm}} > m_{top}$ will decay into tb pairs wih a branching ratio of almost 85%

[3)] The minimal supergravity model (mSUGRA) [45] [46] [47] or CMSSM, has the MSSM embedded in a supergravity framework. Gravity provides the symmetry breaking of the supersymmetric model. mSUGRA is a widely used model due to its predictive capability requiring only four parameters and a sign.

and into $\tau\nu$ with a branching ratio of 15%. For $H^{\pm}$ with $m_{H^{\pm}} < m_{top}$, the branching ratio of $H^{\pm} \to \tau\nu$ is 100%.

On the other hand, for small $\tan\beta$ values, $\tan\beta \lesssim 5$, the pattern is more complicated. For $m_H^{\pm} > m_{top}$, the charged Higgs will decay mainly into tb. In addition, decays into Wh final states play also an important role since they can reach the level of several ten percent for certain m_H^{+} values, leading to a significant reduction of the dominant branching ratio into $\tau\nu$ states. For $H^{\pm}$ with $m_{H^{\pm}} < m_{top}$ the main decay mode is $H^{\pm} \to \tau\nu$ and the $H^{\pm} \to cs$ starts being non negligible.

Charged Higgs Production

If the charged Higgs is lighter than the top quark, top quark decays would be a good source of charged Higgs production through $pp \to t\bar{t}, t \to H^{+}b$, since top quarks will be produced with very large rates at the LHC. In this mass range, the decay channel $H^{\pm} \to \tau\nu$ is the dominant decay mode. For low $\tan\beta$ this decay channel is complemented with $H^{\pm} \to cs$.

In the case of a charged Higgs heavier than the top quark, the main charged Higgs production is through the $2 \to 3$ process $gg \to tbH^{\pm}$ and the $2 \to 2$ process $gb \to tH^{\pm}$.

In any of the production and decay modes of the charged Higgs, the signature that will appear in the detector is very similar to the $t\bar{t}$ process. Therefore the existence of a charged Higgs will have an impact on the analysis of $t\bar{t}$ events, and an excess of events observed in the $t\bar{t}$ analysis will be an indication of new physics. In addition, in a large region of the parameters space, the main decay mode of the charged Higgs is $H^{\pm} \to \tau\nu$, meaning that if there is a contamination of charged Higgs events in the $t\bar{t}$ analysis, the tau channel will appear as favoured respect to the electron and muon channels. And again the ratio $r_\tau = \frac{t\to\tau\nu b}{t\to l\nu b}$ will deviate from 1, indicating the existence of new physics beyond the Standard Model.

Chapter 2

LHC and the ATLAS Detector

Nine years after the Large Electron-Positron accelerator (LEP) was turned off, the Large Hadron Collider (LHC) is upon to start data taking in few months, built in the same tunnel were LEP has proven the success of the Standard Model with a precision at the per-mille level. Many of the questions that LEP left unanswered, like the existence of the Higgs boson or beyond the Standard Model discoveries, need a much higher energy per collider beam to collect data at the TeV scale, and an enormous luminosity such that physicists can accumulate the needed statistics within the 10 years of data taking of the LHC.

Such high energy could not be achieved accelerating electrons. The energy dissipated per revolution by the accelerated particles due to synchroton radiation in an accelerator ring of radius R is

$$\delta E = \frac{4\pi e^2}{3R}\beta^3\gamma^4 \tag{2.1}$$

where $\beta = \frac{v}{c}$ and $E = \gamma mc^2$. If the particles are relativistic the γ^4 becomes dominant, and due to this factor, the electron collider suffers from a much larger radiation loss. For example, at 50 GeV, an electron has a γ of 98,000 while a proton would have a γ of 54 for the same energy. So the next step in the high energy collider experiments had to be a hadronic collider. The LHC is placed in a 27 km underground ring that consists of more than a thousand super-conducting dipole magnets and the beams collide at four interactions points where different detectors are placed: Alice, ATLAS, CMS and LHCb. The ATLAS detector is one of the four, and is one of the largest particle detection systems ever constructed. It is a collection of specialised sub-detectors aiming to achieve measurements at an ambitious precision. The ATLAS collaboration is a large international project involving about 2500 physicists belonging to 169 universities from 37 countries.

This chapter explains the properties of the accelerator and the detector in detail.

2.1 The Large Hadron Collider Accelerator

The Large Hadron Collider is installed in the 27 km long former LEP tunnel, located in CERN, Geneva, Switzerland. The LHC will accelerate and collide two proton beams at energies of

7 TeV and a peak luminoity of 10^{34}cm^{-2} s^{-1}. Before particles are injected into the LHC ring they are preaccelerated in a series of accelerators. The LINAC (LINear ACcelerator) accelerates the protons up to 50 MeV. The Booster increases this energy up to 1 GeV and finally the PS (Proton Synchrotron) and the SPS (Super Proton Synchrotron) rise the energy up to 26 GeV and 450 GeV respectively before they are injected into the LHC ring. Figure 2.1 shows schematically all the components of the CERN accelerator system.

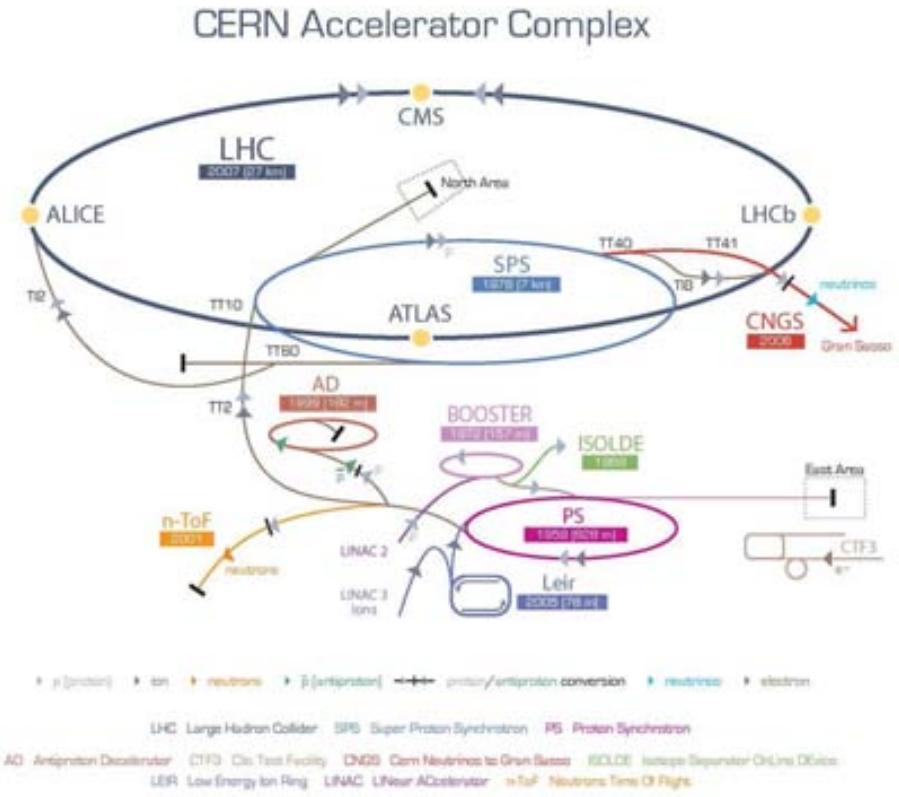

Figure 2.1: Schematic view of the LHC injector system.

The performance requirements of the LHC were never achieved before. The current highest energy accelerator, the Tevatron at Fermilab, collides proton against anti-proton beams at a center of mass energy of 1.9 GeV and has collected up to now ∼3 fb of data over its ten year period of operation. To bend 7 TeV protons aroung the ring, 1,232 LHC superconducting dipoles (Fig 2.2) with a length of 12.2 meters that provide a field strength of 8.6 Tesla are used. The beams are focused using 392 superconducting quadrupole magnets, providing 6.9 Tesla, in the straight sections of the ring. The main properties of the LHC are summarized at Table 2.1.

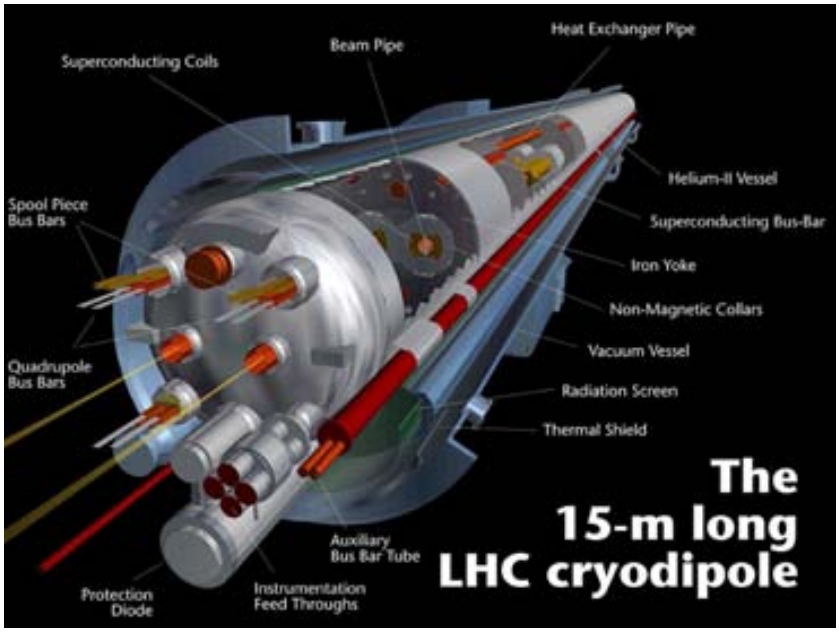

Figure 2.2: Simulation view of the LHC beam pipe within a dipole magnet and its cryostat system.

Table 2.1: LHC performance parameters.

Machine performance	
Energy per beam	7 TeV
Dipole field	8.6 Tesla
Coil aperture	56 mm
Distance between apertures	194 mm
Design Luminosity	10^{34}cm^{-2} s^{-1}
Beam-beam parameter	0.0034
Injection energy	450 GeV
Circulating current/beam	0.54 A
Bunch spacing	25 ns
Particles per bunch	10^{11}
Stored beam energy	334 MJ
Normalized transverse emittance	3.75 μm rad
r.m.s. bunch length	0.075 m
β-values at Interaction Point	0.5 m
Full crossing angle	200 μrad
Beam lifetime	22 h
Luminosity lifetime	10 h
Energy loss per turn	6.7 KeV
Critical photon energy	44.1 eV
Total radiated power per beam	3.6 kW

2.2 The ATLAS Detector

2.2.1 ATLAS Definitions

This section describes the coordinate system and nomenclature used to describe the ATLAS detector and the particles emerging from the $p-p$ collisions. This nomenclature will be used repeatedly throughout this document. The interaction point of the $p-p$ collision defines the origin of the coordinate system, while the beam direction defines the $z-$axis, being the $x-y$ plane the plane transverse to the beam direction. The azimuthal angle ϕ is measured around the beam axis, and the polar angle θ is the angle from the beam axis. The pseudorapidity is defined as $\eta = -\ln[\tan(\theta/2)]$ (in the case of massive objects such as jets, the rapidity $y = 1/2\ln[(E+p_z)/(E-p_z)]$ is used). The transverse momentum p_T, the transverse energy E_T, and the missing transverse energy $\not{E}_T$ are defined in the $x-y$ plane. The distance ΔR in the pseudorapidity-azimuthal angle space is defined as $\Delta R = \sqrt{\Delta\eta^2 + \Delta\phi^2}$.

2.2.2 Physics Programme at ATLAS

The ATLAS detector has been defined to cover much of the new phenomena which one can hope to observe at the TeV scale. The high luminosity and increased cross-sections at the LHC enable further high precision measurements of QCD, electroweak interactions and flavour physics. The top quark will be produced at a rate of few tens of Hz, providing the opportunity to test its couplings and spin.

The ATLAS detector is often referred to as a "discovery machine". The search for the Standard Model Higgs boson has been established as a benchmark in the ATLAS physics programme. It is a particularly important process since, depending on the mass of the Higgs boson, there is a wide range of production and decay mechanisms: from photon pairs or four leptons to more spectacular topologies such as $t\bar{t}H$. To reject the background from various channels, precision measurements in tracking and calorimetry are very important.

Searches for the Higgs boson of the Standard Model, or for particles such as the A and $H^{\pm}$ of the minimal supersymmetric extension of the Standard Model, require sensitivity to processes involving τ-leptons and good b-tagging performance. Should the Higgs boson be discovered, it would need to be studied in several modes, regardless of its mass, in order to fully disentangle its properties and establish its credentials as belonging to the Standard Model or an extension thereof.

These features are also very important for the search of Supersymmetry. The decays of supersymmetric particles, such as squarks and gluinos, would involve cascades which, if R-parity is conserved, always contain a lightest stable supersymmetric particle (LSP). As the LSP would interact very weakly with the detector, the experiment would measure significant missing transverse energy in the final state. Large acceptance in pseudorapidity with almost full azimuthal angle coverage of the detector is a desirable feature for a reliable measurement of missing energy.

Finally, new heavy gauge bosons W' and Z' could be accesible for masses up to approximately 6 TeV. To study their leptonic decays, high-resolution lepton measurements and charge identification are needed in the p_T-range of a few TeV

The formidable LHC luminosity and resulting interaction rate are needed because of the small cross-section expected for many of the processes mentioned above. However, the LHC will produce a total rate of 10^9 inelastic events/s at design luminosity. This presents a serious experimental difficulty as it implies that every candidate event for new physics will on the average be accompanied by 23 inelastic events per bunch-crossing. This requires highly efficient triggering on low transverse-momentum objects with sufficient background rejection, to achieve an acceptable trigger rate for most physics processes of interest.

2.2.3 Detector Overview

The overall ATLAS [48] detector layout is shown in Figure 2.3.

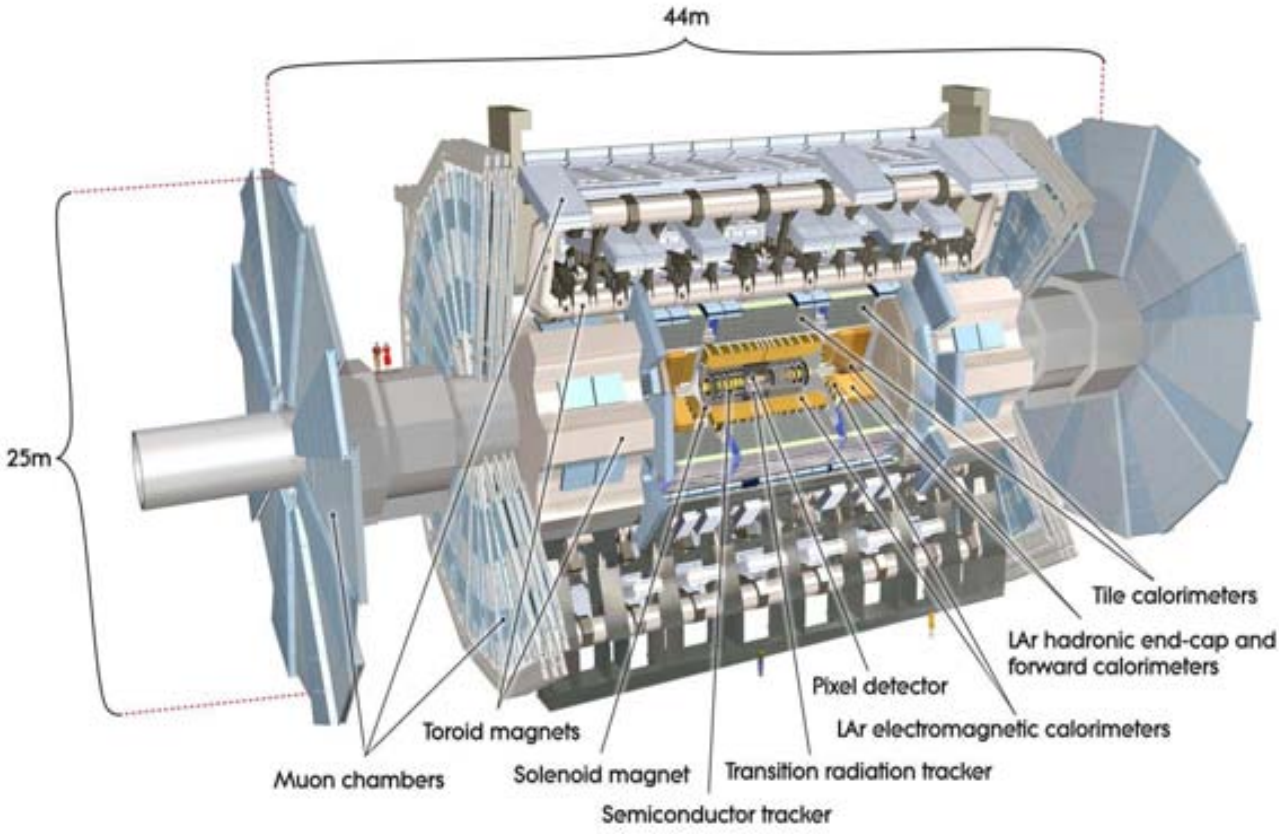

Figure 2.3: Graphical view of the ATLAS detector.

The detector is a complex of sub-detectors weighing approximately 700 tonnes in total and its dimensions are 25 m in height and 44 m in length. The subdetector systems can be divided

into the following:

Table 2.2: Performance requirements of the ATLAS detector for every ATLAS sub-detector.

Detector component	**Required resolution**	**η coverage**	
		Measurement	Trigger
Tracking	$\sigma_{P_T}/P_T = 0.05\% P_T \oplus 1\%$	± 2.5	
EM calorimetry	$\sigma_E/E = 10\%/\sqrt{E} \oplus 0.7\%$	± 3.2	± 2.5
Hadronic calorimetry (jets)			
barrel and end-cap	$\sigma_E/E = 50\%/\sqrt{E} \oplus 3\%$	± 3.2	± 3.2
forward	$\sigma_E/E = 100\%/\sqrt{E} \oplus 10\%$	$3.1 < \lvert\eta\rvert < 4.9$	$3.1 < \lvert\eta\rvert < 4.9$
Muon spectrometer	$\sigma_{P_T}/P_T = 10\%$ at $P_T = 1$ TeV	± 2.7	± 2.4

- Tracking detector for pattern recognition, momentum and vertex measurements.
- Calorimetry for energy measurement of electromagnetic and hadronic showers, with excellent performance in terms of energy and position resolution.
- Magnet System for bending the trajectory of charged particles. The inner detector is immersed in a 2 T solenoidal field, while the muon detectors are surrounded by an air-core toroid system which produces a toroidal magnetic field of approximately 0.5 T and 1 T in the central and end-cap regions, respectively.

The performance requirements needed for each subdetector in order to fulfill the expectations of the physics programme are summarized in Table 2.2.

The proton-proton interaction rate at the design luminosity of 10^{34} cm^{-2} s^{-1} is approximately 1 GHz, while the event data recording, based on technology and resource limitations, is limited to about 200 Hz. This requires an overall rejection factor of $5 \cdot 10^6$ against minimum-bias events while maintaining the efficiency for the interesting physics processes. The Level-1 (L1) trigger, hardware based, makes an initial selection based on high-p_T muons as well as reduced-granularity calorimeter signatures. The Level-1 has the task to reduce the data rate to approximately 75 KHz. The subsequent two levels, known as the high-level trigger, are the Level-2 (L2) trigger and the Event Filter (EF) and they are based on software algorithms to be run in a PC farm. They must reduce the event rate to the final 200 Hz for storage. The high-level trigger has access to the full detector data with full granularity.

Tracking

The inner tracking detectors constitute the innermost system of the ATLAS detector. The innermost layer of the tracking detector is placed only a few centimeters from the interaction point. A layout of the tracking detectors of ATLAS is illustrated in Figure 2.4 and its basic parameters summarised in Table 2.3.

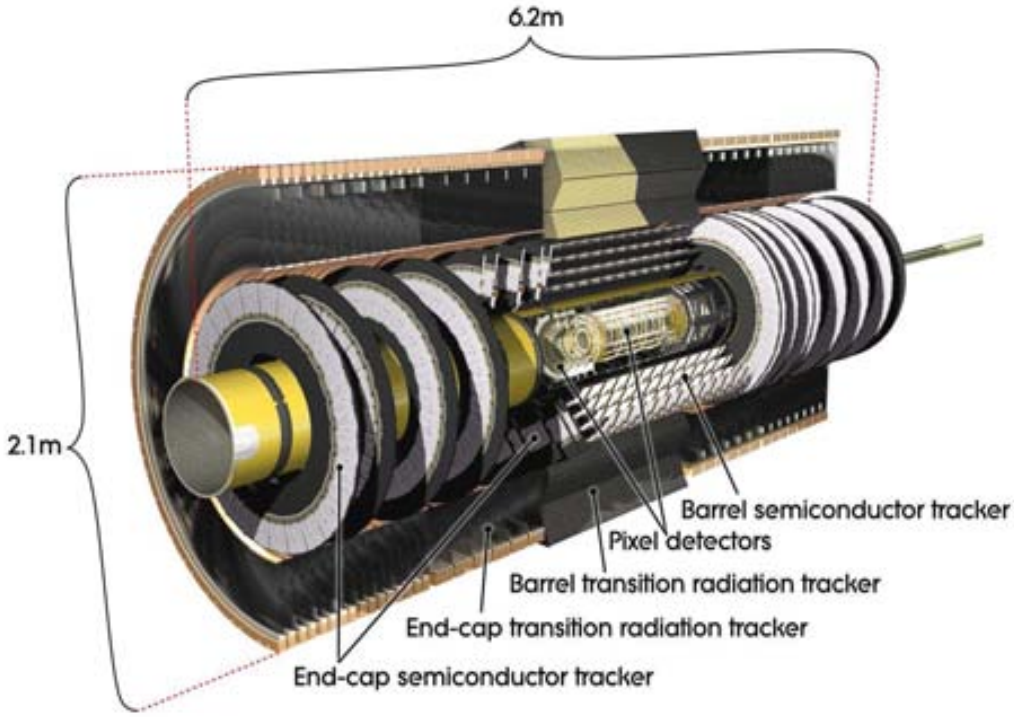

Figure 2.4: Cut-away view of the ATLAS inner detector.

Table 2.3: Main parameters of the ATLAS inner detector.

Item		**Radial extension (mm)**	**Length (mm)**
Overall ID envelope		$0 < R < 1150$	$0 < \|z\| < 3512$
Beam-pipe		$29 < R < 36$	
Pixel	Overall envelope	$45.5 < R < 242$	$0 < \|z\| < 3092$
3 cylindrical layers	Sensitive barrel	$50.5 < R < 122.5$	$495 < \|z\| < 650$
2x3 disks	Sensitive end-cap	$88.8 < R < 149.6$	$495 < \|z\| < 650$
SCT	Overall envelope	$255 < R < 549$ (barrel)	$0 < \|z\| < 805$
		$251 < R < 610$ (end-cap)	$810 < \|z\| < 2797$
4 cylindrical layers	Sensitive barrel	$299 < R < 514$	$0 < \|z\| < 749$
2 x 9 disks	Sensitive end-cap	$275 < R < 560$	$839 < \|z\| < 2735$
TRT	Overall envelope	$554 < R < 1082$ (barrel)	$0 < \|z\| < 780$
		$617 < R < 1106$ (end-cap)	$827 < \|z\| < 2744$
73 straw planes	Sensitive barrel	$563 < R < 1066$	$0 < \|z\| < 712$
160 straw planes	Sensitive end-cap	$644 < R < 1004$	$848 < \|z\| < 2710$

The ATLAS inner detector is designed to provide hermetic and robust pattern recognition,

excellent momentum resolution and both primary and secondary vertex measurements (needed for heavy flavour quark identification) for charged tracks with p_T above 0.5 GeV and within the pseudorapidity range $|\eta| < 2.5$. It also provides electron identification over $|\eta| < 2.0$ between 0.5 GeV and 150 GeV. The ATLAS tracking detectors are composed by three different types of tracking modules (from innermost layer to outermost): pixel detectors, semiconductor tracker (SCT) and straw tubes of the Transition Radiation Tracker (TRT).

The precision tracking detectors (pixel and SCT) cover the region $|\eta| < 2.5$. In the barrel region they are arranged on concentric cylinders around the beam axis while in the end-cap regions they are located on disks perpendicular to the beam axis.

The inner detector is immersed in a 2 T magnetic field generated by a central solenoid needed to bend the trayectory of every charged particle, in order to measure its momentum.

Figure 2.5 shows the different tracking detector elements that form part of the ATLAS inner detector, while the following sections describe them in more detail.

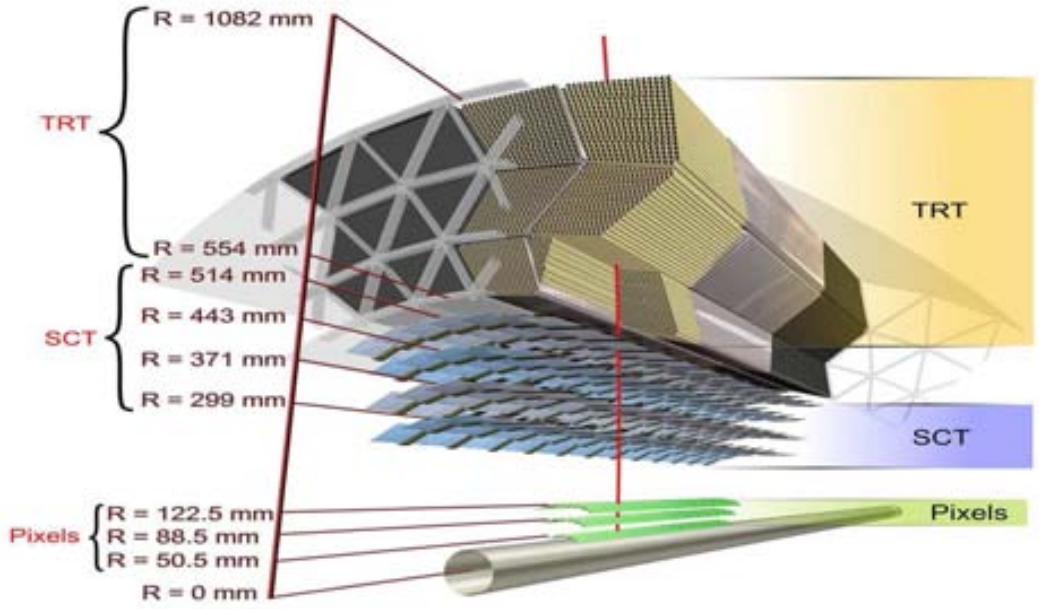

Figure 2.5: Structural elements of the different tracking detectors that form part of the ATLAS inner detector in the central barrel. The red line simulates a charged track with p_T of 10 GeV that traverses successively the beam-pipe, three cylindrical silicon-pixel layers, four cylindrical barrel silicon-microstrip sensors (SCT) and approximately 36 axial straws of the barrel transition-radiation tracker modules.

Pixel Detector

The pixel detector provides, around the vertex region, the highest granulariy. It is a semiconductor detector made of wafers with very small rectangular two-dimensional sensors, with a typical size of the order of microns. They are arranged in layers, which are segmented in $R-\phi$ and z with typically three pixel layers crossed per track.

Three layers of modules occupy the radius from 5 cm to 13 cm from the beam pipe. All pixel sensors are identical and have a minimum pixel size of $50 \times 400\mu\text{m}^2$. The pixel detector has approximately 80.4 million readout channels for these sensors.

The spatial accuracies are 10μm in $R\phi$ and 115μm in z.

Semiconductor Tracker

The SCT tracker surrounds the pixel layers with its four barrel layers and nine end-cap disks covering the radius from 25.5 cm to 56 cm. These layers determine the trajectory and the charge of the tracks. In the barrel region, two silicon modules are glued together back to back with a 40 mrad stereo angle with respect to each other, and are positioned parallel to the beam direction, measuring $R-\phi$. They consist of two 6.4 cm long daisy-chained sensors with a strip pitch of 80μm. In the end-cap region, the detectors have a set of strips running radially and a set of stereo strips at an angle of 40 mrad. The mean pitch of the strips is again about 80μm. The intrinsic accuracies per module are $17\mu\text{m}(R-\phi)$ and $580\mu\text{m}(z)$ for both, the barrel and the disks. The total number of readout channels in the SCT is approximately 6.3 million.

Transition Radiation Tracker

This sub-detector is based on the measurement of the transition radiation produced when a relativistic particle traverses an inhomogeneous medium. The intensity of the transition radiation is roughly proportional to the particle energy and the probability of transition radiation at each interface between different materials increases with the relativistic gamma factor. Therefore, for a given energy, this allows a discrimination between a lighter particle (which will have an associated γ factor high) and a heavier particle (with a lower γ factor).

The straw hits of the TRT also contribute to the momentum measurement, and in combination with the small radii space points measurements of the Pixels and SCT, provide a robust patter recognition and high precision in both $R-\phi$ and z coordinates. The lower precision of the TRT hits compared to the silicon is compensated by the large number of measurements and longer measured track length.

The Transition Radiation Tracker detector consists of a large number of straws which can operate at very high rates. These straws detect the transition-radiation photons caused by charged particles passing by the gas contained in the straw. A large number of hits (typically 36 per track) is provided by the 4 mm diameter straw tubes of the TRT, which cover tracks in pseudorapidity up to $|\eta| = 2.0$. The TRT provides information only in $R-\phi$ with an intrinsic accuracy of 130μm per straw. In the barrel region, the straws are parallel to the beam axis and

are 144 cm long. In the end-cap ragion, the straws are arranged radially in wheels and they are 37 cm long. The TRT contains a total number of 351000 readout channels.

Solenoid Magnet System

The ATLAS central solenoid [49] is designed to provide a 2 Tesla axial field (following the direction of the beam pipe) and it is placed around the inner detectors.

The magnetic field deflects charged particles coming from the interaction point in such a way that it does not modify their transverse direction, bending the trajectories in the $R - \phi$ plane with a radius proportional to its momentum $r = \frac{p}{qB}$.

Figure 2.3 shows a general layout with the central solenoid positioned in front of the electromagnetic calorimeter. To achieve the desired calorimeter performance, the layout was carefully optimised to keep the material thickness in front of the calorimeter as low as possible resulting in a material contribution of ~ 0.66 radiation lengths for the solenoid at normal incidence.

The inner and outer diameters of the solenoid are 2.46 m and 2.56 m and its axial length is 5.8 m. The coil is wound with a high-strength Al-stabilised NbTi conductor, specially developed to achieve a high field while optimising thickness. The flux is returned by the steel of the ATLAS hadronic calorimeter and its girder structure.

Calorimetry

The layout of the ATLAS calorimeter system is presented in Figure 2.6 and its properties and parameters summarised in Table 2.4.

The ATLAS calorimeter system is composed of three main parts: electromagnetic calorimeter (EM), hadronic calorimeter and forward calorimeter (FCAL). The electromagnetic calorimeter and hadronic calorimeter are divided in two parts, barrel and end-cap. The EM barrel extends up to $|\eta| < 1.4$ and the end-cap is located at $1.375 < |\eta| < 3.2$. The hadronic barrel extends up to $|\eta| < 1.7$ (including the extended barrel) and the end-cap is at $1.5 < |\eta| < 3.2$. Finally, forward calorimeter is placed beyond the coverage of the EM and hadronic end-caps, at $3.2 < |\eta| < 4.9$.

Therefore, the ATLAS calorimeters cover the range $|\eta| < 4.9$. In the range $|\eta| < 2.5$, coverage of the inner detector, the EM calorimeter has a finer granularity in order to achieve precision measurements for electrons and photons. Above this range in η, the coarser granularity of the calorimeter is enough to satisfy the requirements of jets and $\not{E}_T$ measurements.

Calorimeters must provide a good containment of electromagnetic and hadronic showers as well as limit punch-through into the muon system. To satisfy these requirements, the thickness of the EM calorimeter is > 22 radiation lengths (X_o) in the barrel and $> 24X_o$ in the end-caps. The total thickness of the calorimeter at $\eta = 0$, 11 interaction lengths (λ), is enough to reduce punch-through below the irreducible level of prompt or decay muons.

The amount of material provided by the different components of the calorimeter is plotted in Figure 2.7.

Table 2.4: Main parameters of the ATLAS calorimeter detectors.

EM calorimeter				
	Barrel		End-cap	
	Granularity $\Delta\eta \times \Delta\phi$	$\|\eta\|$ coverage	Granularity $\Delta\eta \times \Delta\phi$	$\|\eta\|$ coverage
Presampler	0.025×0.1	$\|\eta\| < 1.52$	0.025×0.1	$1.5 < \|\eta\| < 1.8$
Calorimeter 1st layer	$0.025/8 \times 0.1$ 0.025×0.025	$\|\eta\| < 1.40$ $1.40 < \|\eta\| < 1.475$	0.050×0.1 0.025×0.1 $0.025/8 \times 0.1$ $0.025/6 \times 0.1$ $0.025/4 \times 0.1$ 0.025×0.1 0.1×0.1	$1.375 < \|\eta\| < 1.425$ $1.425 < \|\eta\| < 1.5$ $1.5 < \|\eta\| < 1.8$ $1.8 < \|\eta\| < 2.0$ $2.0 < \|\eta\| < 2.4$ $2.4 < \|\eta\| < 2.5$ $2.5 < \|\eta\| < 3.0$
Calorimeter 2nd layer	0.025×0.025 0.075×0.025	$\|\eta\| < 1.40$ $1.40 < \|\eta\| < 1.475$	0.050×0.025 0.025×0.025 0.1×0.1	$1.375 < \|\eta\| < 1.425$ $1.425 < \|\eta\| < 2.5$ $2.5 < \|\eta\| < 3.2$
Calorimeter 3rd layer	0.050×0.025	$\|\eta\| < 1.35$	0.050×0.025	$1.5 < \|\eta\| < 2.5$
LAr hadronic end-cap				
Granularity $\Delta\eta \times \Delta\phi$			0.1×0.1 0.2×0.2	$1.5 < \|\eta\| < 2.5$ $2.5 < \|\eta\| 3.2$
LAr forward calorimeter				
FCal1			Granularity $\Delta x \times \Delta y (cm)$ 3.0×2.6 $\sim$ four times finer	$\|\eta\|$ coverage $3.15 < \|\eta\| < 4.30$ $3.10 < \|\eta\| < 3.15,$ $4.30 < \|\eta\| < 4.83$
FCal2 FCal3			3.3×4.2 $\sim$ four times finer 5.4×4.7 $\sim$ four times finer	$3.24 < \|\eta\| < 4.50$ $3.20 < \|\eta\| < 3.24,$ $4.50 < \|\eta\| < 4.81$ $3.32 < \|\eta\| < 4.60$ $3.29 < \|\eta\| < 3.32,$ $4.60 < \|\eta\| < 4.75$
Scintilator tile calorimeter				
	Barrel		**Extended Barrel**	
	Granularity $\Delta\eta \times \Delta\phi$	$\|\eta\|$ coverage	Granularity $\Delta\eta \times \Delta\phi$	$\|\eta\|$ coverage
layer 1 & 2	0.1×0.1	$\|\eta\| < 1.0$	0.1×0.1	$0.8 < \|\eta\| < 1.7$
layer 3	0.2×0.1	$\|\eta\| < 1.0$	0.2×0.1	$0.8 < \|\eta\| < 1.7$

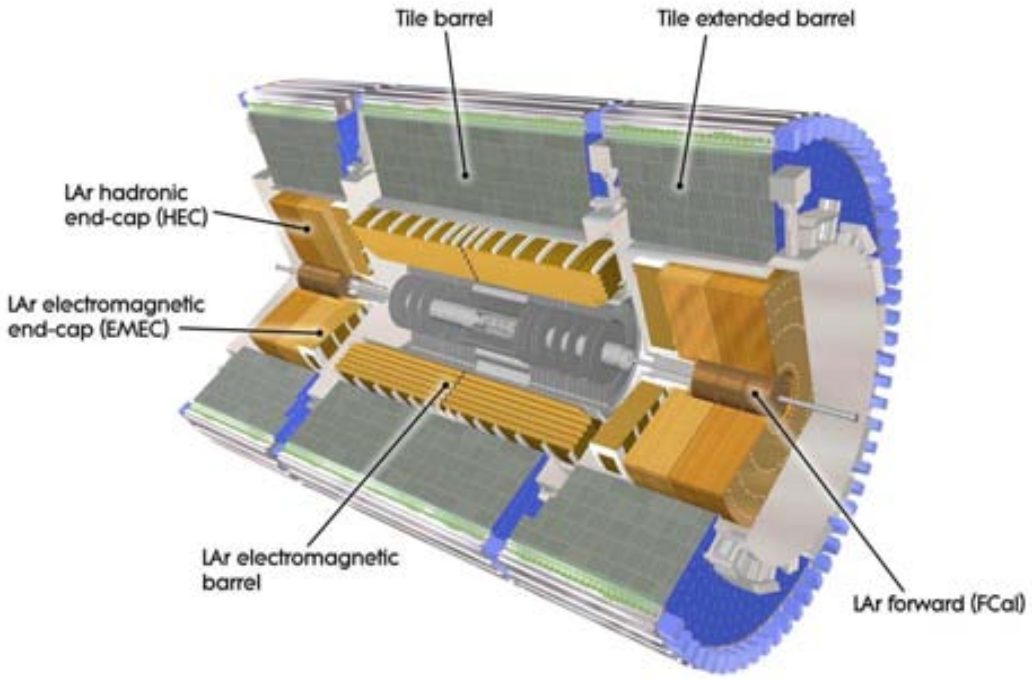

Figure 2.6: Cut-away view of the ATLAS calorimeter system.

Electromagnetic Calorimeter

The electromagnetic calorimeter is a lead-LAr detector with accordion-shaped kapton electrodes and lead absorber plates. The accordion geometry provides naturally a full coverage in ϕ without any cracks, and a fast extraction of the signal at the rear or at the front of the electrodes. When photons or electrons traverse the lead, they generate an electromagnetic shower in their interaction with the material. The number of secondary electrons/positrons generated in the shower is proportional to the energy of the incident particle, and their presence is detected by the kapton electrodes.

The lead plates are separated by a gap of about 4 mm that is immersed in a bath of liquid argon and subjected to a large electric field. When a charged particle from the electromagnetic shower interacts with the liquid argon it generates electron-ion pairs along its path, which are later drifted by the electric field, causing at the same time more ionisation electrons. All ionisation electrons are finally collected by the electrodes, being the intensity of the current generated proportional to the energy of the charged particles that entered into the liquid argon.

The EM calorimeter is divided into a barrel part ($|\eta| < 1.475$) and two end-cap components ($1.375 < |\eta| < 3.2$). Each end-cap component is divided into two coaxial wheels: an outer wheel covering the region $1.375 < |\eta| < 2.5$ and an inner wheel covering the region $2.5 < |\eta| < 3.2$. Over the central region of the EM calorimeter, devoted to precision measurements for electrons and photons, the EM calorimeter is divided in three different layers in depth with different angular

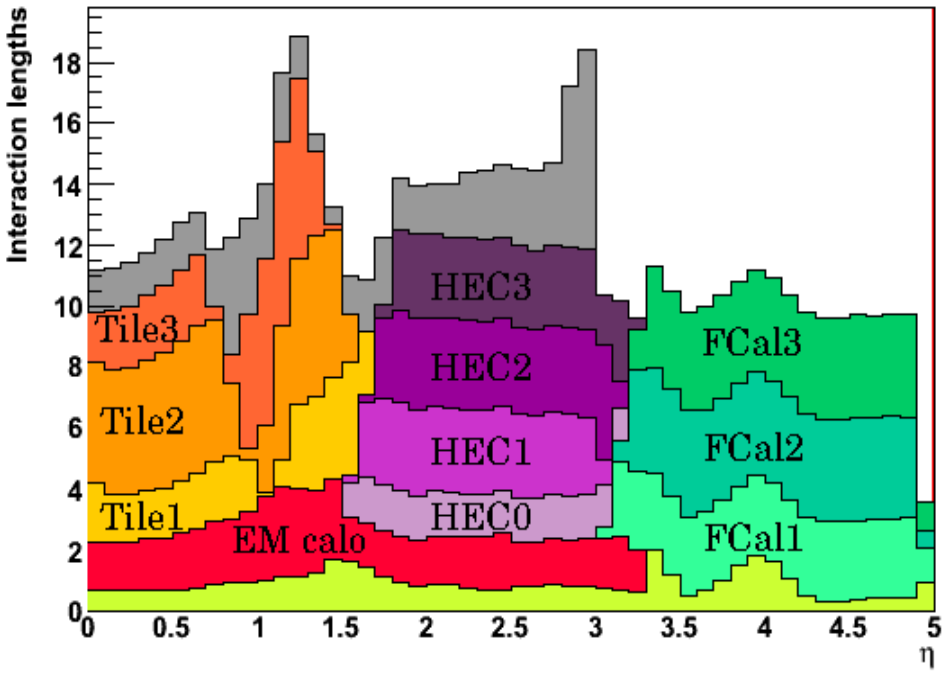

Figure 2.7: Amount of material, in units of interaction lengths, as a function of $|\eta|$ in front of the electromagnetic calorimeters, in the electromagnetic calorimeters, and in each hadronic layer, as well as the amount of material at each forward calorimeter layer. The last layer (up to $|\eta| < 3.0$) corresponds to the amount of material in front of the first layer of the muon spectrometer.

resolutions. Table 2.4 summarises the properties of every layer of the EM calorimeter. The first layer is finely segmented along η. The second layer collects the largest fraction of the energy of the electromagnetic shower and the third layer collects only the tail of the electromagnetic shower and, therefore, it is less segmented in η. In the region of $|\eta| < 1.8$ a presampler detector is used to correct for the energy lost by electrons and photons upstream of the calorimeter. It consists of an active liquid argon layer of thickness 1.1 cm (0.5 cm) in the barrel region of $|\eta| < 1.52$ (end-cap region of $1.5 < |\eta| < 1.8$).

Hadronic Calorimeters

The hadronic calorimeters are placed behind the EM calorimeter. They absorb and measure the energies of hadrons (protons, neutrons, pions, kaons, etc). Two different techniques are used to build the hadronic calorimeters, depending on the η coverage. The barrel region uses a tile scintillator technique while in the end-cap, the LAr (like in the EM calorimeters) is the solution adopted.

Tile Calorimeter

The tile calorimeter is placed directly outside the EM calorimeter envelope, with the barrel region covering the range $|\eta| < 1.0$, and its two extended barrels the range $0.8 < |\eta| < 1.7$. It consists of steel absorbers separated by tiles of scintillating plastic. An interaction of a high-energy hadron in one of the steel plates will produce a hadronic shower of many low-energy protons, neutrons and other hadrons. When the hadronic shower traverses the tiles of scintillating plastic, they yield light, in an amount proportional to the incident energy, that can be collected and its intensity measured.

The barrel and extended barrels are divided azimuthally into 64 modules. Radially, the tile calorimeter covers from an inner radius of 2.28 m to an outher radius of 4.25 m and it is segmented in three different layers in depth, of approximately 1.5, 4.1 and 1.8λ for the barrel, and 1.5, 2.6 and 3.3 λ for the extended barrel. Two sides of the scintillating tiles are read out by wavelength shifting fibres into two separate photomultiplier tubes.

LAr Hadronic End-cap Calorimeter

The total radiation emanating from the collision point increases its intensity at small angles with respect to the beam. As scintillating tiles are damaged by excessive exposure to radiation, the hadronic calorimetry at angles to the beam between 5 and 25 degrees could not be provided by the scintillating tiles technique. A liquid argon device very similar to the electromagnetic calorimeter is chosen instead. The main difference with respect to the electromagnetic calorimeter is that the lead plates are replaced by copper plates, more appropiate for the hadronic showers and the argon gaps are of 8 mm (instead of 4 mm).

It is composed by two independent wheels per end-cap, located directly behind the end-cap electromagnetic calorimeter. Each wheel is built from 32 wedge-shaped modules. The wheels closest to the interaction point are built with 25 mm copper plates while those further away use 50 mm copper plates.

LAr Forward Calorimeter

In order to detect jets at very small angles (with respect to the beam), the forward calorimeter (FCal) covers angles as small as 1 degree relative to the beam. Due to the extremely hostile radiation environment in the angular region between one and five degrees, the LAr (robust against radiation) was the chosen technique for the forward calorimeter. The FCal is approximately 10 interaction lengths deep and is composed by three modules in each end-cap. The first module is made of copper, optimised for electromagnetic measurements, while the other two, made of tungsten, measure predominantly the energy of hadronic interactions. Each module consists of a metal matrix, with regularly spaced longitudinal channels filled with the electrode structure: concentric rods of 4.5 mm diameter centered in tubes of 5 mm of inner diameter. The LAr fills the small gaps between the rod and the tube wall. A few hundred volts between rod and tube produce the electric field to make electrons drift in the argon-filled gap.

Toroid Magnet System

The ATLAS toroid magnet system is placed outside the hadronic calorimeter and generates (in the barrel region) a toroidal field centred in the beam pipe. A layout of the eight toroids and the end-caps outside the hadronic calorimeter is presented in Figure 2.8.

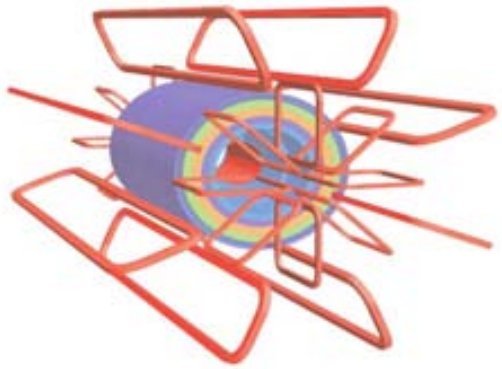

Figure 2.8: View of the ATLAS toroidal magnet system, the tile calorimeter steel and the solenoid winding inside the calorimeter volume. In red are the eight barrel toroid (BT) coils and the end-cap coils interleaved.

The aim of the toroid magnet system is to bend muons scaping from the calorimeters in order to be able to measure their momentum through the muon detectors (Section 2.2.3). The deflection of the charged particles traversing the toroidal field is perpendicular to the direction of the deflection provided by the solenoid magnet in the inner detector.

In the barrel (BT), the eight super-conducting coils are assembled radially around the beam axis, providing approximately a magnetic field of 0.5 T to the muon detectors in the central region. The overall size of the barrel toroid system is 25.3 m in length with an inner diameter of 9.4 m and outer diameter of 20.1 m. The end-cap toroids (ECT) are installed on both sides

of the barrel toroid and produce a magnetic field of approximately 1 T to the muon detectors in the end-cap region.

The conductor and coild-winding technology is essentially the same in the barrel and the end-cap toroids. It is based on winding a pure Al-stabilised Nb/Ti/Cu conductor into the coils. Both, the BT and the ECT are enclosed in aluminium casings and coils are individually placed in the cooling modules which use liquid helium at temperature of 4.5 K. Approximately, the range $|\eta| < 1.0$ is covered by the BT while the field from ECT is dominant in $1.4 < |\eta| < 2.7$.

Muon Spectrometer

The layout of the ATLAS muon spectrometer is shown in Figure 2.9 and its main parameters summarised in Table 2.5.

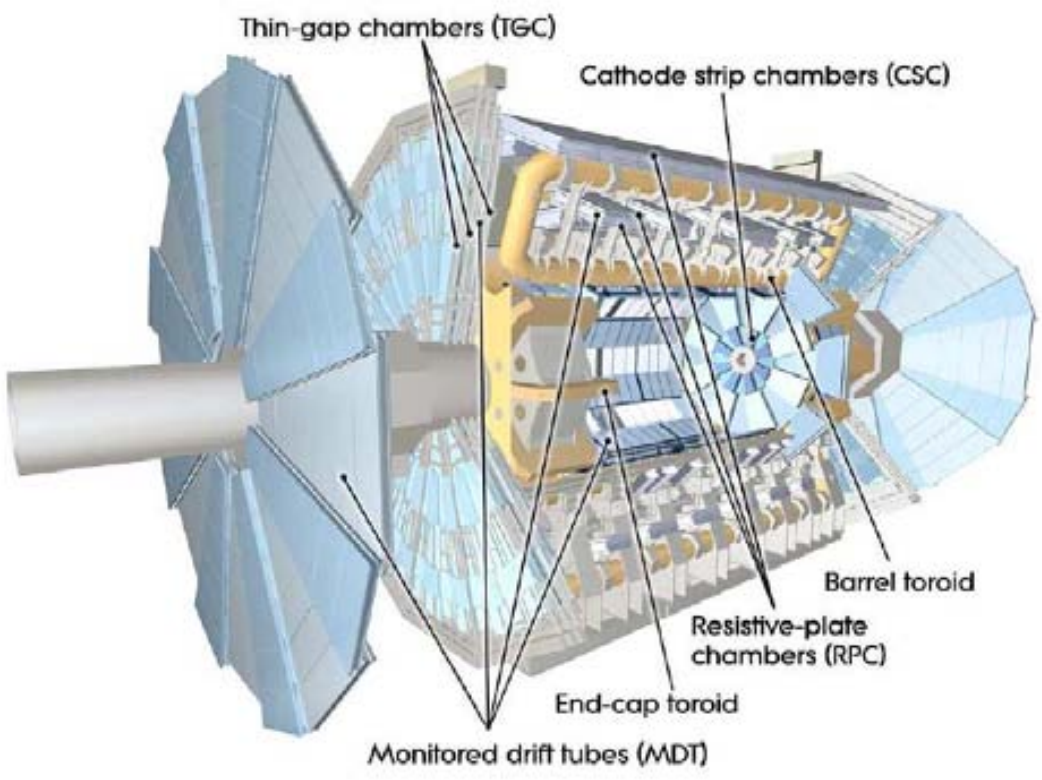

Figure 2.9: View of the ATLAS muon system.

Table 2.5: Main parameters of the ATLAS muon spectrometer.

Monitored drift tubes	**MDT**
Coverage	$\|\eta\| < 2.7$ (innermost layer: $\|\eta\| < 2.0$)
Number of chambers	1150
Number of channels	354000
Function	precision tracking
Cathode strip chambers	**CSC**
Coverage	$2.0 < \|\eta\| < 2.7$
Number of chambers	32
Number of channels	31000
Function	precision tracking
Resistive plate chambers	**RPC**
Coverage	$\|\eta\| < 1.05$
Number of chambers	606
Number of channels	373000
Function	triggering
Thin gap chambers	**TGC**
Coverage	$1.05 < \|\eta\| < 2.7$
Number of chambers	3588
Number of channels	318000
Function	triggering

The muon system measures the charge and energy of the muons that scape from the hadronic calorimeter, based on the deflection of the muon tracks traversing the large air-core toroid magnetic field. Given the high background rates at the LHC, the muon drift chambers will have to operate at high levels of occupancy. For this reason the muon system is instrumented separately with chambers for precision measurement and chambers for trigger. The magnetic field provided by the ATLAS toroid magnet system (see Section 2.2.3) is mostly orthogonal to the muon trajectory while the toroid magnet was designed trying to minimise the multiple scattering effects on muon crossing the magnet instruments.

Over the range $|\eta| < 1.4$, the magnetic bending is provided by the barrel toroid. The range $1.4 < |\eta| < 1.6$ is referred to as the transition region where the magnetic field is provided by a combination of barrel and end-cap fields. In the range $1.6 < |\eta| < 2.7$ the muon tracks are bent by the two end-cap toroids.

In the barrel region, tracks are measured in chambers arranged in three cylindrical layers around the beam axis containing chambers for tracking precision, Monitor Drift Tubes (MDT) and chambers for trigger purposes, Resistive plate chambers (RPC). In the transition and end-cap regions, the chambers are installed in three planes perpendicular to the beam, containing monitored drift tubes (MDT) chambers and Cathode Strip Chambers (CSC) for precision tracking as well as Thin-gap Chambers (TGC) for trigger purposes.

Monitored Drift Tubes are aluminium-walled of 3 cm diameter gaseous drift chambers, with a central wire of 50 μm diameter. The length of the wire varies from ∼1 m up to ∼6 m depending of the position of the chamber within the ATLAS detector. The tube is filled with gas $Ar - CO_2$ in the proportion of 93%-7% respectively. Although this gas has non-uniform drift velocity, it is safe in large quantities.

A muon traversing the chamber ionises the gas under a high electric field. Ionisation electrons are then drifted to the sense wire inducing an electric charge that can be measured. A typical track produces about 400 primary ion pairs. The maximum drift time of ionised electrons is 800 ns and the typical drift velocity is $\sim 2\text{cm}/\mu\text{s}$. With the timing measurements, the positional resolution that can be achieved is ∼0.1 mm.

Resistive Plate Chambers are optimised to provide a good time resolution for triggering, meaning to assign more than 99% of the triggered muons to the correct bunch-crossing. In each module of RPC, a narrow gap between plates is filled with gas. The RPC measures ionisation pulses in gas at high voltage although it contains no wires and therefore the spatial resolution is much coarser, while the time response is higher compared to the MDT. The typical space-time resolution of the RPC is of the order of 1 cm×1 ns.

Although MDT can cover the requirements for precision measurements of muons in most of the coverage of the ATLAS detector, their rather large diameter and high operating pressure make them unsuitable for use in areas where high (> 200 Hz/cm^2) counting rates are expected. In ATLAS such high background rates are produced in the first muon measuring station at $2.0 < |\eta| < 2.7$. In this region, Cathode Strip Chambers (CSC) multi-wire proportional chambers are used instead. They consist of an array of anode wires in narrow gas enclosures with metal walls arranged in the form of strips. Applying a high voltage between wires and wall strips, traversing muons produce signals on the strips that allow position resolution better than 60μm with a time resolution of the order of 7 ns.

For trigger muon measurements in the end-cap, Thin Gap Chambers (TGC) are used instead of the RPC used in the barrel. TGC operate in a saturated mode and therefore, have a structure similar to multiwire proportional chambers. The high electric field around TGC wires and the small distance between wires strongly reduces the drift component of ionisation clusters, leading to very good time resolution. TGC design can achieve a 99% efficiency for a minimum-ionizing particle within a time window of 25 ns (the LHC bunch-crossing period).

Over most of the η range, the precision measurement of the muon track is provided by the MDT's, while for large pseudorapidities, $2 < |\eta| < 2.7$, the CSC chambers are used instead in the innermost plane.

The trigger system covers the range $|\eta| < 2.4$. In the barrel region, the trigger chambers are RPC while in the end-cap regions the TGC are the chosen solution.

Chapter 3

ATLAS Simulation and Reconstruction

The first step in the Monte Carlo simulation of the pp collisions is the generation of the various processes produced in the collision. The ATLAS event generation framework implements interfaces to a wide variety of event generators and Parton Shower (PS) simulators. The generator is responsible for any prompt decays (e.g. Z or W bosons) and stores any stable particle expected to propagate through a part of the detector. Because it only considers immediate decays, there is no need to consider detector geometry during the generation. The generation of the relevant processes studied in this analysis is described in Section 3.1.

The generated events are then fed into the simulation that describes the detector response to every particle generated that crosses the detector. Section 3.2 describes briefly the ATLAS simulation software. Finally, the last step is the reconstruction software that reconstructs the full event from raw data (or simulated Monte Carlo data), starting from basic objects in each subdetector, like a cluster in the calorimeter, up to final identified particles, obtained combining the information of several subsystems, like the electron reconstruction from clusters in the calorimeters and tracks in the inner detector.

Section 3.3 presents the details of the reconstruction software for each piece relevant to this analysis.

3.1 Signal and Background Generation

3.1.1 Production Summary

Table 3.1 summarises the theoretical cross sections for signal and background processes as well as the MC generators used to produce the event samples. The theoretical values of the cross sections are extracted from the referenced papers. Some samples include a filter at the generator level, like the $t\bar{t}$ semileptonic/dilepton sample that was forced to have (at least) one W boson decaying leptonically, with a lepton filter in charge of removing events with leptons out of acceptance. These filters are used to increase the efficiency of the production, considering that

those events that do not pass the filter at the generator level, will not do it in the event selection (after reconstruction). The cross section of each process after applying the corresponding filter is quoted as *sample* σ. The QCD di-jets process was split in several MC samples, covering different ranges of p_T of the jets produced in the event (more specifically, the p_T range specified in the QCD dijet processes of Table 3.1 corresponds to the CKIN[1)] parameter of the PYTHIA [50] generator) The rightmost column shows the integrated luminosity that was generated for the corresponding sample.

Table 3.1: List of MC generators used for every process considered in the analysis together with the theoretical cross section and the cross section of the generated Monte Carlo sample.

Process	Generator	Simulation	Theoretical σ(pb)	Sample σ(pb)	$\int \mathscr{L}$dt(pb^{-1})
$t\bar{t}$ semileptonic/dilepton	MC@NLO [51]	GEANT4	$833^{+52}_{-39} \times 0.54$ [52]	450	1300
$t\bar{t}$ fully hadronic	MC@NLO	GEANT4	$833^{+52}_{-39} \times 0.46$	385.2	130
t-channel single top	AcerMC [53]	GEANT4	$246^{9.3}_{-10.2}$ [54]	79.7	310
s-channel single top	AcerMC	GEANT4	10.65 ± 0.56 [54]	3.45	14000
Wt associated	AcerMC	GEANT4	64.20 ± 0.06 [55]	29.1	830
W + light jets	ALPGEN [56]	GEANT4	16100^{365}_{-171} [57]	241.5	125.3
W + $b\bar{b}$	ALPGEN	GEANT4	$15.5^{+2.4}_{-2.1}$ [57]	19.92	998.4
QCD dijet [70 GeV − 140 GeV]	PYTHIA [50]	GEANT4	$5.88 \cdot 10^6$	$5.88 \cdot 10^6$	0.05
QCD dijet [140 GeV − 280 GeV]	PYTHIA	GEANT4	$3.08 \cdot 10^5$	$3.08 \cdot 10^5$	1.2
QCD dijet [280 GeV − 560 GeV]	PYTHIA	GEANT4	$1.25 \cdot 10^4$	$1.25 \cdot 10^4$	25
QCD dijet [560 GeV − 1120 GeV]	PYTHIA	GEANT4	360	360	1050
QCD dijet [70 GeV − 140 GeV]	PYTHIA	ATLFAST	$5.88 \cdot 10^6$	$2.5 \cdot 10^3$	230
QCD dijet [140 GeV − 280 GeV]	PYTHIA	ATLFAST	$3.08 \cdot 10^5$	$9.3 \cdot 10^2$	340

3.1.2 $t\bar{t}$ Semileptonic

$t\bar{t}$ events were generated at Next-to-Leading-Order using the MC@NLO [51] generator interfaced with HERWIG 6.5 [58] (to reproduce hadronisation) and JIMMY v4 [59] (to include underlying event modelling). Figure 3.1 shows a Feynman diagram of the production process through gluon-gluon scattering (dominant process -Section 1.1.5-). A filter at the generation level allows to pass only those events with at least one W boson decaying leptonically.

3.1.3 $t\bar{t}$ Fully Hadronic Background

Figure 3.2 shows the Feynman diagram for this process with its decay chain. The generation is equivalent to the $t\bar{t}$ semileptonic signal, with a modification in the filter that allows to pass only

[1)] CKIN is a PYTHIA parameter that determines the p_T of the hard scattering.

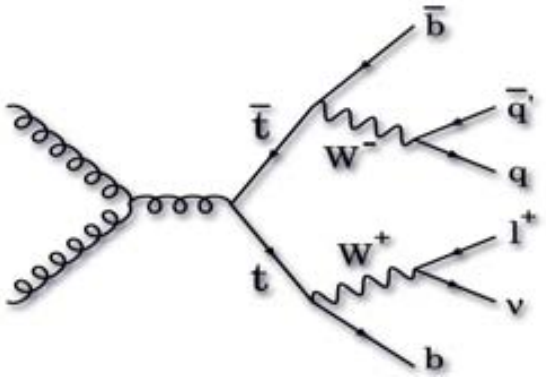

Figure 3.1: Feynman diagram for $t\bar{t}$ semileptonic.

events with both W bosons decaying hadronically.

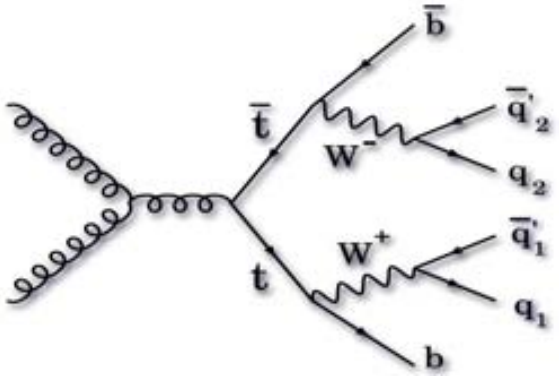

Figure 3.2: Feynman diagram for $t\bar{t}$ fully hadronic.

3.1.4 Single Top Background

There are three different samples of single top events, one for each of the processes represented in Figure 1.5: the s-channel, the t-channel and the associated Wt production. All of them were generated using the AcerMC [53] generator (version 3.1), interfaced with `PYTHIA`. All of them have a somewhat similar topology to the semileptonic $t\bar{t}$ events, and can easily survive the event selection, although the corresponding cross sections are very differeny among the different channels. All single top events were generated with leptonic decay modes only.

- s-channel:

  This is the production process of the single top with the lowest cross section, that is almost three orders of magnitude lower than the $t\bar{t}$ signal. The Feynman diagram for this channel is shown in Figure 1.5(a).

- t-channel:

The leading order and next-to-leading-order diagrams for the t-channel are represented in Figure 1.5(b). Since the gluon population in the proton is by far the largest at the LHC energy scale, the contribution of the next-to-leading-order diagram to the total cross section is of the same order of magnitude as the leading order diagram.

- Wt:

  This process, represented in Figure 1.5(c), has a cross section four times smaller than the dominant t-channel, but a larger jet multiplicity, so that these events would pass more easily the $t\bar{t}$ event selection compared to the t-channel. Both effects may compensate and result in a non negligible background.

3.1.5 W + Light Jets Background

One of the Feynman diagram of this process is represented in Figure 3.3. The production cross section of the W boson is large compared to the signal and, in the leptonic decay of the W boson results in a large $\not{E}_T$ signature. However, $t\bar{t}$ typically presents high jet and b-jet multiplicities, which is in average much lower in the case of the W + jet process. However a correct estimation of the production rate of multiple jets will be very important. The Matrix Element (ME) calculations of the jet production work well with high p_T and non-collinear jets but are particularly sensitive to scale uncertainties and divergent at low jet energies. On the other hand, the Parton Shower (PS) models reproduce better the low p_T and collinear jets region but yield a too soft p_T spectrum of the partons obtained. To accommodate both solutions to the range where each one works better, the W+jets samples were generated with `ALPGEN` [56] (version 2.06), that computes the matrix element from the hard scattering process, considering the leading-order W production diagram plus the tree-level diagrams with extra parton radiation. This production is then interfaced with `HERWIG` 6.5 and `JIMMY` v4. Results from Tevatron show that this technique of mixing the ME computation with the PS is in good agreement with data [60].

The difficulty when integrating both techniques (`ALPGEN` and `HERWIG`) arises from the double counting of events. For example, an event with three partons from the ME and two partons from the hadronisation may be duplicated if another event with two partons from the ME and three partons from the hadronisation produces the partons in the same phase space than the first event. The solution adopted is the called MLM matching [61] that uses a convention to decide which part of the multijet phase space is generated by the ME and which one is generated by the hadronisation. The ME generates events with the following kinematical cuts:

$$p_T^{part} > p_T^{min} \; ; \;\; \Delta R_{ij} > R_{min} \tag{3.1}$$

where p_T^{part} is the transverse momentum of the final state partons and ΔR_{ij} is their minimal separation in the (η, ϕ) plane. Events with partons in the rest of the phase space are generated by the PS through the following procedure: The events are showered using `HERWIG` and a jet

cone algorithm is applied to the partons produced in the perturbative phase of the shower with the following parameters: R_{clus} the cone size of the jet, E_T^{clus} the minimum transverse energy and η_{max}^{clus} the maximum pseudo-rapidity. Starting from the hardest parton generated by the ME, if there is jet within a distance in ΔR smaller than $1.5 \times R_{clus}$ to a given parton, then we say that the parton and the jet match.

If any of the partons does not match a jet, then the event is rejected. If there are more jets in the event than partons (that match a jet) the event is rejected as well.

The parameters used in the W+jets samples are $R_{min} = 0.7$; $p_T^{min} = 15$ GeV for the ME generation and $R_{clus} = 0.7$, $E_T^{clus} = 20$ GeV, $\eta_{max}^{clus} = 6.0$ for the MLM matching.

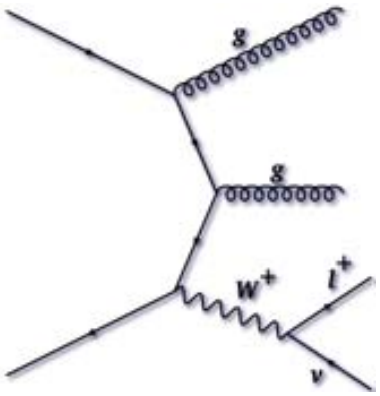

Figure 3.3: Feynman diagram for W + jets processes.

3.1.6 $Wb\bar{b}$ + Jets Background

The lowest order Feynman diagram of the $Wb\bar{b}$ + Jets process is represented in Figure 3.4. Due to the b-tagging requirement, most of the events that pass the event selection will contain a real b quark in the process. The W + light jets sample includes u,d,s and c quarks, so that only b quarks produced in the PS process will be included. A specific $Wb\bar{b}$ + Jets sample was produced using the same generator, `ALPGEN`, to generate b quarks with ME. Double counting with the W + light jets sample is suppresed by the MLM matching that actively kills events containing PS partons with $p_T > 20$ GeV and $\Delta R_{ij} > 0.7$. Both samples are complementary and covers the full phase space of $b\bar{b}$ production. Single b quark production is not included but should be small since it is related to F_b^L at high x that is tiny.

3.1.7 QCD Multijet Background

While QCD multijet processes have not a similar physics signature to $t\bar{t}$ with hadronic τ's in the final state, its cross section is so large that it may affect dramatically the S/B in case the $\not\!\!E_T$, τ and b-tagging are observed due to misidentification. Figure 3.5 shows one of the Feynman diagram of a QCD multijet process.

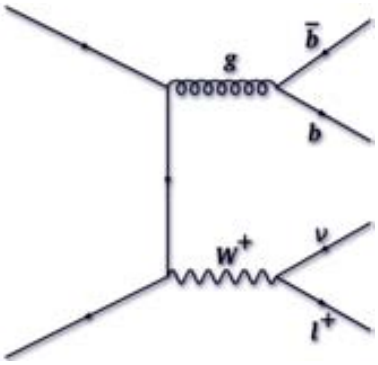

Figure 3.4: Feynman diagram for $W + b\bar{b}$ processes.

In addition to the uncertainty in the production rate of jets associated to the hard scattering, already mentioned in Section 3.1.5, the QCD multijet processes have a large uncertainty in its cross section, due mainly to the PDF uncertainties in the range of energies of the LHC collisions.

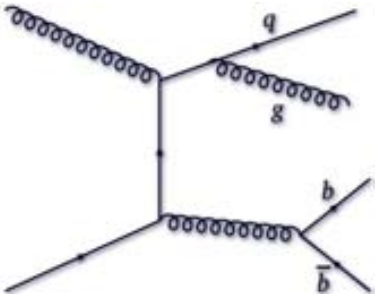

Figure 3.5: Feynman diagram for QCD multijet processes.

As the QCD multijet cross section decays exponentially with the p_T of the two leading jets, the production of QCD samples was split in different energy ranges, in order to have enough statistics of events with high energy jets, that will be very important for the analysis, as they will produce high $\not{E}_T$ signatures as well as a high jet energy profile. Four different samples were produced with Q^2 in the range 70 GeV $-$ 140 GeV, 140 GeV $-$ 280 GeV, 280 GeV $-$ 560 GeV and 560 GeV $-$ 1120 GeV. All samples were generated with `PYTHIA` (version 6.323).

3.2 ATLAS Simulation

A detailed simulation of the detector is carried out through the GEANT4 [62] [63] package which, in addition to accurately describing the detector geometry and tracking particles through it, is used to describe the materials constituting the detector, to visualize the detector components and to simulate and record the response of the sensitive elements of the various systems.

However, the study of some background rates for specific channels requires high statistics Monte Carlo samples which can not be achieved with the full GEANT4 simulation due to its

large CPU consumption. To accomplish the requirements of the high statistics studies of complex background processes, a fast particle-level simulation and reconstruction was developed from a parametrization extracted from the full simulation, called `ATLFAST` [64].

Section 3.2.1 describes the full GEANT4 simulation and Section 3.4 briefly summarizes the fast simulation characteristics.

3.2.1 GEANT4 Simulation

Every particle generated at the event generation step is propagated through the full ATLAS detector by GEANT4, which will compute a large number of physics processes occurring within all parts of the detector. Secondary tracks produced in any given interaction are propagated as well through the full detector. For the majority of the ATLAS detector, the range cuts[2)] take a default value of 1 mm (with some exceptions [65]). Finally the energies deposited in the sensitive volumes of the detector are recorded as "hits", containing the total energy deposition, position and time, and are written to a simulation output file which will seed the reconstruction software.

In addition to the "hits", the information called "truth" (from both generation and simulation) is also recorded for each event. In the generation, the truth is a history of the interactions from the generator, including incoming and outgoing particles. During the simulation, far too many secondary tracks are produced to store the information of every interaction. Only the truth information from those interactions which are of greatest relevance to physics analyses are saved. The truth information of the Monte Carlo simulation is of great importance for a physics analysis, to set a reference for performance measurements like particle identification efficiencies, energy calibrations, etc.

A comparison with the test-beam data shows very good agreement with the GEANT4 simulation, normally at the level of 1% or better [66].

To simulate pile-up, various types of events are read in, and hits from each type are overlaid. The different types of events considered comprise signal, minimum bias, cavern background, beam gas and beam halo events. The number of events of each type to overlay is a function of the luminosity to be simulated, for the number of interactions per bunch crossing, for example 23 at the design luminosity of 10^{34} cm^{-2} s^{-1} with 25 ns bunch spacing, depends linearly on luminosity and bunch spacing. However, this number follows a Poisson distribution with a long tail beyond the most probable value. Thus, a substantial fraction of the bunch crossings will have more than the average number of interactions. In addition, the ATLAS subdetectors are sensitive to hits produced several bunch crossings before and after the bunch crossing that contains the hard scattering event. All these effects are taken into account during the pile-up event merging.

[2)] The range cuts are GEANT4 parameters that control the creation of secondary electrons or photons during Bremsstrahlung and ionization processes. If the expected range of the secondary is less than some minimum value, the energy of that secondary particle is deposited at the end of the step where the primary was about to produce the secondary and no separate secondary is produced.

Due to the large CPU and disk consumption of the GEANT4 simulation, large scale productions are done on the LHC Computing Grid [65].

3.3 Reconstruction

This section presents a brief account of the ATLAS reconstruction of the objects which are used in this analysis.

3.3.1 Truth Jets

Truth jets are jets built by any of the jet reconstruction algorithms (see Section 3.3.5) using stable Monte Carlo particles produced by the fragmentation model in the physics generator as the ingredients that will conform the jet (instead of the usual calorimeter clusters). Therefore they are only available in simulated events. Those particles with a laboratory lifetime larger than 10 picoseconds are considered stable in ATLAS. These truth jets represent the reference for performance and calibration studies.

3.3.2 Electron

The ATLAS detector and reconstruction software have been designed with an excellent electron identification capability for many channels of new physics (with electrons in the final state) which have small cross sections and suffer from large QCD background. The ratio between the rate of isolated electrons and the rate of QCD jets with p_T in the range $20-50$ GeV is expected to be $\sim 10^{-5}$ at the LHC, almost two orders of magnitude smaller than at the Tevatron $p\bar{p}$ collider. Therefore to reach an acceptable performance the electron identification capability has to be two orders of magnitude better than what has been achieved so far.

Two types of reconstruction algorithms for electrons are implemented at present in the ATLAS software:

- The calorimeter-seeded reconstruction, which is seeded from electromagnetic (EM) clusters, and then builds identification variables based on information from the inner detector and the EM calorimeters.

- The tracking-seeded reconstruction, which is seeded from inner detector tracks, selects good-quality tracks that match (in position) an isolated deposition of energy in the EM calorimeters. The identification variables are then calculated in the same way as in the calorimeter-seeded reconstruction. This algorithm is optimized for low p_T and non-isolated electrons, with energies as low as a few GeV.

The algorithm used in the analysis, described in this section, is the calorimeter-seeded algorithm, that is the default algorithm for non low p_T electrons. The reconstruction starts from an electromagnetic tower with transverse energy above 3 GeV. Then a track is searched for among all reconstructed tracks (not belonging to a photon conversion pair in the inner detector), which

after extrapolation to the EM calorimeter is required to match the cluster within a window of 0.05×0.10 in $\Delta\eta \times \Delta\phi$. The ratio of the energy of the cluster to the momentum of the track, E/p, is required to be smaller than 10. After these requirements on the electron reconstruction, approximately 93% of true isolated electrons with $E_T > 20$ GeV and $|\eta| < 2.5$ are kept, the main cause of the inefficiency being the large amount of material in the inner detector and therefore η dependent. The η region above 2.5 is out of the acceptance of the inner detector, and therefore there is no possibility of using tracks in this region. Even if electron identification in the forward region, $|\eta| > 2.5$, (very important in many physics analysis with specific topologies) is possible using cut-based methods with calorimeter variables only; it is not considered in this analysis.

There are several techniques to identify electrons from the candidate reconstructed with the calorimeter-seeded algorithm, trying to maximize the jet rejection by combining calorimeter, track quantities and the TRT information. Although advanced identification methods, such as likelihood discriminants, have been developed for electron identification in the ATLAS software, a simple cut based identification procedure is used in this analysis, for it provides a robust solution, specially important with early data.

The cuts have been optimised in up to seven bins in η and up to six bins in p_T. The electron reconstruction software provides three reference sets of requirements: loose, medium and tight. In a compromise between low fake rate and not too low efficiency on signal the medium set of cuts was chosen for this analysis.

The loose cuts are applied on the hadronic leakage (ratio of E_T in the first sampling of the hadronic calorimeter to E_T of the EM cluster) and on several shower shape variables (ratio in η of cell energies in 3×7 versus 7×7 cells and the same ratio in ϕ) extracted from the middle layer of the EM calorimeter. These cuts provide a good signal efficiency but poor jet rejection. To improve the discrimination of jets, the medium set of cuts incorporate additional requirements on the strips in the first layer of the EM calorimeter and on the tracking variables. The strip based cuts are effective in the rejection of $\pi^o \to \gamma\gamma$ decays since the energy deposit pattern from π^o's is often found to have two maxima due to the pair of photons. The variables considered are $\Delta E_S = E_{max2} - E_{min}$, the difference between the energy associated with the second maximum E_{max2} and the energy reconstructed in the strip with the minimal value, found between the first and second maxima E_{min}; $R_{max2} = E_{max2}/(1 + 9 \times 10^{-3} E_T)$ where E_T is the transverse energy of the cluster in the EM calorimeter; the shower width over the strips and the fraction of energy deposited outside the shower core of three central strips.

The tracking variables are the number of hits in the pixels, the number of silicon hits (pixels detector and SCT) and the transverse impact parameter.

The medium cuts increase the jet rejection by a factor 3-4 with respect to the loose cuts while reducing the signal efficiency by $\sim$10%. Figure 3.6 shows the efficiency of the medium cuts used in this analysis for electron identification.

The jet rejection achieved with the medium cuts, computed on simulated di-jet and minimum-bias samples with $E_T > 17$ GeV is 2184 ± 13.

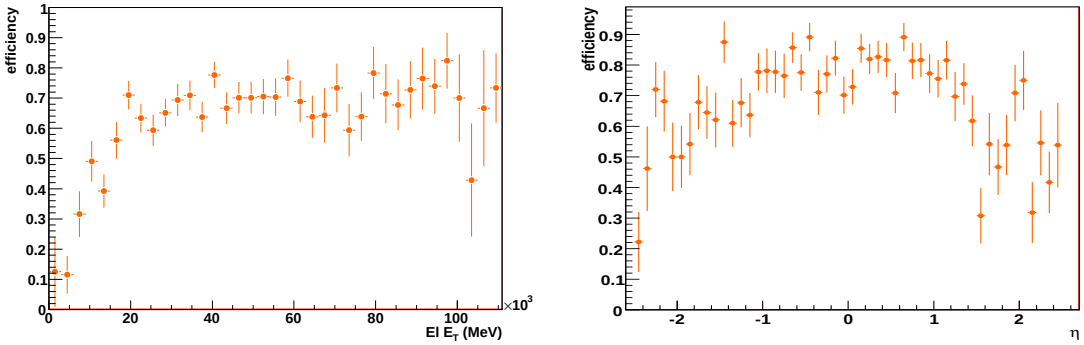

Figure 3.6: Identification efficiencies for isolated electrons that decay from a W boson on $t\bar{t}$ events using the medium cuts versus E_T (left) and η (right).

3.3.3 Muon

The direct strategy to reconstruct muons in ATLAS is the so called *standalone* muon reconstruction that consists in finding tracks in the muon spectrometer and extrapolating them to the beam line. However muons leave their signatures in all of the detector subsystems including the inner detector, calorimeters and the muon spectrometer. Therefore, an optimal muon identification and measurement is obtained when information from each subsystem is used by the reconstruction algorithm. *Combined* muons are found by matching standalone muons to nearby inner detector tracks and then combining the measurements from the two systems. *Tagged* muons are found by extrapolating inner detector tracks to the spectrometer detectors and searching for nearby hits. The current ATLAS software includes two muon reconstruction algorithms of each type. This analysis uses the Staco algorithm, which uses the *combined* muon strategy, that is currently the default for physics analysis.

3.3.4 Hadronic Tau

Two complementary algorithms for the reconstruction of hadronic τ decays are implemented in the ATLAS offline reconstruction software: the calorimeter-based approach and the tracking-based approach.

As this analysis uses only the calorimeter-based algorithm for τ identification, for it provides a lower τ fake rate, this section only describes the calorimeter-based approach (see ref. [67] for more details on both τ identification approaches).

In the calorimeter-based approach, the hadronically decaying τ candidates are reconstructed using calorimeter clusters as seeds. They are obtained from a sliding window clustering algorithm [68] applied to so called calorimeter towers which are formed from cells of all calorimeter layers on a grid of size $\Delta\eta \times \Delta\phi = 0.1 \times 2\pi/64$. The energy and position of the tau candidate is calculated from the clusters, where a threshold of 15 GeV is applied to the transverse energy of the cluster.

All cells within $\Delta R < 0.4$ around the barycenter of the cluster are calibrated with an H1-style calibration [69], and later used to compute shower shape variables suitable to discriminate hadronic τ decays from fake candidates originating from QCD jets. The H1-style calibration applies a weight to each cell that is a function of the cell energy density, η and the calorimeter region. These weights were optimized for QCD jets, and work satisfactory well for hadronically decaying τ (see paragraph on jet calibration in Section 3.3.5).

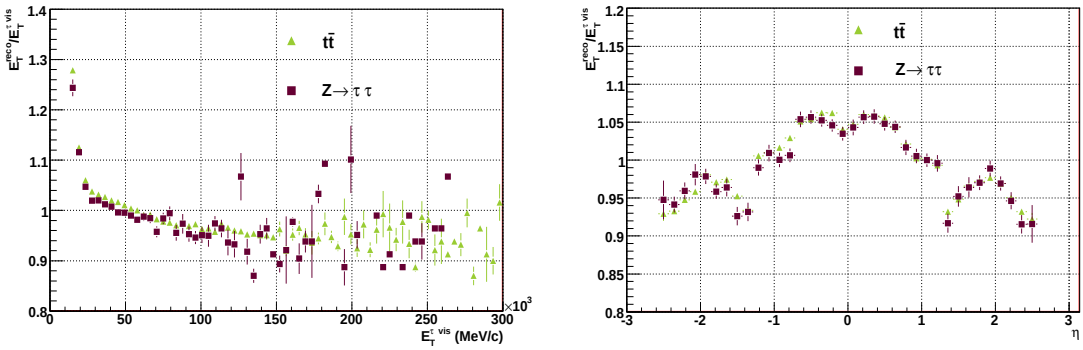

Figure 3.7: Ratio of reconstructed transverse energy (E_T^{reco}) and true transverse energy of the visible products of the hadronic τ decay ($E_T^{\tau vis}$) calculated as a function of p_T of the visible products of the τ for $\eta < 2.5$ (left) and as a function of η for $E_T^{\tau vis} > 25$ GeV (right) for taus from $Z \to \tau\tau$ (squares) and $t\bar{t}$ (triangles).

The tau energy scale (ratio of reconstructed transverse energy of the τ and true transverse energy of its visible products) is shown in Figure 3.7 as a function of the transverse energy of the τ and η.

Several quantities that show a different behaviour between hadronically decaying τ and QCD jets are combined in a likelihood function. These quantities are described in the following:

- Electromagnetic Radius. Hadronically decaying τ's have a smaller shower profile than QCD jets, that can be exploited with the electromagnetic radius defined as:

$$R_{em} = \frac{\sum_{i=1}^{n} E_{T,i}\sqrt{(\eta_i - \eta_{cluster})^2 + (\phi_i - \phi_{cluster})^2}}{\sum_{i=1}^{n} E_{T,i}} \tag{3.2}$$

  where i runs over all cells in the electromagnetic calorimeter within $\Delta R < 0.4$ from the barycenter of the cluster. This variable shows good discrimination power at low E_T but becomes less effective at high E_T.

- Isolation in the Calorimeter.

  Clusters from hadronically decaying τ's are more collimated than those produced by QCD jets, and therefore an isolation variable can be used in order to discriminate them. The calorimeter-based algorithm for τ reconstruction uses the isolation variable defined in a ring of $0.1 < \Delta R < 0.2$

$$\Delta E_T^{12} = \frac{\sum_i^{0.1<\Delta R<0.2} E_{T,i}}{\sum_j^{\Delta R<0.4} E_{T,j}} \tag{3.3}$$

Typically hadronically decaying τ's yield narrower showers in the calorimeters than QCD jets and then the isolation variables are expected to take smaller values for τ's compared to jets.

- Charge of the τ candidate.

  The charge of the τ candidate is defined as the sum of the charges of the tracks associated to the cluster. The misidentification of the charge (different from ± 1) of τ's is at the level of a few percent, while QCD jets may have higher values from the sum of the charges of different tracks associated to the cluster.

- Number of associated tracks.

  This variable computes the number of tracks that match the calorimeter cluster within $\Delta R < 0.3$. The tracks are required to have a $p_T > 2$ GeV. Most of the hadronically decaying τ's will be 1-prong (τ's decaying hadronically with one charged particle among the decay products) in 74% of the cases, and 3-prong (τ's decaying hadronically with three charged particles among the decay products) in 23% of the cases (see Table 3.2). Therefore it is expected that most of the reconstructed τ's show a track multiplicity between 1 and 3, while QCD jets have a higher associated track multiplicity due to fragmentation.

- Number of hits in the η strip layer.

  The first layer of the electromagnetic barrel calorimeter (the *strip detector*) is finely segmented in the η direction. Cells with energy above 200 MeV and within $\Delta R < 0.4$ from the center of the cluster are counted as hits in the strip layer. A significant fraction of hadronically decaying τ's deposit very little energy in this layer (in contrast to QCD jets), and the number of hits is therefore small.

- Transverse energy width in the η strip layer

  This variable defined as

$$\Delta\eta = \sqrt{\frac{\sum_{i=1}^{n} E_{T,i}^{strip} \cdot (\eta_i - \eta_{cluster})^2}{\sum_{i=1}^{n} E_{T,i}^{strip}}} \tag{3.4}$$

  measures the spread in η (weighted by the cell energy) of clusters in the strip layer, where the sum runs over all strip cells within $\Delta R < 0.4$. Since τ's produce more collimated clusters than QCD jets in the calorimeter they are expected to follow a narrower distribution for this variable compared to jets.

- E_T over p_T of the leading track.

Hadronically decaying τ's expect to pass a large fraction of its energy to the leading track. Therefore the ratio of the cluster energy E_T to the momentum of the leading track p_{T1} is expected to be close to 1, while QCD jets are expected to show a more uniform distribution of the energy among all the tracks. QCD jets are also expected to have more additional neutral particles associated to the jet, decreasing the ratio E_T/p_{T1}.

Table 3.2: Different decay modes of a τ lepton which are clasified in leptonic decay, single-prong, three-prong, five-prong and other modes.

Decay modes	**Branching ratio**
$\tau \rightarrow e\nu_e\nu_\tau$	17.8 %
$\tau \rightarrow \mu\nu_\mu\nu_\tau$	17.4%
$\tau \rightarrow h^{\pm}neutr.\nu_{tau}(single-prong)$	48.2%
$\tau \rightarrow \pi^{\pm}\nu_\tau$	10.9%
$\tau \rightarrow \pi^{o}\pi^{\pm}\nu_\tau$	25.5%
$\tau \rightarrow \pi^{o}\pi^{o}\pi^{\pm}\nu_\tau$	9.2%
$\tau \rightarrow \pi^{o}\pi^{o}\pi^{o}\pi^{\pm}\nu_\tau$	1.0%
$\tau \rightarrow K^{\pm}neutr.\nu_\tau$	1.6%
$\tau \rightarrow h^{\pm}h^{\pm}h^{\pm}neutr.\nu_\tau(three-prong)$	15 %
$\tau \rightarrow \pi^{\pm}\pi^{\pm}\pi^{\pm}\nu_\tau$	9.0 %
$\tau \rightarrow \pi^{o}\pi^{\pm}\pi^{\pm}\pi^{\pm}\nu_\tau$	4.5 %
$\tau \rightarrow \pi^{o}\pi^{o}\pi^{\pm}\pi^{\pm}\pi^{\pm}\nu_\tau$	0.5 %
$\tau \rightarrow \pi^{o}\pi^{o}\pi^{o}\pi^{\pm}\pi^{\pm}\pi^{\pm}\nu_\tau$	0.1 %
$\tau \rightarrow K^{o}_{S}X^{\pm}\nu_\tau$	0.9 %
$\tau \rightarrow (\pi^{o})\pi^{\pm}\pi^{\pm}\pi^{\pm}\pi^{\pm}\pi^{\pm}\nu_\tau(five-prong)$	0.1 %
other modes with K	1.3%
others	0.03%

Figure 3.8 shows some of the variables used for τ identification for τ's and QCD jets. The τ identification is performed through a one-dimensional likelihood ratio constructed from these variables. Tau identification efficiencies and jet rejections will depend on the likelihood value selected.

For a $t\bar{t}$ event, where the jet multiplicity is very high, it is very important to keep the jet rejection at high values, in order to have reasonable purities in the τ sample. A likelihood cut greater than 4, provides a τ efficiency of 50% in the plateau and acceptable jet rejection factors ($\sim$ 100 for QCD jets in the range 30-50 GeV) as can be seen in Figures 3.9 and 3.10.

The τ efficiency and rejection factor (per energy bin) are defined as follows:

$$\text{Eff} = \frac{\text{Number identified } \tau\text{'s}}{\text{Number true } \tau's} \tag{3.5}$$

$$\text{Rejection factor} = \frac{\text{Number jets misidentified as } \tau}{\text{Number truth jets}} \tag{3.6}$$

where the rejection factor definition can be normalized to different type of truth jets (Sec-

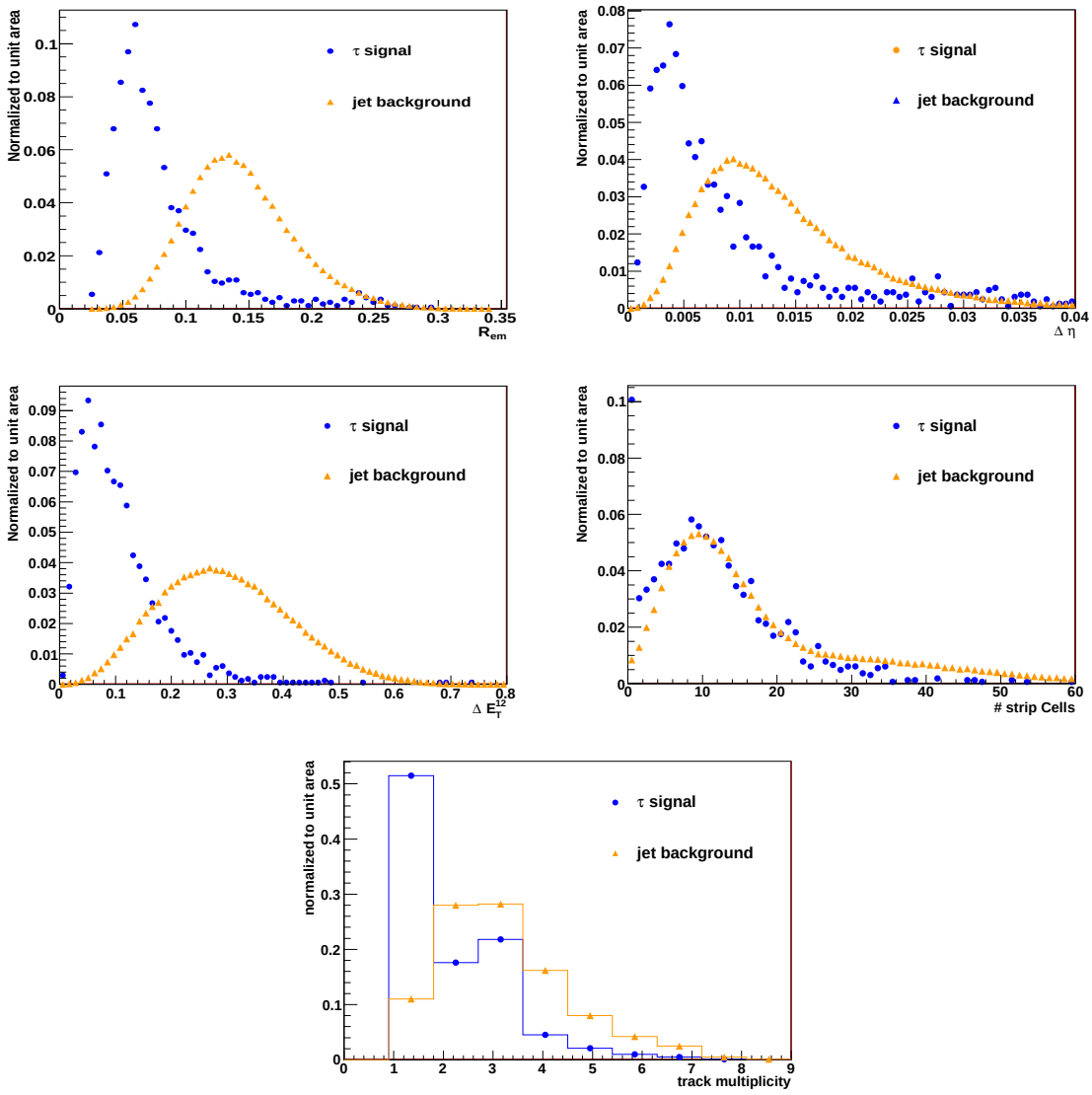

Figure 3.8: Some of the variables used in the calorimeter-based algorithm for tau identification, for hadronic τ decays (from a $Z \rightarrow \tau\tau$ sample) (circles) and QCD jet background (triangles). From top-left to bottom-right: electromagnetic radius, transverse energy width in the η strip layer, energy isolation in the electromagnetic calorimeter, number of hits in the strip layer of the calorimeter and track multiplicity.

tion 3.3.1), like heavy flavour jets or light jets from the W boson decay ($W \rightarrow q\bar{q}$) in $t\bar{t}$ events.

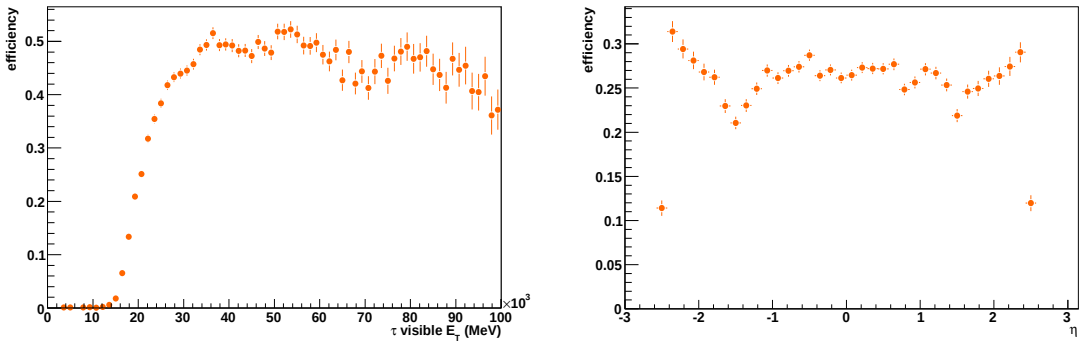

Figure 3.9: τ identification efficiencies for $t\bar{t}$ events using a likelihood cut greater than 4 as a function of the τ visible energy (left) and η (right). The efficiency on the right plot is $\lesssim 0.3$ while the plateau on the efficiency versus p_T plot is at 0.5 due to the soft spectrum of τ's present in $t\bar{t}$ events.

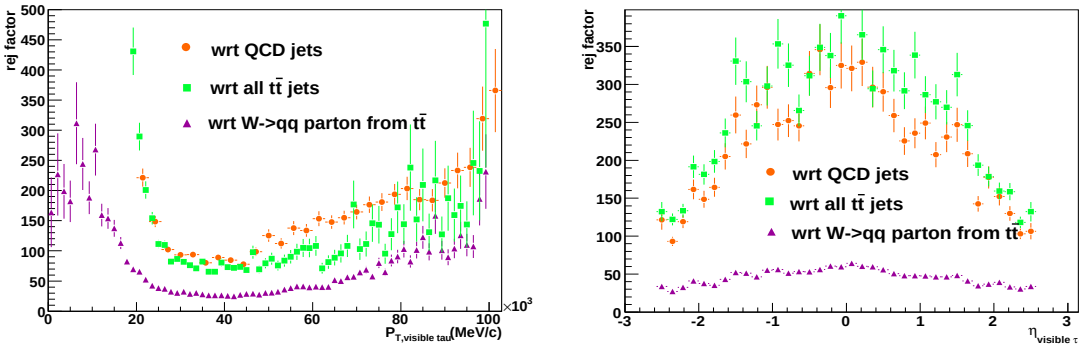

Figure 3.10: τ rejection factor for $t\bar{t}$ events using a likelihood cut greater than 4 as a function of p_T (left) and η (right). The rejection factor depends on the "type" of jet taken as a reference. These plots consider QCD jets (circles), any truth jet found in a $t\bar{t}$ event (squares) and light jets that decay from a W boson produced in the decay of one of the tops of a $t\bar{t}$ event (triangles).

3.3.5 Hadronic Jet

Implementations of all relevant jet finding algorithms are available in the ATLAS reconstruction software, including the most commonly used: the seeded fixed cone finder with split and merge and the k_T algorithm (Refs [70], [71]). To reconstruct events with very busy final state like $t\bar{t}$, narrow jets are the preferred choice. In this analysis, a fixed cone with size 0.4 jet finding algorithm has been chosen.

The main element that will form a jet is the *tower*: a set of cells in the electromagnetic and hadronic calorimeters that belong to the same bin in η/ϕ. The tower bin size is $\Delta\eta \times$

$\Delta\phi = 0.1 \times 0.1$ in the whole acceptance of the calorimeters, $|\eta| < 5$ and $-\pi < \phi < \pi$ with $100 \times 64 = 6400$ towers in total. The seed is the tower with the highest p_T, that must be above a given threshold: 1 GeV. Every tower within a cone in pseudorapidity η and azimuth ϕ with $\Delta R = \sqrt{\Delta\eta^2 + \Delta\phi^2} < 0.4$ is combined with the seed.

A new direction of the jet is recomputed from the four momenta (weighted by their energy) of all towers inside the initial cone, and the neighbour towers that will compose the jet have to be recomputed again. This procedure continues in an iterative process until the direction of the jet does not change significatively.

Finally, there is a split/merge technique to be applied after all jets in the event are been built in order to make this algorithm infrared safe. If two jets are very close to each other, and they share more of 0.5 the p_T of the less energetic jet, they are merged. Otherwise they will be split into two separate jets.

Calorimeter Jet Calibration

Jets are calibrated using the cell-based H1 [69]) calibration schema, that applies an energy density dependent weight to the energy of every cell in the jet. The motivation behind the H1 calibration is that low signal densities in the calorimeter cells indicate a hadronic signal in a non-compensaing calorimeter and thus need a signal weight for compensation of the order of the electron/hadron signal ratio e/h, while the high signal densities are more likely generated by electromagnetic showers and therefore do not need additional signal weighting.

The weighting factor is ~ 1 for high density signals, rising up to 1.5, the typical e/π for the ATLAS calorimeters, with decreasing cell signal densities. The calibrated jet four-momentum is then recalculated from the weighted cell energies.

3.3.6 B-Jet Tagging

The identification of b-jets takes advantage of several of their properties which allow us to distinguish them from jets which contain only lighter quarks. The fragmentation is hard and the b-hadron retains about 70% of the original b quark momentum. As the mass of the b-hadrons is relatively high (> 5 GeV), their decay products may have a large transverse momentum with respect to the jet axis and the opening angle of the decay products is large compared to the jets that contain only light quarks. And finally, the relatively long lifetime of hadrons containing a b quark, of the order of 1.5 ps ($c\tau \sim 450\ \mu$m) is very helpful to identify secondary vertices that indicate the presence of a b-quark in the jet. A b-hadron in a jet with $p_T = 50$ GeV will therefore have a significant flight path length, travelling on average about 3 mm in the transverse plane before decaying. There are two approaches in the ATLAS reconstruction software to identify b-jets. One is based on the impact parameter, d_o, that is the distance of the closest approach of the track to the primary vertex point, in the $r - \phi$ projection. The tracks from b-hadron decay products tend to have rather large impact parameters which can be distinguished from tracks stemming from the primary vertex. The second approach is to reconstruct explicitly the

displaced secondary vertex.

The b-tagging identification used in this analysis is based on a likelihood which is a combination of the information provided by the two methods.

The tracks reconstructed in the ATLAS inner detector are the main ingredient for the b-tagging. The ATLAS tracker is able to measure efficiently and with good accuracy the tracks within $\eta < 2.5$ and down to $p_T \sim 500$ MeV. For a central track with $p_T = 5$ GeV, which is typical for b-tagging, the relative transverse momentum resolution is around 1.5% and the transverse impact parameter resolution is about 35 μm.

The resolution of the impact parameter (extracted from the σ of a fit to a Gaussian distribution) is reported on Figure 3.11 for all tracks in $t\bar{t}$ events that pass the b-tagging quality cut[3)] and match a good Monte Carlo track.

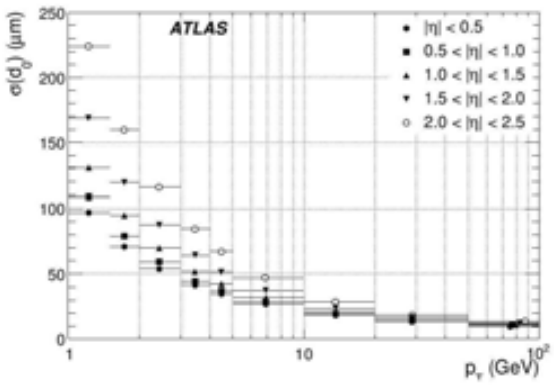

Figure 3.11: Track impact parameter resolution (from $t\bar{t}$ events) versus track p_T for several bins in the track pseudo-rapidity.

Another key ingredient for b-tagging is the primary vertex of the event. The impact parameters of tracks are recomputed with respect to its position and tracks compatible with the primary vertex are excluded from the secondary vertex searches. The efficiency to find the primary vertex is very high in the high p_T events of interest, and the resolution on its position is around 12 μm in each transverse direction and 50 μm along z axis. With pile-up, the presence of additional minimum bias vertices makes the choice of the primary vertex less trivial: at a luminosity of $2\times10^{33}\text{cm}^{-2}\ \text{s}^{-1}$ (on average 4.6 minimum bias events per bunch crossing) a wrong vertex can be picked up as the primary vertex in about 10% of the cases, causing a deterioration in the b-jet tagging efficiency.

In order to extract the b-tagging likelihood ratio, the measured value S_i of a discriminating variable is compared to pre-defined smoothed and normalized distributions for both the b- and light jet hypotheses, $b(S_i)$ and $u(S_i)$. The ratio of the probabilities $b(S_i)/u(S_i)$ defines the

[3)] The b-tagging quality track is designed to select well-measured tracks and reject fake tracks and tracks from long-lived particles. It requires at least seven precision hits in the inner detector, at least two hits in the pixel detector, the impact parameter $d_0 < 1$ mm and $|z_o - z_{pv}|\sin\theta < 1.5$ mm, where z_{pv} is the longitudinal location of the primary vertex. Only tracks with $p_T > 1$ GeV are considered

weight, represented on Figure 3.12. To select b-jets, a cut value on this weight must be chosen, corresponding to a given efficiency.

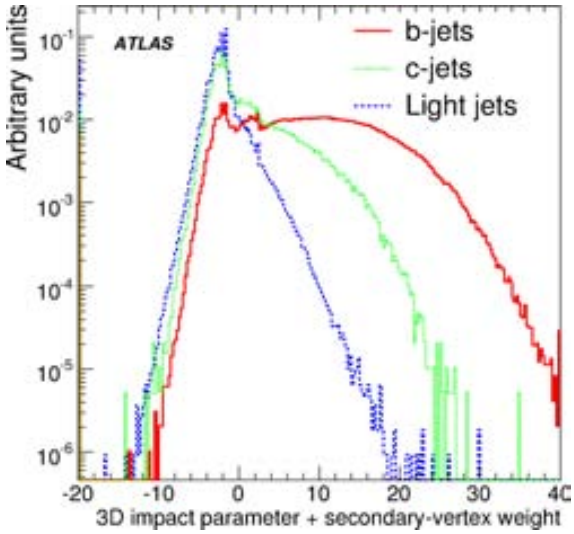

Figure 3.12: b-tagging likelihood distribution for b-jets, c-jets and light jets. The algorithm combines variables using the impact parameter and secondary vertex reconstruction.

An optimum performance of the b-jet algorithms requires a specific calibration of the jets and to extract the likelihood reference distributions with large purified samples of b-jets, as well as a good understanding of the ATLAS inner detector, specially concerning the tracking resolution, given the importance of the ATLAS tracking in the b-tagging reconstruction. All the ingredients to have an optimum b-tagging performance will take time, and we can expect a non perfect b-tagging performance with the ATLAS early data, which will be improved with time. There exists specific methods developed to evaluate the b-tagging performance directly from data $t\bar{t}$ events with 100 pb^{-1} of data [72].

Given the importance of the b-tagging for this analysis to reduce the physics background, we have considered two different scenarios. A loose b-tagging scenario uses a *weight* cut greater than 3, which provides an efficiency on signal of about 80% but a poor light jet rejection, as can be seen on Figures 3.13 and 3.14. This scenario represents the hypothesis for an early stage of the detector when the b-tagging is not perfectly understood and therefore the jet rejection is far from being ideal.

The second scenario uses a *weight* cut greater than 7.05, that provides an efficiency on signal of about 60% and a much higher jet rejection, shown on Figures 3.13 and 3.15. This is a realistic hypothesis after some time of data taking and a good understanding of the inner detector.

3.3.7 Missing Transverse Energy

The missing transverse energy plays an important role in the $t\bar{t}$ semileptonic analyses, as $t\bar{t}$ events contain a real source of missing transverse energy from the neutrino that decays from the leptonic

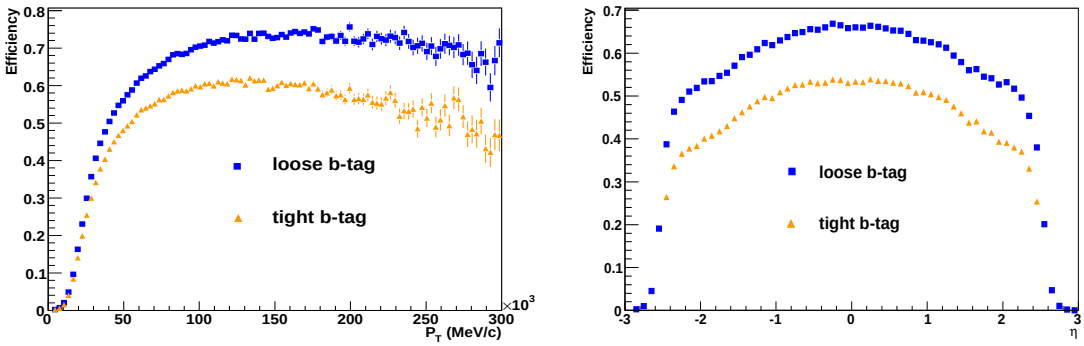

Figure 3.13: b-tagging efficiencies as a function of p_T (left) and η (right) for loose (blue squares) b-tagging selection (weight > 3) and tight (orange triangles) b-tagging selection (weight > 7.05). The efficiencies are normalized to true b-quarks from $t \to b\,W$ in $t\bar{t}$ events.

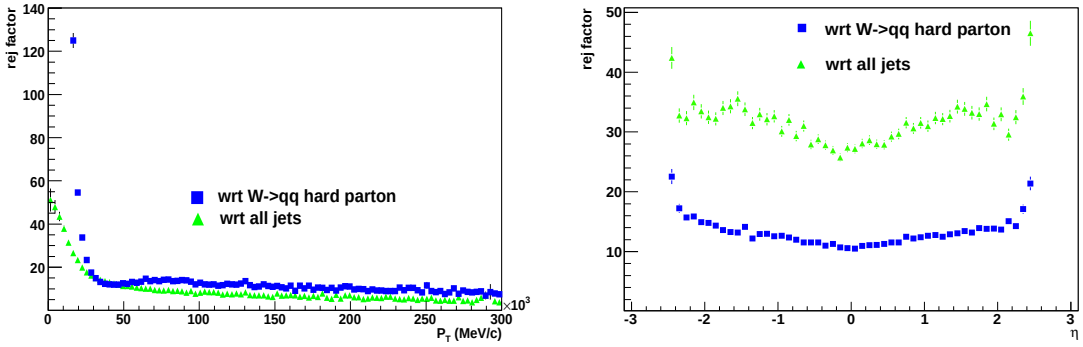

Figure 3.14: b-tagging rejection factor as a function of p_T (left) and η (right) for a loose b-tagging selection (weight > 3). The rejection factors are normalized to Monte Carlo light jets from $W \to qq'$ (blue squares) and to any Monte Carlo jet (green triangles) in $t\bar{t}$ events.

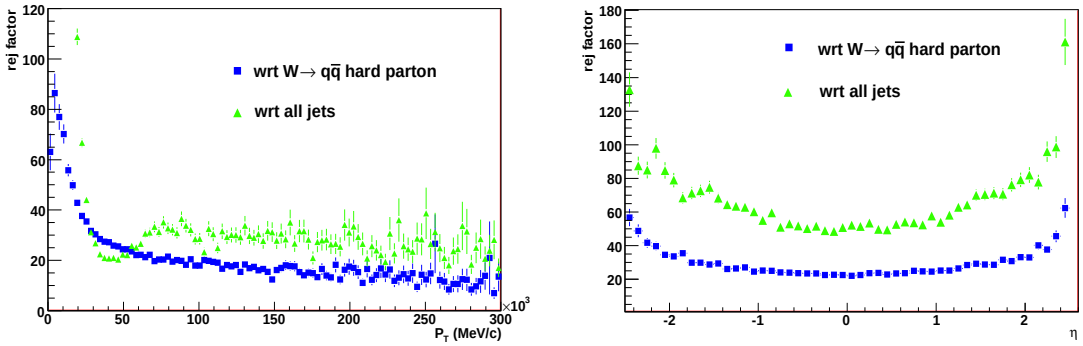

Figure 3.15: b-tagging rejection factor as a function of p_T (left) and η (right) for a tight b-tagging selection (weight > 7.05). The rejection factors are normalized to true light jets from $W \to qq'$ (blue squares) and to any Monte Carlo jet (green triangles) in $t\bar{t}$ events.

W boson. In the case of the τ channel, the neutrino produced in the decay of the hadronic τ introduces additional sources of missing transverse energy. This missing transverse energy expected in $t\bar{t}$ events is very useful to reject other background processes where no significant sources of missing transverse energy are expected, like QCD multijets and the fully hadronic decay channel of the $t\bar{t}$ process.

Even so, altough the ATLAS calorimeter extends to large pseudo-rapidity angles, there are inactive transition regions between different calorimeters that produce fake missing transverse energy ($\not\!\!E_T{}^{Fake}$), and in addition, dead and noise readout channels, if present, will also produce $\not\!\!E_T{}^{Fake}$ that can reduce the rejection power of this variable against fully hadronic processes.

The algorithm to compute the missing transverse energy starts from the energy deposites in calorimeter cells that survive a noise suppression procedure. The cells are calibrated using global calibration weights that depend on their energy density. Later corrections are applied to the muon energy and the energy lost in the cryostats.

The electronic noise alone in the $\sim 200K$ readout channels of the ATLAS calorimeter contributes about 13 GeV to the width of the $\not\!\!E_T$ distribution. Its suppression is specially important in those processes where there is no presence of large real $\not\!\!E_T$. To eliminate this noise, an energy threshold is applied to each cell, such that only those cells with $|E_{cell}| > 2 \times \sigma_{cell}^{noise}$, where σ_{cell}^{noise} is the width of the noise distribution (a combination of purely electronics noise and pile-up noise) for the given cell, will contribute to the missing transverse energy computation.

The total missing transverse energy is computed as the contribution from the energy deposited in the calorimeters, the contribution measured from muons and the correction for energy lost in the cryostat.

$$\not\!\!E_T{}_{x,y}^{Final} = \not\!\!E_T{}_{x,y}^{Calo} + \not\!\!E_T{}_{x,y}^{Cryo} + \not\!\!E_T{}_{x,y}^{Muon} \tag{3.7}$$

The term that computes the missing transverse energy from the energy deposited in the calorimeters is calculated as the sum of the energies of all the cells in the calorimeter that pass the noise threshold:

$$\not\!\!E_T{}_{x,y}^{Calo} = -\sum_{cells} E_{x,y} \tag{3.8}$$

The result, using cells calibrated to the electromagnetic scale, gives a large shift in the $\not\!\!E_T$ scale of about 30% with respect to $\not\!\!E_T{}^{True}$. To correct for this effect, an "H1-like" calibration is applied to each cell.

The $\not\!\!E_T$ muon term is calculated from the momenta of muons measured in the muon chambers in a large pseudo-rapidity region $\eta < 2.7$:

$$\not\!\!E_T{}_{x,y}^{Muon} = -\sum_{Muons} E_{x,y} \tag{3.9}$$

In the region $\eta < 2.5$ (within the coverage of the ATLAS inner detector) a further requirement of matching a track in the inner detector is applied in order to reduce the contribution from fake

muons. Due to the good identification efficiency and resolution of the ATLAS muon system, the muon term does not affect significantly to the $\not\!\!E_T$ resolution.

Finally the thickness of the cryostat between the LAr barrel electromagnetic calorimeter and the tile barrel hadronic calorimeter is about half an interaction length, where hadronic showers loose energy that is not measured in the calorimeters. The $\not\!\!E_T$ reconstruction recovers this loss of energy in the cryostat using the correlation of energies between the last layer of the LAr calorimeter and the first layer of the hadronic calorimeter. It uses the same technique applied to the cryostat correction for jet energies.

$$\not\!\!E_T{}_{x,y}^{Cryo} = -\sum_{Jets} Ejet_{x,y}^{Cryo} \tag{3.10}$$

where all reconstructed jets are summed in the event and

$$Ejet^{Cryo} = w^{Cryo}\sqrt{E_{EM3} \times E_{HAD1}} \tag{3.11}$$

w^{Cryo} being a cell dependent calibration weight and E_{EM3} and E_{HAD1} the jet energies in the third layer of the electromagnetic calorimeter and the first layer of the hadronic calorimeter respectively. The cryostat correction contributes about 5% per jet with p_T above 500 GeV.

The final step in the $\not\!\!E_T$ computation is the refinement of the calibration of cells associated with each high-p_T object. Calorimeter cells are associated with a parent reconstructed and identified high-p_T object in a chosen order: electrons, photons, muons, hadronically decaying τ's, b-jets and light jets. The calibration of these objects is known to higher accuracy than the global calibration, and therefore the refined calibration of the objects is used to substitute the global calibration of those cells that are part of the given object.

$$\not\!\!E_T{}_{x,y}^{Calo} = \not\!\!E_T{}_{x,y}^{RefCali} = -(\not\!\!E_T{}_{x,y}^{RefEle} + \not\!\!E_T{}_{x,y}^{RefTau} + \not\!\!E_T{}_{x,y}^{Refbjets} + \not\!\!E_T{}_{x,y}^{RefJets} + \not\!\!E_T{}_{x,y}^{RefMuo} + \not\!\!E_T{}_{x,y}^{RefOut}) \tag{3.12}$$

where $\not\!\!E_T{}_{x,y}^{RefOut}$ is the contribution from cells that are not included in any of the reconstructed objects.

The linearity of the missing transverse energy, defined as:

$$Linearity = (|\not\!\!E_T{}^{true}| - |\not\!\!E_T|)/|\not\!\!E_T{}^{true}) \tag{3.13}$$

where $\not\!\!E_T$ and $\not\!\!E_T{}^{true}$ are the reconstructed and the true $\not\!\!E_T$, respectively, is shown in Figure 3.16 for $A \to \tau^+\tau^-$ events.

The different improvements in calibrations and corrections to $\not\!\!E_T$ already described are summarized in the plot:

- The uncalibrated $\not\!\!E_T$ (using cell energies at the electromagnetic scale) shows a large systematic bias of 30%.

- The reconstructed $\not\!\!E_T$ based on globally calibrated cell energies and reconstructed muons

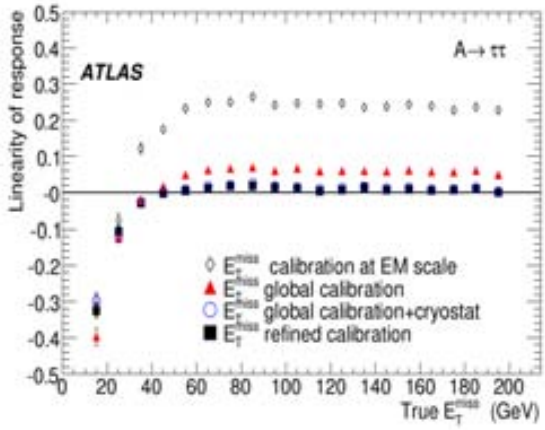

Figure 3.16: Linearity of response of reconstructed $\not\!\!E_T$ as a function of true $\not\!\!E_T$ for events with the Minimal Supersymmetry Standard Model Higgs, A, decaying into a couple of τ's ($A \to \tau^+\tau^-$) with $m_A = 800$ GeV.

improves the linearity up to a 5%.

- The addition of the cryostat correction reduces the linearity up to 1% level.
- Refined $\not\!\!E_T$ calibration with the specific calibration of reconstructed objects does not improve the linearity but gives a better resolution.

Figure 3.17 shows the $\not\!\!E_T$ resolution estimated from the width of the $\not\!\!E_{T_{x,y}} - \not\!\!E_{T_{x,y}}^{true}$ distribution as a function of the total transverse energy of the event ($\sum \not\!\!E_T$), emphasizing the dependence of the $\not\!\!E_T$ resolution on the total transverse energy of the event. The typical range of $\not\!\!E_T$ resolution for $t\bar{t}$ events is 10-15 GeV.

3.4 Fast Simulation and Reconstruction

The ATLAS fast simulation, `ATLFAST`, software goal is to perform a computationally fast simulation of the ATLAS detector response in order to be able to deal with statistically large samples of signal and background events for physics studies. To keep the CPU time per event at a reasonable level, no detailed simulations of any interactions of the particles in the detector are performed. Instead, it is based on a parametrization of the detector response, obtained through the full simulation results.

While full simulation is desirable to study the full extent of the detector effects, it is an intensive computing process that may take ~ 30 minutes for a typical SM event (for example a minimum bias will take an average time of 551 kSI2K seconds and a $t\bar{t}$ event will take about 1990 kSI2K seconds [65]) , using a large amount of RAM, CPU and disk space. The fast simulation, on the other hand, takes a small fraction of a second per event.

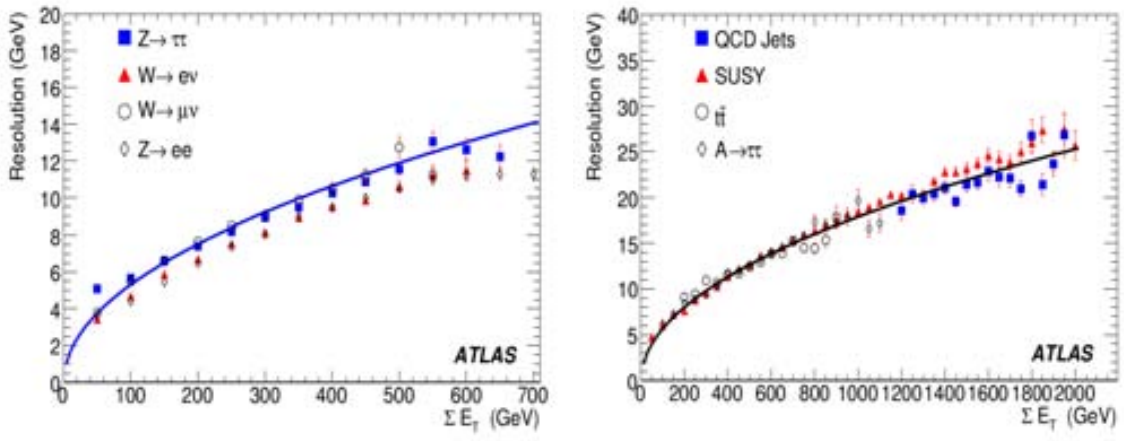

Figure 3.17: Resolution of the $\not\!\!E_T$ with refined calibration as a function of the total transverse energy, $\sum \not\!\!E_T$, for low to medium values (left) and for higher values (right) of the $\sum \not\!\!E_T$. The curves correspond to the best fits, $\sigma = 0.53\sqrt{\sum \not\!\!E_T}$, through the points from $Z \to \tau^+\tau^-$ (left) and $\sigma = 0.57\sqrt{\sum \not\!\!E_T}$, through the points from $A \to \tau^+\tau^-$ events (right). Points from $A \to \tau^+\tau^-$ events are for masses m_A ranging from 150 to 800 GeV and the points from QCD jets correspond to di-jet events with $560 < p_T < 1120$ GeV.

The ATLFAST program is an essential tool within the ATLAS software model. According to the Computing Technical Design Report [73], about 80% of the ATLAS Monte Carlo event production will be done using a fast simulation, since the computing power for a complete full simulation will not be available.

In particular, in this analysis, the ATLFAST simulation is needed for the evaluation of the QCD background. If the simulated statistics in full simulation for $t\bar{t}$ (of the order of the fb) and other SM backgrounds (see Table 3.1) is more than enough for a study with early data, this is not the case for QCD production. The cross section for QCD processes at the LHC collision energies is several orders of magnitude that of the $t\bar{t}$ signal and its simulation implies hundreds of millions of events, numbers that are not affordable for the ATLAS full simulation.

Table 3.1 shows that the generated statistics for the full simulation sample of QCD di-jets in the range 70 GeV − 140 GeV is only 0.05 pb^{-1}, that is not enough to evaluate the impact of the QCD background on the $t\bar{t}$ analysis with 100 pb^{-1}. Even for the sample of QCD di-jets in the range 140 GeV − 280 GeV, that has a much lower cross section, the generated full simulation statistics is only of the order of one pb^{-1}. Therefore, a fast simulation production for this sample is also desirable.

Even if the small CPU consumption of the ATLFAST simulation makes possible a Monte Carlo production of the order of hundreds of pb^{-1}, the disk size of the output file is still not negligible. The size of the output file of the last stage of the fast simulation is about 10 KB per event. A production of 100 pb^{-1} of QCD di-jets in the p_T range of 70 GeV − 140 GeV is equivalent to generate about 600 millions of events, and therefore to store $\sim$ 6 Tera Bytes of data, that exceeds the computer resources for a local production at IFAE. To reduce the amount of data

stored in the disks, a filter was applied: any event with a reconstructed value of $\not\!\!E_T$ lower than 20 GeV or with less than 2 b-jets identified with a loose b-tagging selection (weight > 3, see Section 3.3.6) is rejected and therefore will not be recorded. The filter has a rejection factor of the order of 10^3 for the QCD di-jets sample with jets in the p_T range 70 GeV $-$ 140 GeV and 10^2 for those in the range 140 GeV $-$ 280 GeV (see Table 3.1).

Any event selection considered in this analysis includes tighter cuts than the cuts applied in the filter, so that any event that is needed for the analysis is kept after the filter is applied.

3.4.1 ATLFAST Performance

ATLFAST simulation is a fast parametrization of the detector response extracted from the full simulation with no detailed simulation of interactions of particles crossing the detector. It does not make use of the reconstruction algorithms of the full simulation (that will be applied to data) to identify all the particles that come out from the collision and from other interactions with the material of the detector. Hence, differences in terms of performance between the fast and full simulations are always expected.

In order to be able to use the results obtained from ATLFAST, its performance has to be evaluated and the impact of the differences into the analysis have to be understood and corrected if needed.

The following sections present the performance of the main components of the analysis and the corrections that were applied when the results differed from the full simulation in such a way that the numbers obtained in both simulations were not compatible.

Missing Transverse Energy

The $\not\!\!E_T$ reconstructed by ATLFAST is very optimistic compared with the full simulation in those events where the main source of the $\not\!\!E_T$ is the fake $\not\!\!E_T$ from detector effects and not a true source of $\not\!\!E_T$, like for example in QCD di-jets events. On the contrary, on events with large $\not\!\!E_T$ coming from true neutrinos, like in $t\bar{t}$ events, the $\not\!\!E_T$ estimation agrees very well between fast and full simulations. Figure 3.18 shows the $\not\!\!E_T$ comparison for $t\bar{t}$ events, with large component of true $\not\!\!E_T$, and QCD di-jet events, where the main source of $\not\!\!E_T$ comes from detector effects.

The fact that the $\not\!\!E_T$ distribution for full simulation in QCD samples has larger tails at high values compared to the ATLFAST simulation implies that any cut on $\not\!\!E_T$ must be decreased when applying it to ATLFAST samples in order to get a comparable efficiency to full simulation. The cut $\not\!\!E_T > 35$ GeV (used in this analysis) has an efficiency of 98.8% on the full simulation distribution of the right plot (QCD di-jets in the p_T range $70-140$ GeV) in Figure 3.18. In order to get the same efficiency for the ATLFAST distribution the cut must be relaxed to $\not\!\!E_T > 27$ GeV.

Figure 3.19 shows the Reconstructed - Truth resolution of $\not\!\!E_T$ and the ϕ component of the missing energy for ATLFAST and full simulation. In both distributions, ATLFAST $\not\!\!E_T$ presents a width about 25% smaller than in full simulation.

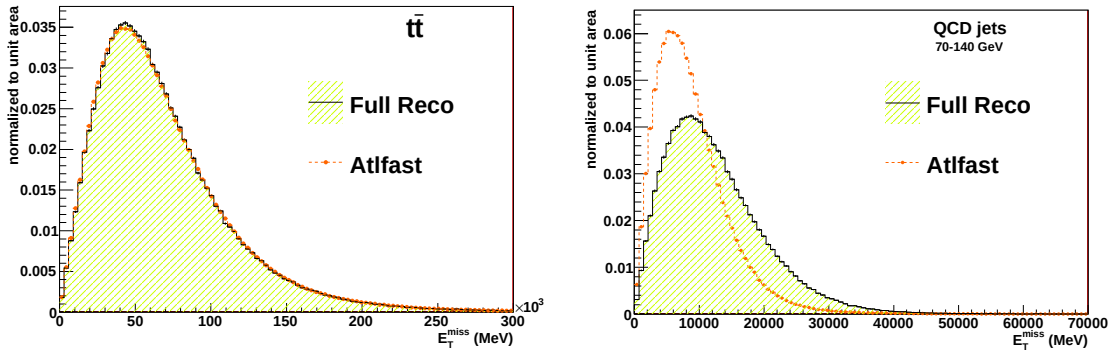

Figure 3.18: Comparison of ATLFAST and full simulation: the missing transverse energy distribution is shown for $t\bar{t}$ and QCD di-jets samples. Distributions are normalized to unit area.

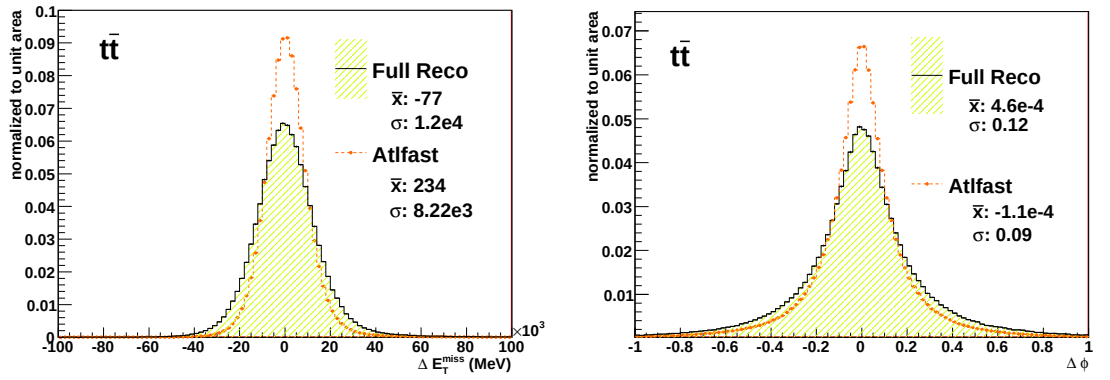

Figure 3.19: $\not\!\!E_T$ resolution for full and fast simulation. The left plot shows the Reco - Truth $\not\!\!E_T$. Right plot shows the ϕ component of Reco - Truth $\not\!\!E_T$. Distributions are normalized to unit area.

τ Jet

As the analysis is focused on the τ channel of the $t\bar{t}$ process, a good agreement in the τ performance between Full Simulation and ATLFAST is needed in order to validate the results obtained with ATLFAST on large statistics. As it can be seen in Figure 3.20, the rejection factor of the τ identification algorithm in ATLFAST is too high compared to the results obtained with the full simulation using a cut on the likelihood greater than 4 (that is the selection used for the analysis on full simulation -Section 3.3.4-). In order to decrease the rejection factor up to the level obtained with the full simulation, fake τ's were introduced in the event from truth jets (Section 3.3.1), according to a parametrization obtained from full simulation samples. As the τ performance depends on the topology of the event (events with higher occupancy of particles show higher τ fake rate), different parametrizations were obtained for $t\bar{t}$ and different ranges in p_T of QCD di-jets events. True jets that are introduced in the reconstruction as fake τ's are smeared on its energy according to the τ energy resolution.

The result of the corrections applied to obtain the right τ efficiencies and fake rates is shown on Figures 3.21 and 3.22 for $t\bar{t}$ events.

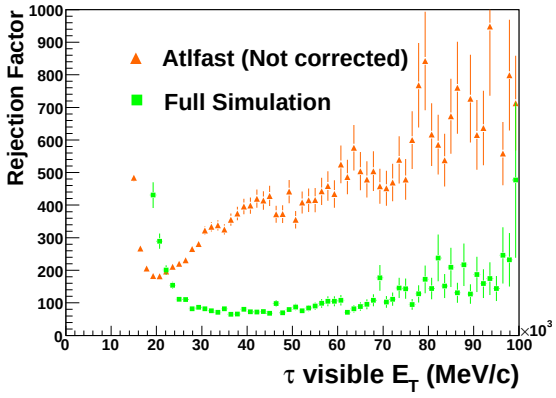

Figure 3.20: Tau rejection factor on $t\bar{t}$ events (before any correction to ATLFAST is applied), normalized to cone 0.4 truth jets, for ATLFAST (triangles) and full simulation (squares) as a function of p_T.

b-jet tagging

The b-tagging is also an important component in the analysis, needed to reduce the background, in particular QCD, to reasonable levels. In full simulation, the b-tagging efficiency and rejection factors are a function of the selection cut on the b-tagging likelihood (Section 3.3.6). The simplest method to reproduce the efficiency provided by the full simulation at a given likelihood cut is to tag jets randomly at a constant rate. While this works fairly well for b-jets, the efficiency for non b-jets to be mistagged depends highly on the kinematics of the jet and its flavour composition. A constant rate mistagging would bias the kinematics of mistagged events

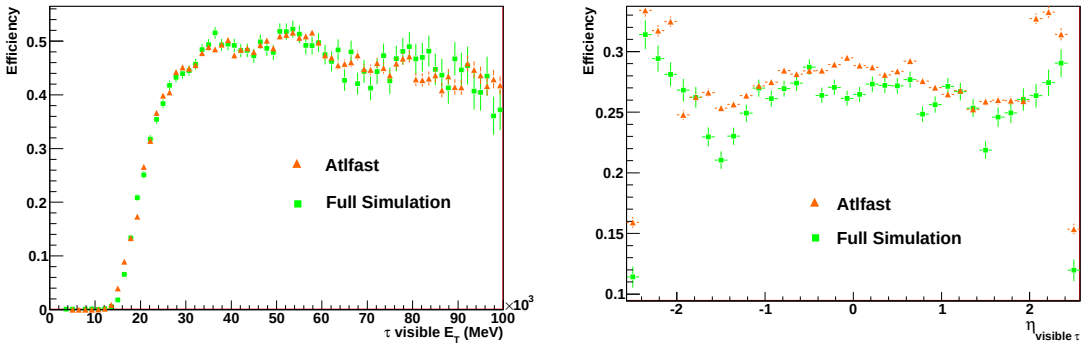

Figure 3.21: Tau identification efficiency on $t\bar{t}$ events for corrected ATLFAST (triangles) and full simulation (squares) as a function of p_T (left) and η (right) of the visible products of the τ.

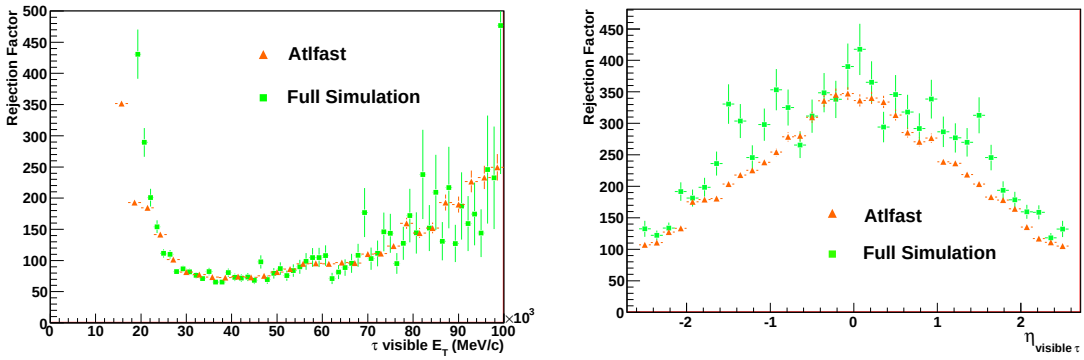

Figure 3.22: Tau rejection factor on $t\bar{t}$ events, normalized to cone 0.4 truth jets, for corrected ATLFAST (triangles) and full simulation (squares) as a function of p_T (left) and η (right) of the visible products of the τ.

significantly. Therefore corrections to ATLFAST b-tagging [74] were carried out first labelling jets according to their procedence:

- b-jet: a jet within $\Delta R < 0.3$ from a truth b quark.
- c-jet: a jet within $\Delta R < 0.3$ from a truth c quark.
- τ-jet: a jet within $\Delta R < 0.3$ from a truth τ lepton.
- light jet: a jet that is not one of the above.
- pure light jet: a jet that is away from b/c quark or τ lepton by $\Delta R > 0.8$.

An efficiency parametrization from full simulation is extracted for each category of jets and applied to ATLFAST labelled jets. Rejection of light jets depends on event topology since it is more likely to have tracks from heavy quark decays in light jets in events with high particle population. The definition of pure light jet removes such dependency.

A comparison of the full simulation and ATLFAST corrected for b-tagging is shown in Figures 3.23 and 3.24.

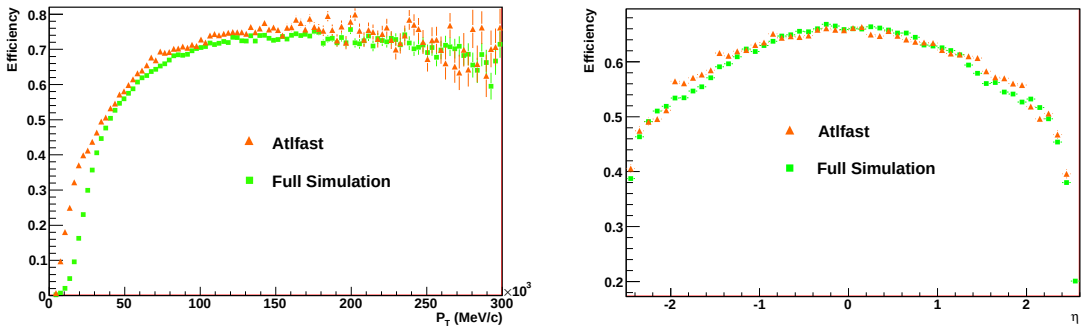

Figure 3.23: b-tagging efficiency on $t\bar{t}$ events for ATLFAST (triangles) and full simulation (squares) as a function of p_T (left) and η (right) of the b-jet.

Particle Jets

Reconstruction of particle jets is important in top physics where the jet multiplicity is very high and can be used to reject other background processes with lower jet multiplicity like QCD events. Therefore, a good agreement between ATLFAST and full simulation in the jet multiplicity of signal and background events is desirable. Also, jet properties like energy resolution and angular resolution need to be validated for ATLFAST, as other, more elaborated, kinematical variables built for $t\bar{t}$ identification will make use of jets as basic components.

The event selection of this analysis specifically requires at least two light jets (non b-tagged) with $p_T > 20$ GeV. A good parametrization of the full simulation particle jets efficiency is needed to rely on ATLFAST results for high statistic samples.

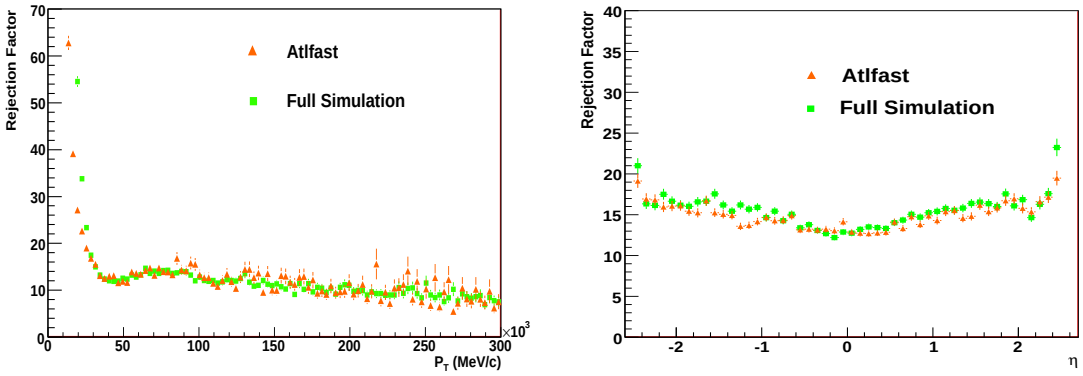

Figure 3.24: b-tagging rejection factor on $t\bar{t}$ events, normalized to cone 0.4 truth jets, for ATLFAST (triangles) and full simulation (squares) as a function of p_T for $\eta < 2.5$ (left) and η for $p_T > 20$ GeV (right) of the b-jet.

Figure 3.25 shows a comparison of the reconstruction efficiency of jets as a function of η and p_T. While performance differences appear large in the high η region and in the low p_T region, the effect on the overall difference is small due to the kinematical cuts used in the analysis as can be concluded from Table 3.3. The lower efficiency of fully simulated jets can partially be attributed to detector effects such as noise, although much of the inefficiency in high η region is due to the use of calo towers where they are less representative of the topology of the energy deposited from hadrons. The use of topo clusters (algorithm already implemented within the ATLAS software) can provide a vast improvement.

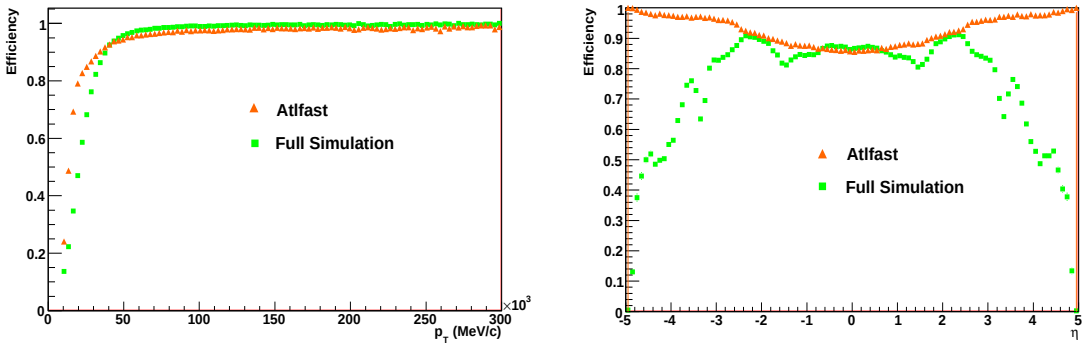

Figure 3.25: Reconstruction efficiency of particle jets on $t\bar{t}$ events for ATLFAST (triangles) and full simulation (squares) as a function of p_T (left) and η (right). In the right plot jets have a p_T cut at 20 GeV.

Figure 3.26 shows the resolution of jets for full simulation and fast simulation. The shift in central value of p_T resolution is noticeable: ATLFAST understimates it by 0.2% and full simulation by 2.9%. On the contrary, the agreement in angular resolution is quite satisfactory.

This difference in the p_T resolution between ATLFAST and full simulation is also seen in the

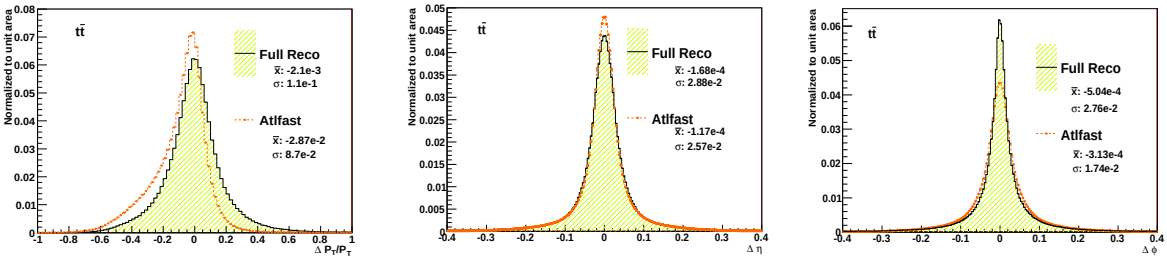

Figure 3.26: Comparison of ATLFAST and full simulation p_T, η and ϕ resolution of particle jets.

p_T spectrum of jets (Figure 3.27 for $t\bar{t}$ events), although the differences are much less important above the 20 GeV p_T cut used in this analysis. Particularly important is the jet multiplicity distribution, shown in Figure 3.28 for $t\bar{t}$ and QCD jets, as the analysis will require a minimum number of jets reconstructed per event.

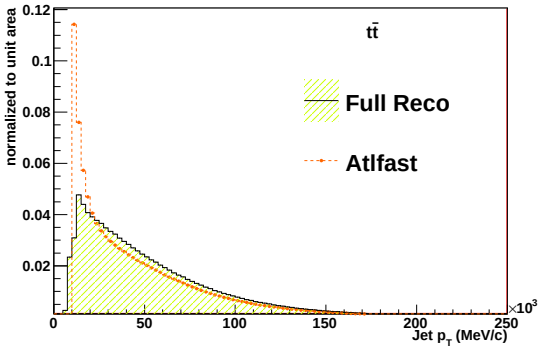

Figure 3.27: p_T spectrum of particle jets on $t\bar{t}$ events for ATLFAST (triangles) and full simulation (squares).

Although the agreement is not perfect for all the jet properties between ATLFAST and full simulation, its impact on the analysis is still at reasonable levels, as can be inferred from the numbers shown in Tables 3.3 and 3.4, which compare the number of events that pass each selection cut used in the analysis between ATLFAST and full simulation. A comparison of other kinematical variables (related to the topology of the $t\bar{t}$ events) used in the analysis will be presented in Section 4.5, after the reconstruction of the $t\bar{t}$ has been explained.

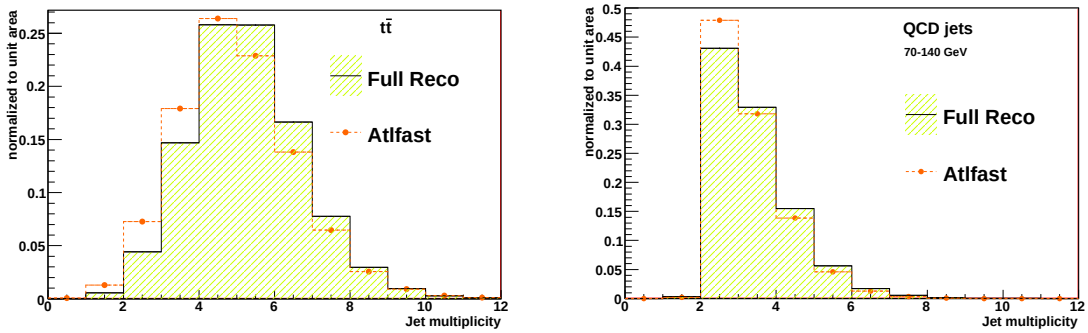

Figure 3.28: Jet multiplicity in $t\bar{t}$ events for ATLFAST (triangles) and full simulation (squares). Only jets with p_T above 20 GeV are considered.

Table 3.3: Comparison in number of events between ATLFAST and full simulation for $t\bar{t}$ event selection cuts. Cuts applied (shown in the first column) are cumulative. The table shows the number of events after each selection cut for full simulation and ATLFAST and the efficiency relative to the previous cut.

$t\bar{t}$	**Full sim**	**Eff**	ATLFAST	**Eff**
Total number	584550 ± 800	-	4835000 ± 2000	-
$\not\!\!E_T > 35$ GeV	454670 ± 700	77.78 ± 0.15	3739000 ± 2000	77.34 ± 0.05
# of Light Jets > 1	387600 ± 600	85.25 ± 0.19	3190500 ± 1800	85.32 ± 0.07
τ $p_T > 25$ GeV/c	28250 ± 170	7.29 ± 0.05	220200 ± 500	6.9 ± 0.015
# B Jets > 1	9050 ± 100	32.0 ± 0.4	67600 ± 300	30.7 ± 0.13
e,μ veto	6330 ± 80	70.0 ± 1.1	51440 ± 230	76.1 ± 0.5

Table 3.4: Comparison in number of events between ATLFAST and full simulation for QCD. The table shows the number of events after each selection cut (the first cut on $\not\!\!E_T$ and b-tagging is always applied due to the filter applied at the generation level for QCD samples -Section 3.4-) for full simulation and ATLFAST and the efficiency relative to the first cut. Numbers for τ cut are omitted because this cut kills all the full simulation events.

QCD jets (35 – 70 GeV)	**Full sim**	**Eff**	ATLFAST	**Eff**
Total number	290300	-	583132	-
1) $\not\!\!E_T > 35$ GeV (27 GeV for ATLFAST) # B Jets > 1	219 ± 15	0.075 ± 0.005	433 ± 21	0.0074 ± 0.004
1) + # of Light Jets > 1	127 ± 11	58 ± 6	264 ± 16	61 ± 5
1) + τ $p_T > 25$ GeV/c	-	-	-	-
1) + e,μ veto	181 ± 13	83 ± 8	372 ± 19	86 ± 6

Chapter 4

$t\bar{t}$ with Decay to τ Analysis

In a $t\bar{t}$ event, once produced, each top quark will decay quickly due to its very large mass. Top quarks, in the SM, decay almost exclusively to a b quark and a real W boson with a branching ratio ~ 0.999.

The W boson subsequently can decay leptonically ($W \rightarrow l\nu_l$, where l is e, μ or τ with a branching ratio of 32%) or hadronically ($W \rightarrow q_1\bar{q}_2$, where (q_1, q_2) are (u, d) or (c, s) with a branching ratio of 68%). Figure 4.2 shows the branching ratios of each decay mode. The analysis presented here considers the case where one of the W bosons decays to a hadronically decaying τ and the other one decays hadronically yielding a couple of jets in the calorimeter (see the Feynman diagram in Figure 4.1). Therefore a typical event of this analysis will contain two b-jets, two light jets, one hadronically decaying τ and $\not\!\!E_T$.

It is also easier to reconstruct than the dilepton channel, for in this last case there are two sources of missing energy that make difficult to reconstruct the transverse masses of the two corresponding W bosons.

Due to the large jet multiplicity that characterizes the $t\bar{t}$ events (see Figure 4.3), it will be very important to efficiently identify the real τ's of the event and to provide high jet rejection to reduce the combinatorial background (real $t\bar{t}$ events that were identified and passed the event selection cuts, but where the τ is a fake) to the minimum and to control the physics background. Being the τ's produced at the very end of the decay chain in a $t\bar{t}$ event, their p_T spectrum is very soft (see Figure 4.4). As the tau identification algorithms are only efficient for τ's with visible transverse energy above 25 GeV (see Section 3.3.4 where the performance of the tau identification algorithm is presented), around 60% of the events, containing a very soft tau, will not pass the event selection.

Two algorithms for τ reconstruction and identification are available as part of the ATLAS reconstruction software: a calorimeter-based and a tracking-based. For the same efficiency on signal of 50%, the calorimeter-based algorithm provides a higher jet rejection, that justifies its use in this analysis (Section 3.3.4).

Another important piece of the analysis is the missing transverse energy. In the *semileptonic mode* with τ's in the final state, $t\bar{t}$ events present several sources of real missing transverse

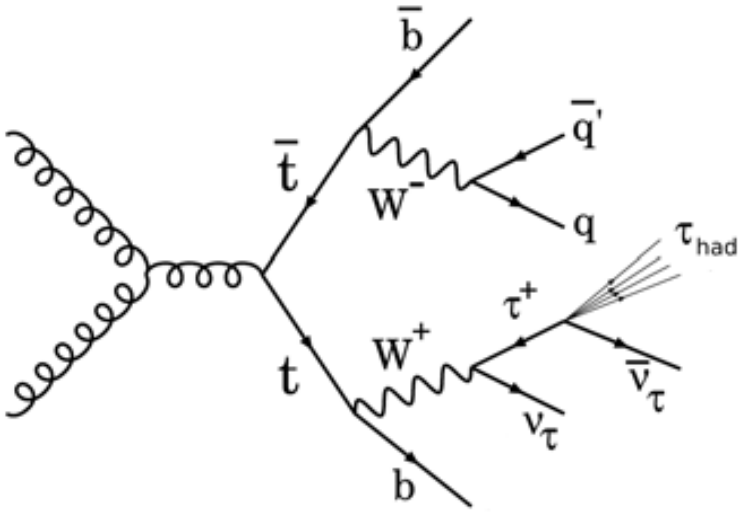

Figure 4.1: Feynman diagram for $t\bar{t}$ semileptonic with a hadronically decaying τ in the final state. The bunch of particles labeled as τ_{had} represents the visible products of the τ that decays hadronically.

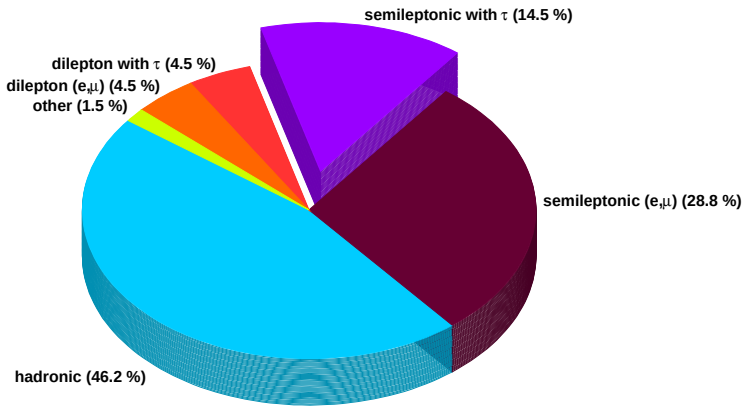

Figure 4.2: Branching ratios of the different decay modes of a $t\bar{t}$ event. For almost every event, each top will decay to a b quark and a real W boson. In the *hadronic mode*, both W bosons decay hadronically to (u, d) or (c, s). In the *semileptonic mode* one of the W bosons decays leptonically while the other one decays hadronically, and finally, in the *dilepton mode*, both W bosons decay leptonically.

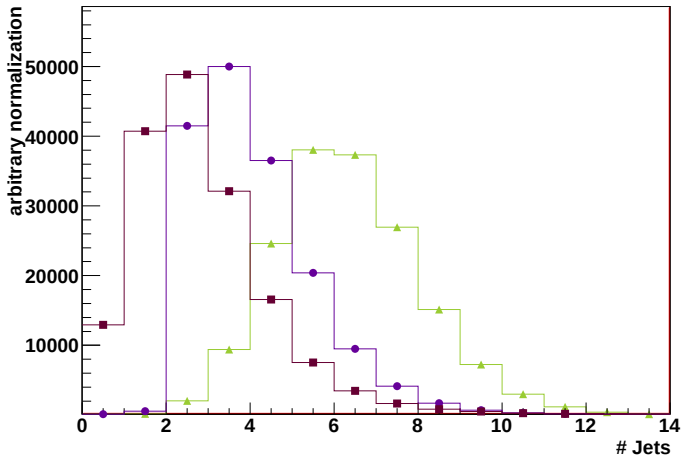

Figure 4.3: Number of reconstructed jets with the Cone 0.4 algorithm for $t\bar{t}$ (green triangles), $Z \rightarrow \tau\tau$ (red squares) and QCD jets (purple circles)

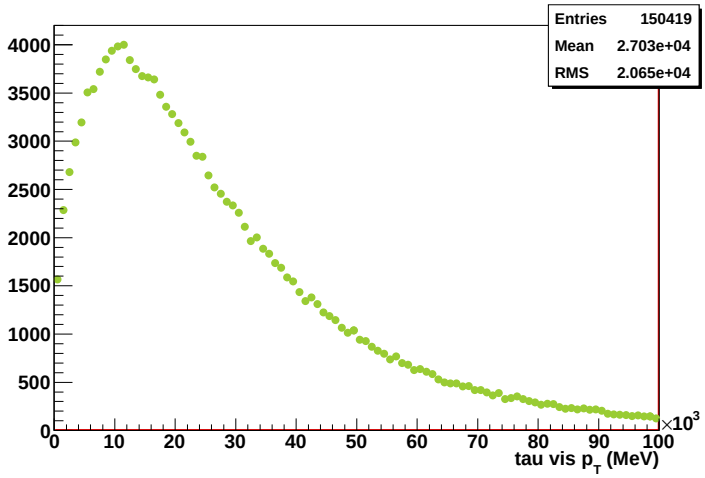

Figure 4.4: Visible tau p_T spectrum for τ's from a $t\bar{t}$ decay.

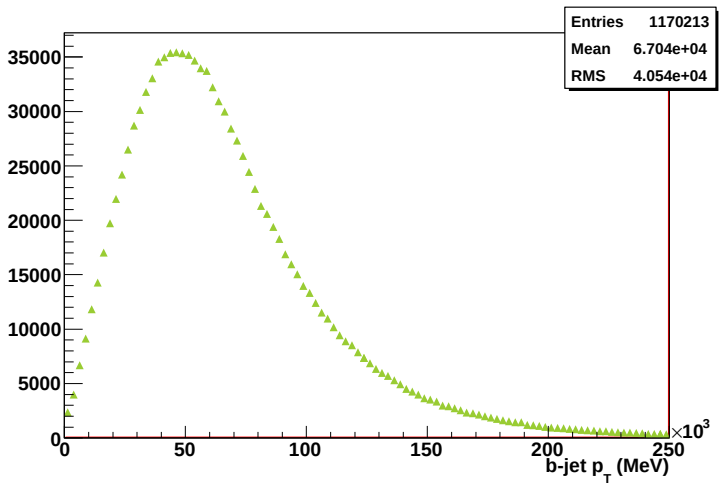

Figure 4.5: p_T spectrum of b-quarks from a $t\bar{t}$ decay.

energy. First, the W boson that decays leptonically ($W \rightarrow \nu l$) already produces large values of missing transverse energy due to the presence of the neutrino. A second source of real missing transverse energy is the neutrino from the τ that decays hadronically.

Finally, the last important piece of the analysis is the b-tagging (see Section 3.3.6 for a description of performance results). Each of the tops will produce one b quark in the decay so that a $t\bar{t}$ event will contain at least two b quarks with a relatively high p_T spectra (see Figure 4.5), that will be reconstructed as jets in the calorimeter and can be tagged as b-jets. To require at least two b-jets in the reconstructed event will reduce drastically the QCD background and will help in reducing the W+jets and single top backgrounds.

4.1 Preselection

In the preselection step every particle is identified in order to be able to build later the $t\bar{t}$ event.

Electrons and muons are identified with the criteria presented in Sections 3.3.2 and 3.3.3. Both leptons should pass a p_T threshold of 15 GeV.

Taus are identified applying a likelihood cut greater than 4 (as explained in Section 3.3.4). Overlaps between different particles are treated in such a way that identified particles of different types are not associated to the same objects in the calorimeter.

If a jet/τ overlaps with a previously identified electron, i.e. the center of the jet/τ is closer to the electron than 0.3 in ΔR, the jet is removed. A similar procedure is applied to τ's and jets, however as only one τ is expected (in the signal) per event and the τ fake rate being non negligible in high jet multiplicity environments like $t\bar{t}$, to avoid removing these jets that match a fake τ, only the jets that overlap with the τ selected to build the leptonic W boson will be removed from the event.

Jets reconstructed using the cone 0.4 algorithm should pass a p_T threshold of 20 GeV in order

to minimize biases related to jet calibration, minimum bias and noise level at low transverse energy.

Finally, b-jets are tagged using two selections for different scenarios. As the b-tagging requires a very good understanding of the algorithms that compute the secondary vertex, impact parameter and other variables relevant to disentangle heavy quarks from light quarks with real data, as well as a calibration and likelihood training for signal and background, it may happen that at the very beginning (with 100 pb^{-1} of integrated luminosity) the light jet rejection of the b-tagging algorithm is far from being at the expected values extracted from the Monte Carlo simulation.

For an integrated luminosity of 100 pb^{-1}, a loose b-tagging uses the cut weight greater than 3 (Section 3.3.6) while for 1 fb^{-1}, a tighter b-tagging uses the cut weight greater than 7.05. Jets identified as b-jets are not considered as light jets.

4.2 $t\bar{t}$ Event Reconstruction

A first step in the event selection is to require the reconstructed objects corresponding to all particles and components needed to reconstruct and identify a $t\bar{t}$ event. This includes light jets reconstructed in the calorimeter, at least one τ, at least 2 b-tagged jets and missing transverse energy.

Later, all the components can be combined in order to build the invariant masses of the composite particles, mothers of the particles seen in the detector, like the W bosons and the top quark. As the analysis studies the semileptonic decay mode of $t\bar{t}$ events, the event can be separated in two pieces: a "hadronic side", composed by the W boson that decays into a pair of light quarks ((u, d) or (c, s)) and the b quark that accompanies the W boson from the top decay. And a "leptonic side" composed by the τ and the missing transverse energy produced in the decay of the second W boson, as well as the b-jet produced from the b-quark that decays from the initial top.

While on the leptonic side the reconstruction simply consists in a combination of the selected τ and the missing transverse energy, in the hadronic side there are many possible combinations to build a hadronic W boson and the hadronic top from the basic ingredients. In this analysis, four different strategies were studied. Three of them build first a hadronic W from a pair of light jets and later use it in combination with a b-jet to calculate the hadronic top. On the contrary, the fourth strategy computes first the best combination to form a hadronic top and later obtains the best hadronic W combination.

Leptonic Side Reconstruction

On the leptonic side the identified tau (with transverse momentum larger than 25 GeV) is combined with the transverse missing energy to build the leptonic W transverse mass. As shown schematically in Figure 4.1, in the decay chain of the leptonic top ($t \to bW^+ [\to \tau^+(\tau_{had}\bar{\nu}_\tau)\nu_\tau]$) there are two different sources of missing transverse energy: the neutrino that decays from the W boson and the neutrino that appears in the hadronic decay of the τ. Both will contribute

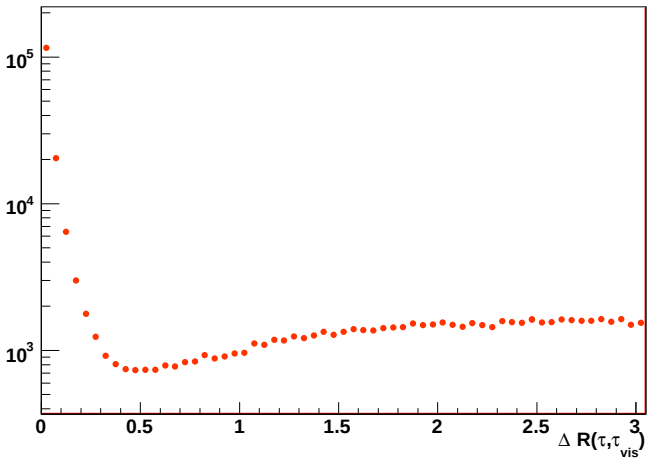

Figure 4.6: ΔR between the τ that decays from the W boson and the composite particle formed by its visible decay products in $t\bar{t}$ events. 65% of the τ's are closer than 0.2 in ΔR to its visible decay products.

to the total missing transverse energy, and therefore it is not possible to reconstruct exclusively the energy and momentum of the two neutrinos separately.

Assuming the collinear approximation for the τ decay (the visible products of the decay of the τ and the associated neutrinos of its decay are collinear), the invariant transverse mass of the leptonic W boson can be determined with the following expression

$$M_T^{lepW} = \sqrt{2E_T^{\nu_\tau}\left(E_T^{\tau_{had}} + E_T^{\bar{\nu}_\tau}\right) \cdot \left[1 - cos\theta\left(p_T^{\tau_{had}}, \nu_\tau\right)\right]} \tag{4.1}$$

where τ_{had} are the visible decay products of the hadronic decay of the τ. The use of the collinear approximation is justified by Figure 4.6.

As it is not possible to extract separately the transverse momentum of each neutrino, ν_τ and $\bar{\nu}_\tau$, from the reconstructed missing transverse energy, we can only approximate the leptonic W transverse mass by the following expression

$$M_T^{lepW} = \sqrt{2\not{E}_T E_T^{\tau_{had}} \cdot \left[1 - cos\theta\left(p_T^{\tau_{had}}, \not{p}_T\right)\right]} \tag{4.2}$$

The formed leptonic W is then combined with the closest (in ΔR) b-jet to constitute the leptonic top. If there is more than one reconstructed tau we select the the most energetic one.

Hadronic Side Reconstruction

The hadronic side is built from a combination of light jets and b-tagged jets. In the following, the four different strategies to build the hadronic side of the $t\bar{t}$ event are summarized.

- Best PDG - Closest ΔR

  Among all possible pairs of light jets, this strategy selects the jet pair with invariant mass

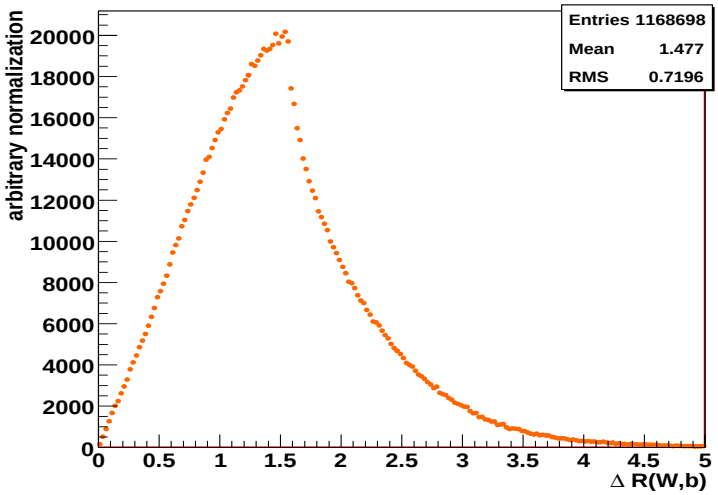

Figure 4.7: Distance in ΔR between the hadronic W boson and the b quark that decays from the top in $t\bar{t}$ events.

closer to the W mass PDG value. The hadronic top is built by combining this hadronic W with the closest b-jet in ΔR. This strategy will bias the hadronic W mass distribution, so that the variable can not be included in the list of variables that participate in the event selection, but may reduce the fakes in the reconstruction of the hadronic top on the signal.

Figure 4.7 shows the distance in ΔR between the hadronic W boson and the b quark that decays from the same top quark.

- Highest Jets - Highest b-Jet

  From the set of all possible light jets, this strategy selects the two most energetic ones to form a hadronic W. Later this hadronic W is combined with the b-jet with highest p_T to build the hadronic top. Figure 4.8 compares the p_T distribution of the leading jet of the event and the highest p_T jet that decays from the W boson.

- Highest composite particle

  From the set of all possible light jets, this strategy builds a candidate W boson. Among all the W candidates, it selects the one with the highest p_T. The same procedure is carried out to combine the W boson with a b-jet to form a top candidate and select the most energetic one.

- Highest composite (build hadronic top first)

  This strategy builds a hadronic top candidate from any possible combination of a pair of light jets and a b-jet. Among all the top candidate it selects the one with highest p_T. The pair of light jets that was chosen to be part of the hadronic top will form the hadronic W boson.

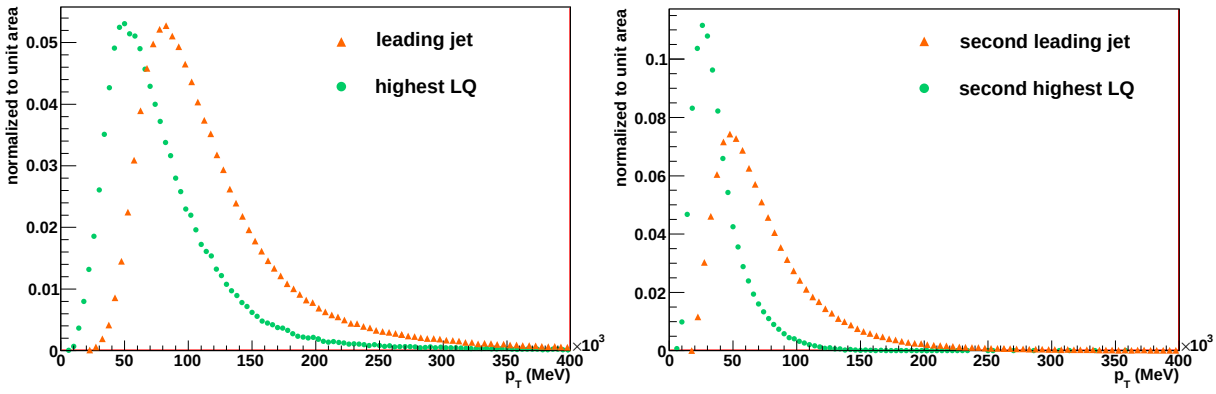

Figure 4.8: Comparison of the spectrum of the leading jets of a $t\bar{t}$ event and the light quarks that decay from the W boson. On the left: p_T distribution of the leading jet (red triangles) and the most energetic of the two light quarks (green circles) that decay from the W boson. On the right: p_T distribution of the second leading jet (red triangles) and the less energetic of the two light quarks (green circles) that decay from the W boson.

All strategies yield similar results in terms of the ratio of signal and background events (S/B) (see appendix A), but the shape of the resulting invariant masses for the W boson and top quark shows some differences. The different behaviour in shapes among the various strategies can be clearly seen in Figures 4.17 and 4.18, where the amount of background was artificially increased to better visualize the shape of the background distributions, which are well fitted to a fourth order Chebyshev polynomial, and compare them with the $t\bar{t}$ signal, that fits nicely to a Gaussian distribution. In general, the distributions for the background are shifted with respect to the signal, where the value and sign of the shift depend on the strategy chosen. As explained in more detail in Section 4.8, although the properties of the distributions of invariant masses vary with the strategy to be considered, the information that can be extracted from them is equivalent, with one exception: the *Best PDG - Closest* ΔR strategy biases the background distributions, which follow exactly the same shape as the $t\bar{t}$ signal. In this case, there is a loss of information that is crucial to determine the amount of background present in data, and therefore, to measure the $t\bar{t}$ cross secion. Unless explicitly mentioned, the default strategy considered in the document from now on is the *Highest Jets - Highest b-Jet*.

4.3 Hadronic τ Purity

Due to the fact that the tau fake rate is very large compared with other particle misidentifications, and also to the fact that the jet multiplicity of a $t\bar{t}$ event is large, the purity (fraction of events that contain a true hadronically decaying τ among all the selected events) of the selected data sample is far from being 100 %. While muons are rarely misidentified as taus, there will be contamination from true electrons that are identified as taus because the electron veto was

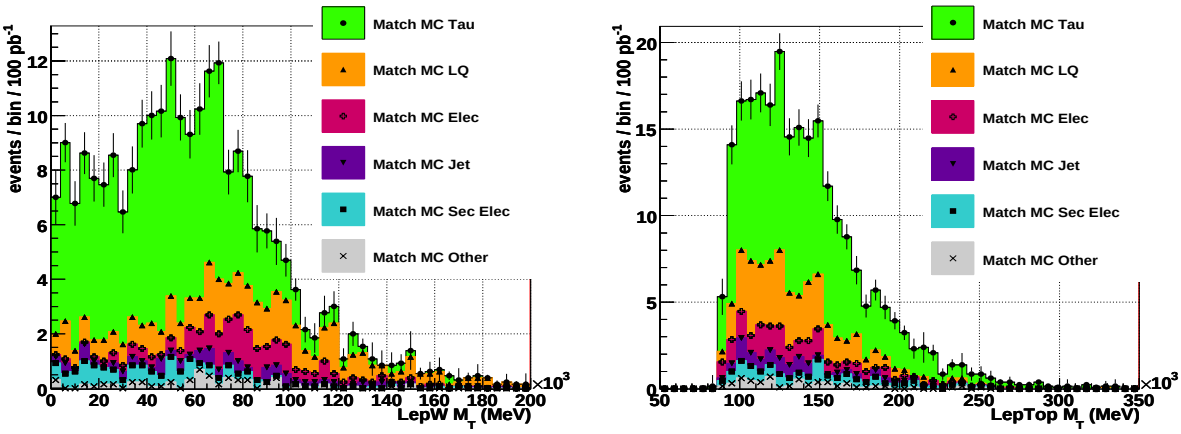

Figure 4.9: Distribution of the leptonic W (left) and top (right) transverse masses, normalized to an integrated luminosity of 100 pb^{-1}, computed as a combination of a reconstructed hadronic τ and missing transverse energy from Eq. 4.2. Each reconstructed τ was matched to a MC object to investigate its origing. Cumulative distributions show reconstructed τ's matched to true hadronic decaying τ's (green solid circles), true light quarks that decay from the hadronic W (orange upward solid triangles), true electrons that decay from a leptonic W (red crosses), any truth jet -jets built with the same reconstruction algorithm but using true particles- (blue downward solid triangles), true secondary electrons -those that do not decay from the W boson- (cyan open circles) and any other true object (gray crosses).

not efficient enough, and of course, significant contamination of different types of jets into the τ sample.

Figure 4.9 shows the different sources of contamination to the τ sample, after applying the event selection for the 100 pb^{-1} scenario, with the loose b-tagging selection. The main contributions come from the light quarks that decay from the hadronic W boson, due to the very low jet rejection factor of the τ identification on those kind of jets (Figure 3.10), and the electrons that come from the decay of a W boson in $t\bar{t} \rightarrow W(\rightarrow e\nu_e)b\, W(\rightarrow jetjet)b$ events.

The purity of the τ sample in this scenario is 60%. For the 1 fb^{-1} scenario, using a tighter b-tagging selection, the tau purity remains unchanged, as the b-quarks do not contribute significantly to the contamination of the τ sample. Figure 4.10 shows the same sources of contamination to the τ sample for the tight b-tagging scenario.

4.4 Event Selection

Once the preselection is applied and the $t\bar{t}$ event is reconstructed, the following selection cuts are applied in order to maximize the observation of the $t\bar{t}$ signal respect to the background:

- Transverse missing energy, $\not\!\!E_T$, should be larger than 35 GeV.
- At least 2 light jets (with $p_T > 20$ GeV).

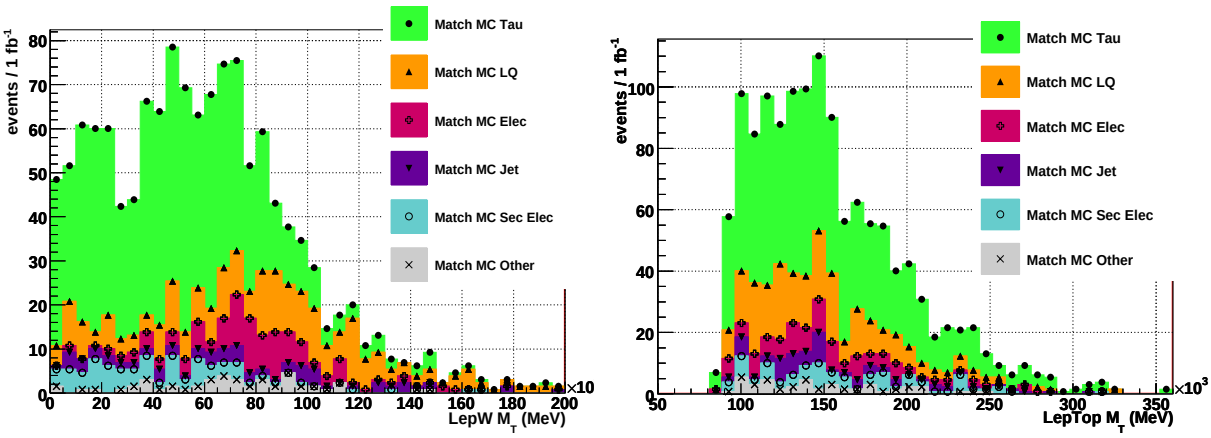

Figure 4.10: Same as Figure 4.9 but using the tight b-tagging selection. Distributions are normalized to an integrated luminosity of 1 fb^{-1}.

- An identified τ with $p_T > 25$ GeV.
- At least 2 b-jets (with $p_T > 20$ GeV).
- No identified lepton (electron or muon with transverse momentum larger than 20 GeV) should be present in the event.
- The angular distance between the two selected b-jets, $\Delta R(\mathrm{b}, \bar{\mathrm{b}})$, should be larger than 1.
- The azimuthal angle between the missing momentum and the b-jet on the hadronic side, $\Delta\phi(\not{p}_T, B)$, should be larger than 0.5
- The minimum of the azimuthal angle between the missing momentum and the 3 leading jets in the event should be larger than 0.8

The effect of the event selection on the signal and the background processes was evaluated using the corresponding Monte Carlo samples simulated with a full Geant4 simulation, except the QCD background, for which there was not enough statistics (due to its huge cross section) and the use of the fast simulation was needed. As explained in Section 3.4.1, the parametrization of the missing transverse energy is not realistic enough in the fast simulation (compared to the full simulation). Therefore in order to apply a realistic event selection to the fast simulation samples, the missing transverse energy cut, placed at 35 GeV for full simulation was relaxed to 27 GeV so that the efficiency of this cut on QCD samples is comparable between fast and full simulations.

For the rest of cuts in the event selection, all the relevant corrections were applied to the different objects in the fast simulation so that the fast parametrization agrees well with the full simulation in terms of identification efficiencies and background rejection. Therefore the same cuts for the event selection were used for the QCD fast simulation samples.

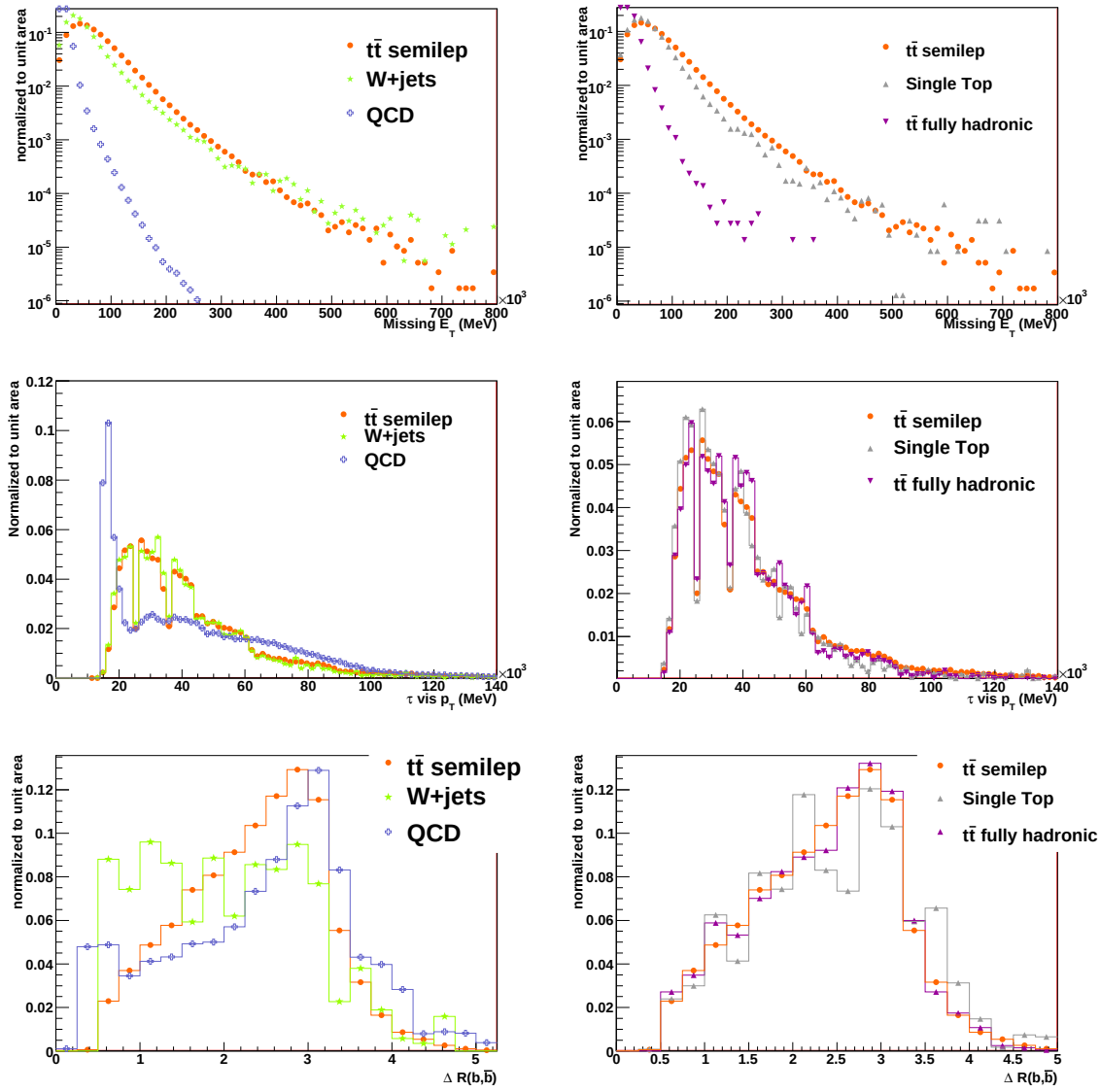

Figure 4.11: Variables included in the event selection. Distributions show the $t\bar{t}$ semileptonic signal as well as all relevant physics backgrounds. All variables are normalized to unit area to be able to compare the shapes of the distributions. Some variables, like the ΔR between the leptonic and the hadronic identified b-jets, have strong requirements on the preselection of the event, like having two identified b-jets, which reduce significantly the statistics of the background distributions.

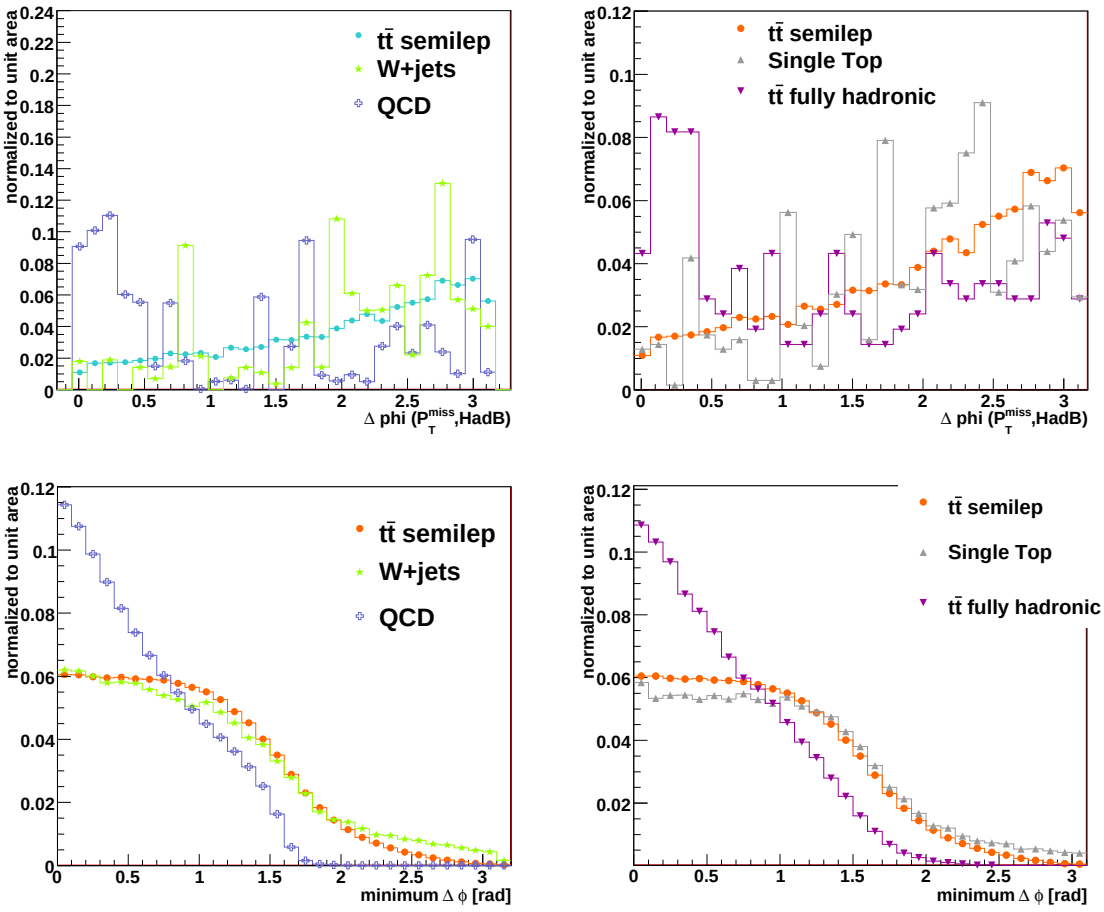

Figure 4.12: Variables included in the event selection. Distributions show the $t\bar{t}$ semileptonic signal as well as all relevant physics backgrounds. All variables are normalized to unit area to be able to compare the shapes of the distributions.

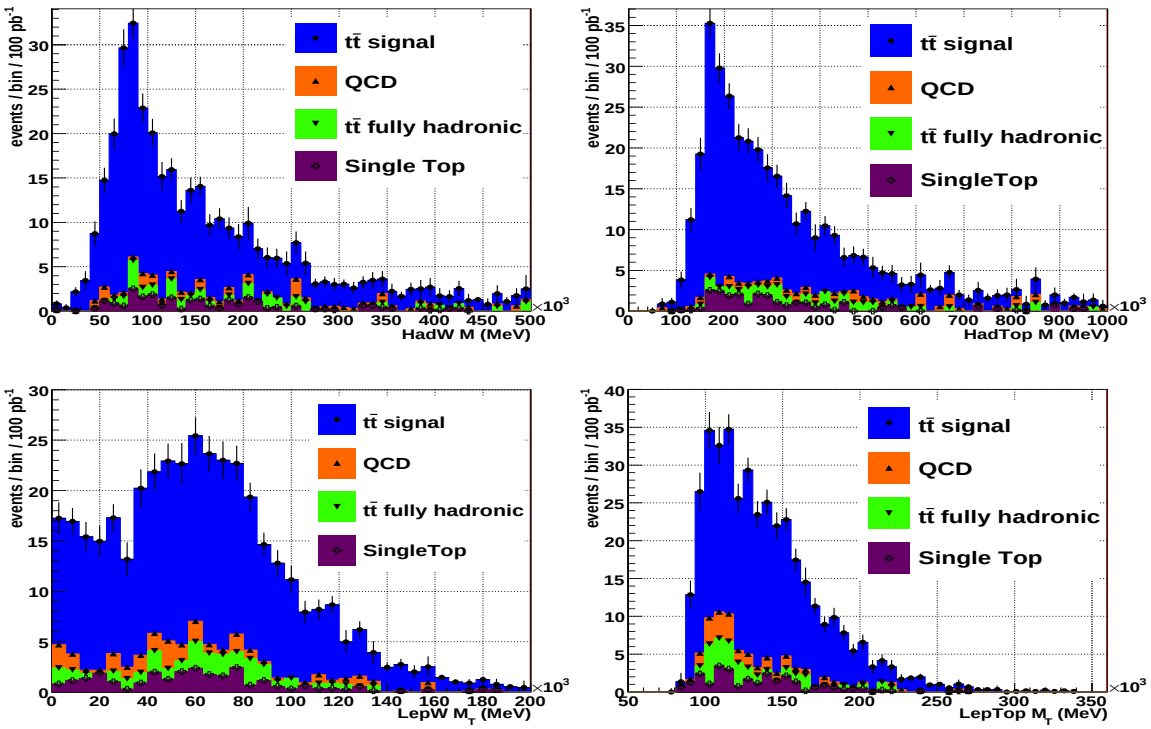

Figure 4.13: Invariant masses for hadronic W, hadronic top, leptonic W and leptonic top, reconstructed with the *Highest Jets - Highest b-Jet* strategy (see Section 4.2) after applying the full event selection. Plots are normalized to an integrated luminosity of 100 pb^{-1}. Distributions are shown in cumulative histograms for the different samples: single top (open crosses), $t\bar{t}$ fully hadronic (downward triangles), QCD (upward triangles) and $t\bar{t}$ signal (circles). The W+jets sample is not shown in the plots for it has a negligible contribution to the total number of events. Errors shown for the sum of all the contributions are computed from the full statistics available in the simulation (Table 3.1).

Some of the variables used in the event selection are shown in Figures 4.11 and 4.12.

Figure 4.13 shows the reconstructed invariant masses for the hadronic W boson and top and the transverse masses for the leptonic W boson and top after the event selection for signal and SM background. Although a first look at the shapes seems to indicate that they are not useful to disentangle between signal and background, Section 4.8 will explain a method developed to evaluate the amount of background present in data using the hadronic invariant mass distributions.

In the analysis, two possible scenarios have been considered. The first scenario is prepared for an analysis with early data for an integrated luminosity of 100 pb^{-1}. In this early stage of the experiment we can not expect an optimum performance of the reconstruction and identification algorithms. In particular the b-tagging will require a good understanding of the detector, specially the Inner Detector, and its performance might be far from the optimum at the very beginning (see Section 4.1). The time needed to collect 100 pb^{-1} of data at low luminosity, $10^{32}cm^{-2}$ s^{-1}, is about one month. Expected number of events for signal and backgrounds for this early data scenario are quoted in Table 4.2.

Due to τ fakes and lepton identification inefficiencies there is contamination on the τ sample from the different semileptonic and dilepton channels on $t\bar{t}$ events after applying the event selection. Table 4.1 shows the composition of each type of event.

Table 4.1: Sample composition after applying the event selection to $t\bar{t}$ semileptonic events.

Event Type	**Sample Composition (%)**
Semileptonic	
$t\bar{t}$ (elec)	14.1
$t\bar{t}$ (muon)	3.1
$t\bar{t}$ (tau)	71.4
Dilepton	
$t\bar{t}$ (di-tau)	5.1
$t\bar{t}$ (muon-tau)	1
$t\bar{t}$ (elec-tau)	4
$t\bar{t}$ (di-elec)	0.5

The second scenario is adapted to a more advanced stage of the data taking. The reference here is an integrated luminosity of 1 fb^{-1}, that can be achieved in about one month running at an instantaneus luminosity of 10^{33} or in one year at 10^{32}. In this scenario, the number of signal events using the previous selection is an order of magnitude larger than the one shown in Table 4.2. In order to increase the total S/B, this scenario considers a tighter event selection, in particular in what concerns the b-tagging identification criterium that is one of the most efficient cuts to reduce the QCD background[1)]. The cut in the likelihood for the b-tagging identification

[1)] Tighter cuts can be applied also to other basic selections, like the tau identification likelihood or the missing transverse energy threshold. However the lack of simulated events for the background, specially QCD, prevents us from doing a detailed study.

Table 4.2: Number of events remaining after each selection requirement, for signal and Standard Model background samples, using a loose b-tagging selection for 100 pb^{-1}. The rightmost column shows the signal over background ratio. QCD simulation includes a filter requiring at least 2 identified jets and $\not\!\!E_T > 20$ GeV to increase the generation efficiency. Therefore, no expected number of events for the first cuts are shown in the table. Errors quoted in this table correspond to the available MC statistics for each given sample (see Table 3.1). Numbers in parentheses are the S/B ratio for the each background.

	N_{evt} (100 pb^{-1})		
	Non hadronic $t\bar{t}$	**Hadronic $t\bar{t}$**	**Single top**
no cut	4.500e+4 ± 6e+1	3.852e+4 ± 1.4e+2 [1.2]	1.122e+4 ± 5e+1 [4.0]
$\not\!\!E_T > 35$ GeV	3.500e+4 ± 5e+1	4.86e+3 ± 5e+1 [7.2]	8.13e+3 ± 5e+1 [4.3]
# of Light Jets > 1	2.984e+4 ± 5e+1	4.79e+3 ± 5e+1 [6.2]	6.11e+3 ± 4e+1 [4.9]
τ $p_T > 25$ GeV/c	2175 ± 13	232 ± 12 [9.4]	324 ± 9 [6.7]
# B Jets > 0	1751 ± 12	209 ± 11 [8.4]	199 ± 7 [8.8]
# B Jets > 1	697 ± 7	106 ± 8 [6.6]	46 ± 4 [15]
e veto	626 ± 7	100 ± 8 [6.3]	42 ± 4 [15]
μ veto	488 ± 6	81 ± 7 [6.0]	35 ± 3 [14]
ΔR b Jets > 1.0	456 ± 6	77 ± 7 [5.9]	33 ± 3 [14]
$\Delta\phi(\not\!\!p_T, \mathrm{B}) > 0.5$	415 ± 6	56 ± 6 [7.4]	30 ± 3 [14]
min $\Delta\phi(\not\!\!E_T$,jets) > 0.8	214 ± 4	23 ± 4 [9.3]	15.3 ± 2.3 [14]

	N_{evt} (100 pb^{-1})		
	W+jet	**QCD**	**S/B**
no cut	1992 ± 14 [23]	-	-
$\not\!\!E_T > 35$ GeV	1219 ± 11 [29]	-	-
# of Light Jets > 1	784 ± 9 [38]	-	-
τ $p_T > 25$ GeV/c	32.8 ± 2.0 [66]	-	-
# B Jets > 0	19.4 ± 1.5 [90]	-	-
# B Jets > 1	4.5 ± 0.8 [1.5e+2]	131 ± 8 [5.3]	2.4
e veto	4.5 ± 0.8 [1.4e+2]	131 ± 8 [4.8]	2.3
μ veto	4.1 ± 0.8 [1.2e+2]	131 ± 8 [3.7]	2.0
ΔR b Jets > 1.0	3.2 ± 0.7 [1.4e+2]	117 ± 7 [3.9]	2.0
$\Delta\phi(\not\!\!p_T, \mathrm{B}) > 0.5$	3.0 ± 0.7 [1.4e+2]	82 ± 6 [5]	2.4
min $\Delta\phi(\not\!\!E_T$,jets) > 0.8	1.5 ± 0.6 [1.4e+2]	18 ± 3 [12]	3.7

is placed at 7.05, providing about 60% efficiency for the $t\bar{t}$ signal. This selection is well described in detail in Section 3.3.6. The expected number of events for this tight selection is quoted in Table 4.3.

Table 4.3: Number of events remaining after each selection requirement for signal and Standard Model background samples, using a tight b-tagging selection for 1 fb^{-1}. The rightmost column shows the signal over background ratio. QCD simulation includes a filter requiring at least 2 identified jets and $\not\!\!E_T > 20$ GeV to increase the generation efficiency. Therefore, no expected number of events for the first cuts are shown in the table. Errors quoted in this table correspond to the available MC statistics for each given sample (see Table 3.1). Numbers in parentheses are the S/B ratio for the each background.

	N_{evt} (1 fb^{-1})		
	Non hadronic t$\bar{t}$	**Hadronic t$\bar{t}$**	**Single top**
no cut	4.500e+5 ± 6e+2	3.852e+5 ± 1.4e+3 [1.2]	1.122e+5 ± 5e+2 [4.0]
$\not\!\!E_T > 35$ GeV	3.500e+5 ± 5e+2	4.86e+4 ± 5e+2 [7.2]	8.13e+4 ± 5e+2 [4.3]
# of Light Jets > 1	3.144e+5 ± 5e+2	4.84e+4 ± 5e+2 [6.5]	6.53e+4 ± 4e+2 [4.8]
τ $p_T > 25$ GeV/c	2.315e+4 ± 1.3e+2	2.35e+3 ± 1.2e+2 [9.9]	3.5e+3 ± 1e+2 [6.6]
# B Jets > 0	1.555e+4 ± 1.1e+2	1.78e+3 ± 1.0e+2 [8.7]	1.71e+3 ± 7e+1 [9.1]
# B Jets > 1	4.18e+3 ± 6e+1	6.3e+2 ± 6e+1 [6.6]	2.5e+2 ± 3e+1 [17]
e veto	3.80e+3 ± 5e+1	6.0e+2 ± 6e+1 [6.3]	2.4e+2 ± 3e+1 [16]
μ veto	3.09e+3 ± 5e+1	5.2e+2 ± 6e+1 [5.9]	2.1e+2 ± 3e+1 [15]
ΔR b Jets > 1.0	2.87e+3 ± 5e+1	4.8e+2 ± 6e+1 [6.0]	2.0e+2 ± 3e+1 [14]
$\Delta\phi(\not\!\!p_T, \mathrm{B}) > 0.5$	2.66e+3 ± 5e+1	3.2e+2 ± 5e+1 [8.3]	1.9e+2 ± 3e+1 [14]
min $\Delta\phi(\not\!\!E_T$,jets) > 0.8	1.33e+3 ± 3e+1	74 ± 25 [18]	94 ± 19 [14]

	N_{evt} (1 fb^{-1})		
	W+jet	**QCD**	**S/B**
no cut	1.992e+4 ± 1.4e+2 [23]	-	
$\not\!\!E_T > 35$ GeV	1.219e+4 ± 1.1e+2 [29]	-	
# of Light Jets > 1	8.61e+3 ± 9e+1 [37]	-	
τ $p_T > 25$ GeV/c	371 ± 21 [62]	-	
# B Jets > 0	177 ± 15 [88]	-	
# B Jets > 1	24 ± 7 [1.7e+2]	0 ± 10 [inf]	4.6
e veto	24 ± 7 [1.6e+2]	0 ± 10 [inf]	4.4
μ veto	22 ± 6 [1.4e+2]	0 ± 10 [inf]	4.1
ΔR b Jets > 1.0	19 ± 6 [1.5e+2]	0 ± 10 [inf]	4.1
$\Delta\phi(\not\!\!p_T, \mathrm{B}) > 0.5$	18 ± 6 [1.5e+2]	0 ± 10 [inf]	5
min $\Delta\phi(\not\!\!E_T$,jets) > 0.8	8 ± 5 [1.7e+2]	0 ± 10 [inf]	7.6

4.5 ATLFAST - Full Simulation Comparison of $t\bar{t}$ Kinematical Variables

As estated in Section 3.4, a large production of ATLFAST samples is needed to evaluate the impact of QCD di-jets background on the $t\bar{t}$ analysis. The amount of QCD events generated

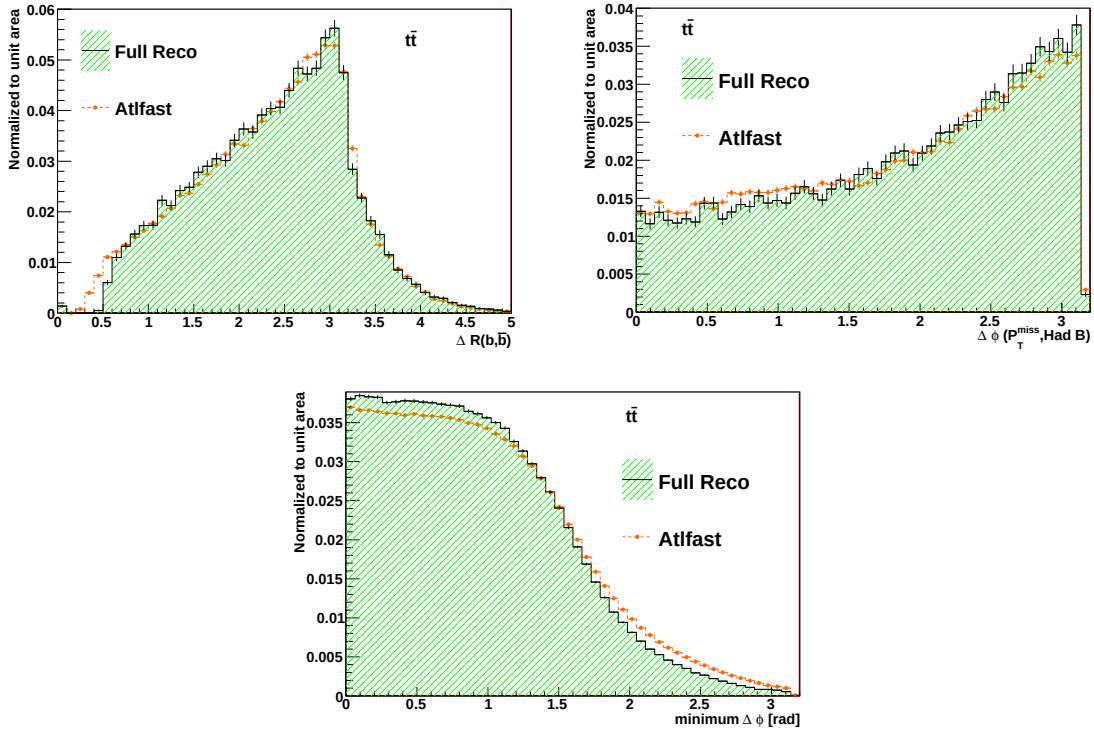

Figure 4.14: Comparison between ATLFAST and full simulation for topology variables of $t\bar{t}$ events. The upper plots show the angular distance between the two selected b-jets (left) and the azimuthal angle between the missing momentum and the b-jet on the hadronic side (right). The bottom plot shows the minimum of the azimuthal angle between the missing momentum and the 3 leading jets. Distributions are plotted for events that pass the basic selection cut: $\not\!\!E_T >$ 35 GeV , # of Light Jets > 1, τ $p_T > 25$ GeV/c , # B Jets > 1 and e,μ veto.

and simulated with ATLFAST is summarized on Table 3.1.

Before being able to estimate the amount of QCD background that remains after the $t\bar{t}$ event selection, we need to validate the performance of the ATLFAST simulation and understand the impact of the differences present between ATLFAST and full simulation.

Section 3.4.1 presented the performance of the ATLFAST simulation and a comparison with the full simulation for all the basic elements used in the analysis, like τ identification, $\not\!\!E_T$ or b-tagging.

This section makes a comparison of variables used in the event selection once the $t\bar{t}$ event is fully reconstructed. These variables respond to the typical $t\bar{t}$ topology (see Section 4.2) and are suitable to reject background processes with different event topologies like QCD dijets.

Figure 4.14 shows the three variables used in the event selection related to the $t\bar{t}$ topology. The agreement is quite acceptable and can be quantitatively evaluated inspecting the Table 4.4.

Although not explicitly used in the event selection, the four invariant mass distributions are useful to extract the amount of background present in data through fit methods, and are shown in Figure 4.15.

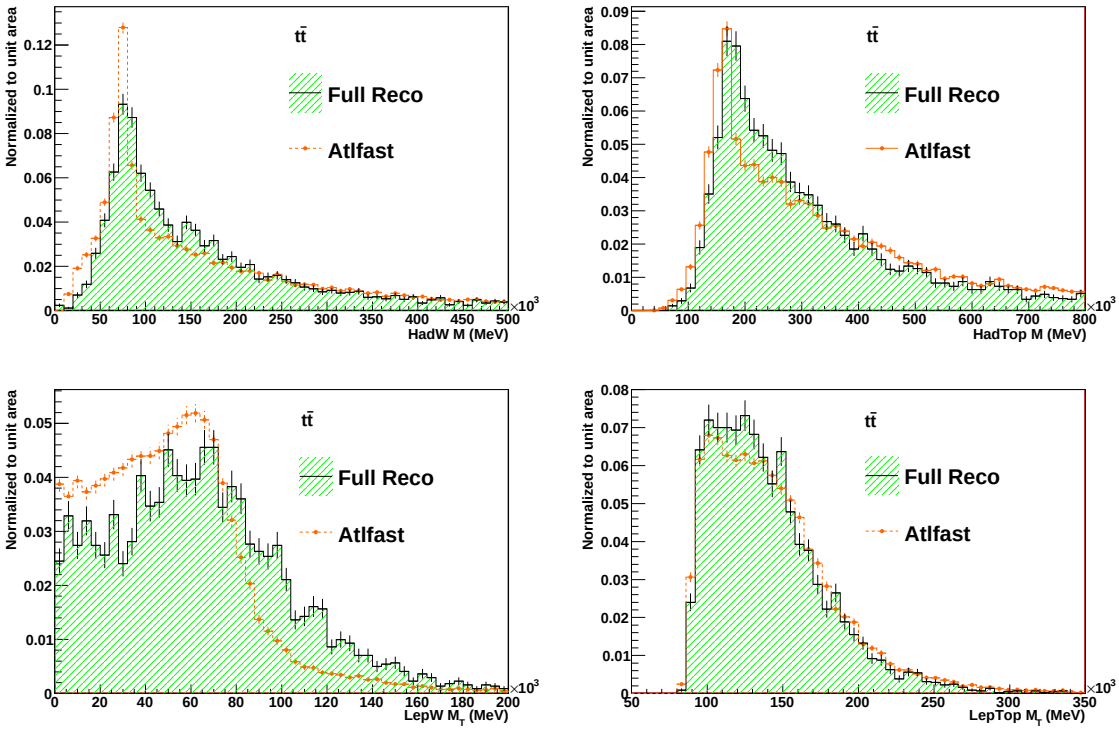

Figure 4.15: Comparison between ATLFAST and full simulation for invariant masses in the hadronic side and transverse masses in the leptonic side of $t\bar{t}$ events. Distributions are plotted for events that pass the basic selection cut: $\not\!\!E_T > 35$ GeV , # of Light Jets > 1, τ $p_T > 25$ GeV/c , # B Jets > 1 and e,μ veto.

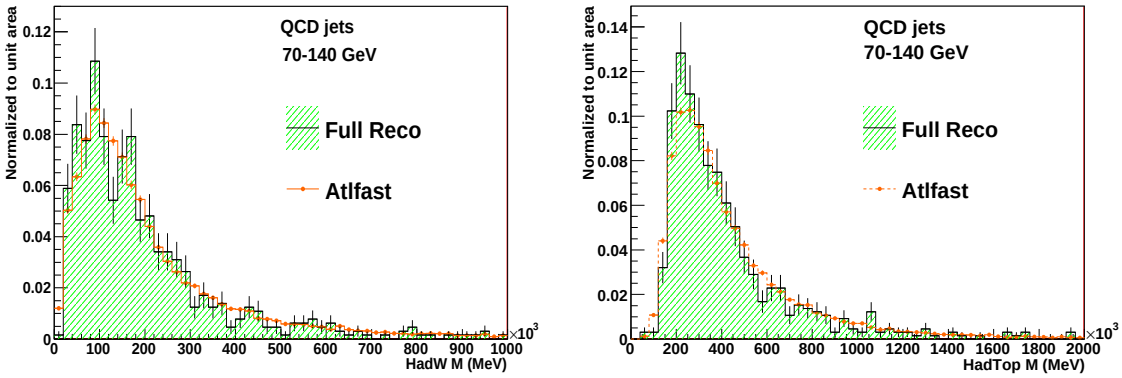

Figure 4.16: Comparison between ATLFAST and full simulation for invariant masses in the hadronic side for QCD dijets events in the range 70-140 GeV. Distributions are plotted for events that pass the basic selection cut: $\not{E}_T > 20$ GeV , # of Light Jets > 1, # B Jets > 1. The basic selection cuts are relaxed here to increase the acceptance of number of simulation events that pass the selection due to the limited statistics of full simulation samples for QCD processes (see Table 3.1).

Table 4.4: Comparison between ATLFAST and full simulation for topology variable cuts in $t\bar{t}$ events. Cuts applied are cumulative being the basic selection cut: $\not{E}_T > 35$ GeV , # of Light Jets > 1, τ $p_T > 25$ GeV/c , # B Jets > 1 and e,μ veto. Columns show the number of events after each selection cut for full simulation and ATLFAST and the efficiency relative to the previous cut.

	Full sim	**Eff (%)**	ATLFAST	**Eff (%)**
basic selection cut	6270 ± 80	-	41000 ± 200	-
ΔR b Jets > 1.0	5810 ± 80	92.7 ± 1.6	37560 ± 190	91.7 ± 0.7
$\Delta\phi(\not{p}_{\mathrm{T}}, \mathrm{B}) > 0.5$	5300 ± 70	91.3 ± 1.7	33800 ± 180	90.0 ± 0.7
min $\Delta\phi(\not{E}_T$,jets$) > 0.8$	2580 ± 50	48.7 ± 1.2	16710 ± 130	49.4 ± 0.5

Particularly important to compute the amount of background present in data after the event selection is the fact that for $t\bar{t}$ events the invariant masses of the hadronic side for the ATLFAST distributions are shifted with respect to the full simulation. This disagreement is explained due to the shift of the mean value of $\Delta p_T = p_T^{reco} - p_T^{truth}$ of reconstructed particle jets present in ATLFAST samples (see Figure 3.26). This effect appears only in those $t\bar{t}$ events where the hadronic top or hadronic W is well reconstructed (meaning that this reconstructed particle matches the truth quark or W boson) and conforms the peak of the invariant mass distributions, while it is not present at the tails, filled with events where the reconstructed hadronic top or hadronic W do not match the truth particle. This can be confirmed by looking at the hadronic invariant masses on QCD events, where no top quarks or W bosons are expected (Figure 4.16). Here the

shape of the invariant masses agrees well between full simulation and ATLFAST, what allows the use of the QCD samples to estimate the amount of background present in the data (Section 4.8).

4.6 Systematic Uncertainties

In the analysis of $t\bar{t}$ decays with $(qq'\tau_{had})$ final state the most relevant contributions to the detector uncertainties are the jet and $\not\!\!E_T$ energy scales, b–tagging efficiency and tau identification efficiency. In order to estimate the detector contribution to the systematic uncertainty on the cross section measurement its performance has been varied within the range of accuracy that is expected for data sets of 100 pb^{-1} and 1 fb^{-1}. The corresponding variation of the number of selected $t\bar{t} \to W(qq')W(\tau_{had}\nu)b\bar{b}$ candidates in the non hadronic $t\bar{t}$ sample is evaluated and presented in the following sections for the main sources of systematic errors. A more complete discussion on how to relate the number of candidate events to the $t\bar{t} \to W(qq')W(\tau_{had}\nu)b\bar{b}$ cross section is given in section 4.7. With present MC statistics, the variation of the cross section is dominated by the signal contribution, while SM background processes yield minor contributions.

4.6.1 Jets and Missing Transverse Energy

Jet energy scale (including τ jets) and $\not\!\!E_T$ energy have been systematically rescaled by 10%, 5% and 2% corresponding respectively to the expected precision of the 100 pb^{-1}, 1 fb^{-1} and 10 fb^{-1} scenarios. The soft component of the $\not\!\!E_T$ has been also smeared by 10% in the following way: the contribution to the $\not\!\!E_T$ from jets and leptons with transverse momentum above 20 GeV/c has been removed, the remaining component has been smeared by 10% (for all luminosities) and then lepton and jet contributions have been added back.

The systematic variation of the number of selected events due to different values of the jet energy scale is reported in Table 4.5.

Table 4.5: Systematic variation of the number of selected events due to the change of the jet energy scale. Variations are relative to a jet energy scale value of 1. The quoted error originates from MC statistics only.

Systematic Variation	
Jet energy scale	**#events variation**
0.90	0.920 ± 0.017
0.95	0.983 ± 0.008
0.98	0.993 ± 0.005
1.00	1
1.02	1
1.05	1.014 ± 0.007
1.10	1.056 ± 0.014

4.6.2 B-tagging Efficiency

The b-tagging efficiency plays an important role in the $t\bar{t} \to W(qq')W(\tau_{had}\nu)b\bar{b}$ reconstruction as one of the selection criteria is that the two b–jets expected in the final state should be reconstructed and correctly identified. The systematic uncertainty due to heavy flavour tagging has been estimated by varying the b–tagging efficiency by 5% and its light quark rejection factor by 10%. The corresponding systematic variations on the number of selected events measured are presented in Table 4.6.

Table 4.6: Systematic variation of the number of selected events due to the change of the b-tagging efficiency. Variations are relative to a nominal b-tagging efficiency of 67.4% and to a light quark rejection factor of 10.8 . The quoted error is derived from MC statistics only.

Systematic Variation	
b-tagging efficiency / Nominal value	**#events variation**
0.95	0.875 ± 0.018
1.05	1.025 ± 0.009
Light quark rejection / Nominal value	**#events variation**
0.90	1.018 ± 0.008
1.10	1.007 ± 0.005

4.6.3 Tau Identification Efficiency

The systematic contribution to the measurement of the number of the $t\bar{t} \to W(qq')W(\tau_{had}\nu)b\bar{b}$ cross section due to the τ identification efficiency has been estimated by varying the tau identification efficiency and the light quark rejection factor by 10%. The systematic variation of the number of selected events due to different values of the τ identification efficiency is reported in Table 4.7.

Table 4.7: Systematic variation of the number of selected events due to the change of the τ identification efficiency and light quarks rejection factor. Variations are relative to a nominal τ identification efficiency of 50.0% and to a light quark rejection factor of 6.2 . The quoted error is derived from MC statistics only.

Systematic Variation	
τ-id efficiency / Nominal value	**#events variation**
0.90	0.986 ± 0.007
1.10	1.053 ± 0.013
Light quark rejection / nominal value	**#events variation**
0.90	1.032 ± 0.011
1.10	1.057 ± 0.014

4.7 Cross Section Determination

The $t\bar{t} \rightarrow W(qq')W(\tau_{had}\nu)b\bar{b}$ cross section can be determined through a counting method:

$$\sigma = \frac{N_{sig}}{\mathcal{L} \times \epsilon} = \frac{N_{obs} - N_{bkg}}{\mathcal{L} \times \epsilon} \tag{4.3}$$

where N_{obs} is the number of events measured after the event selection is applied to data, N_{bkg} is the number of background events that pass the selection estimated from Monte Carlo simulations or from data samples, $\mathcal{L}$ is the integrated luminosity and ϵ the efficiency of the event selection.

The first measurements of the luminosity at LHC can be expected with an uncertainty of about 20-30% although more precise determination methods using special runs of the machine dedicated to measure the instantaneus luminosity will reduced this uncertainty to 5%. Advanced methods to measure the luminosity in ATLAS, like the ALFA detector [75] that will measure elastic scattering in the Coulomb-nuclear interference region using special runs and beam optics, or the use of the optical theorem together with a precise measurement of the total cross section [76] can achieve an uncertainty on the luminosity measurement of the order of 3%.

The systematics uncertainties considered in the calculation of the cross section are summarized in Table 4.8.

Table 4.8: Systematic uncertainties for cross section determination. For the jet energy scale, a variation of 5% on jet energy scale and $\not{E}_T$ was considered.

Source	Uncertainty (%)
Jet Energy Scale	8
b-tagging identification	13
τ identification	6

Assuming the number of background events for 100 pb^{-1} can be estimated with a precision of a 20%, and an uncertainty on the luminosity of 5%, the following accuracy for the measurement of the cross section is expected:

$$\frac{\Delta\sigma}{\sigma} = (6(\text{stat}) \pm 4(\text{bkg}) \pm 16(\text{sys}) \pm 5(\text{lumi}))\,\% \tag{4.4}$$

Other sources of systematics not studied in this analysis are the PDFs and the initial state radiation (ISR) and final state radiation (FSR) uncertainties. Similar $t\bar{t}$ analyses on the lepton channel [77] determine a systematic due to the PDF of about 2% and a contribution from the ISR/FSR of about 10%.

4.8 Estimation of QCD Background from Data

The invariant mass distributions on the hadronic side give us some information to discriminate the "pure" signal events (those $t\bar{t}$ events where the selected light jets and b-jet to build the hadronic top were the correct combination and therefore, the reconstructed hadronic top matches the true quark) from the physics background and the combinatorial background ($t\bar{t}$ events where the hadronic top was not the correct combination of jets and b-jet and therefore the reconstructed particle does not match the true quark). As the reconstructed hadronic top in combinatorial background events does not correspond to the true top quark, these events contribute to the invariant mass distributions with a shape typical of physics background events, even if they are $t\bar{t}$ signal events.

The difference in shape of the invariant mass distributions between signal and SM backgrounds is not well appreciated in Figure 4.13 due to the small amount of background that pass the event selection. Figures 4.17 and 4.18 show the same distributions with a QCD cross section increased by a factor 500% (with respect to the QCD cross section used in the analysis, Table 3.1) , in order to be able to observe by naked eye the shape differences and show the disentangling power between signal and background for the different strategies.

Among the different strategies proposed in Section 4.2, the BestPDG-ClosestDR strategy biases the background in such a way that both, signal and background fit well to a Gaussian distribution. On the contrary, the other three strategies, although leading to much wider distributions, provide a better separation between the signal, following a Gaussian distribution, and the background, with longer tails at high invariant mass values.

Here, a combined fit of a fourth order Chebyshev polynomial plus a Gaussian distribution will properly distinguish between the *pure* signal events on the one hand, and the physics and combinatorial background on the other hand, as it can be seen in Figures 4.17 and 4.18. The relation between the parameters of the Chebyshev polynomial and the Gaussian distribution extracted from the fit will depend on the amount of background present in data.

The cross section for QCD multijet processes is very uncertain, and the invariant masses produced with data after the event selection may differ from what we expect from the Monte Carlo. The parameters of the fits to the invariant masses distributions represent a measurement of the amount of QCD background present in the data if we assume that the only unknown is the value of the cross section, while other properties of the QCD process, like the jet multiplicity from radiation and the kinematics of the event are well simulated by the Monte Carlo.

This section illustrates how we can estimate the amount of QCD present in data through the fit method. First, the hadronic W and hadronic top are plotted for $t\bar{t}$ and the physical background for an integrated luminosity of 100 pb^{-1}. QCD distributions are then increased by a given percentage in their normalizations: 1%,2%,5%... , with respect to the cross section assumed in the Monte Carlo production (Table 3.1) with the assumption that the shape of the invariant mass distributions remains unchanged. Finally the distributions are fitted with a combination of a Gaussian distribution and a fourth order Chebyshev polynomial. The parameters of the fit

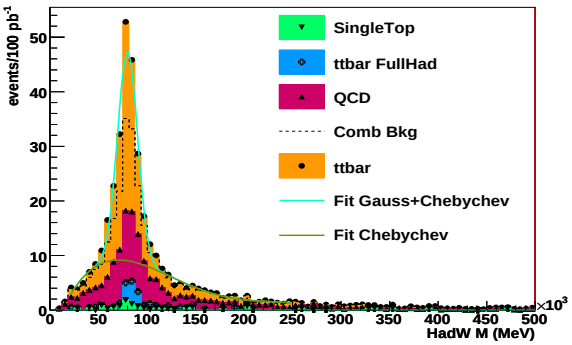

(a) Best PDG - Closest ΔR

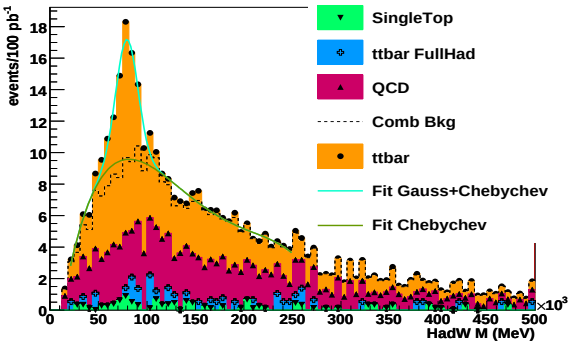

(b) Highest Jets - Highest b-Jet

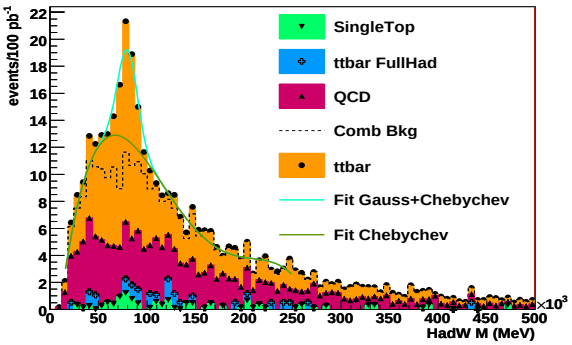

(c) Highest composite particle

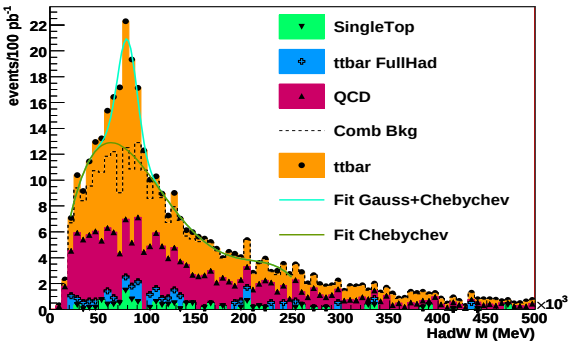

(d) Highest composite (build hadronic top first)

Figure 4.17: Hadronic W invariant mass distributions for $t\bar{t}$ signal and SM background for the four different strategies. The dashed line indicates the $t\bar{t}$ combinatorial backround. The two curves represent the fit to the physical plus combinatorial background through a fourth order Chebyshev polynomial and the fit adding also a Gaussian distribution for the signal. Distributions are normalized to 100 pb^{-1} and the QCD background was artificially incremented by 500% in order to show grafically how these fits can extract information on the amount of QCD background present in the data.

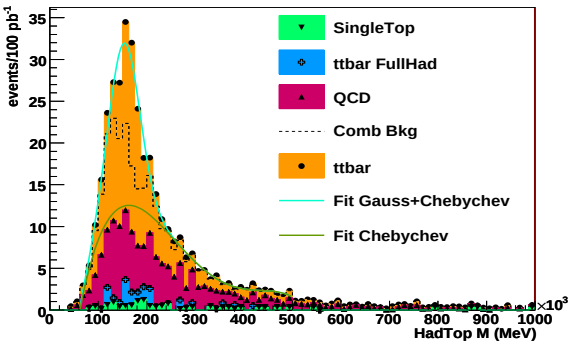

(a) Best PDG - Closest ΔR

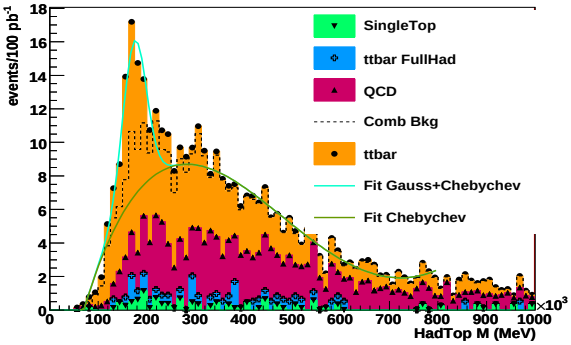

(b) Highest Jets - Highest b-Jet

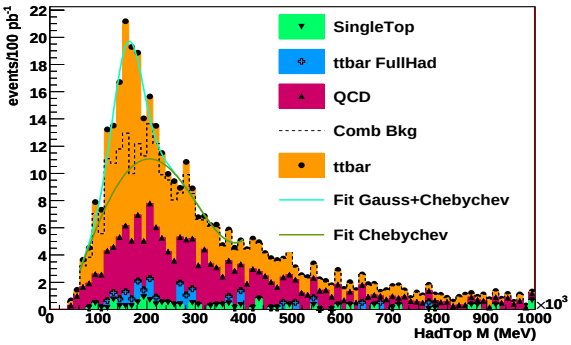

(c) Highest composite particle

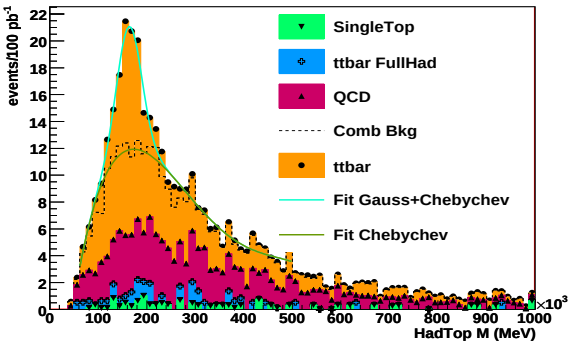

(d) Highest composite (build hadronic top first)

Figure 4.18: Hadronic top invariant mass distributions for $t\bar{t}$ signal and SM background for the four different strategies. The dashed line indicates the $t\bar{t}$ combinatorial backround. The two curves represent the fit to the physical plus combinatorial background through a fourth order Chebyshev polynomial and the fit adding also a Gaussian distribution for the signal. Distributions are normalized to 100 pb^{-1} and the QCD background was artificially incremented by 500% in order to show grafically how these fits can extract information on the amount of QCD background present

will vary with the amount of QCD that was artificialy introduced in the data.

With the gradual increase of QCD background, two effects are observed concerning the fit: 1) The integral of the distribution under the Chebyshev curve increases while the integral of the distribution under the Gaussian curve remains unchanged. 2) The maximum of the Chebyshev polinomial is gradually shifted with respect to the Gaussian maximum.

Two variables sensitive to this variation are considered: the ratio of the integral of the Gaussian and the Chebyshev distributions, and the distance between the maximum value of the two distributions. The dependence of the fit parameters with the amount of QCD present in the distributions is shown for the (*Highest Jets - Highest b-Jet*) strategy in Figure 4.19.

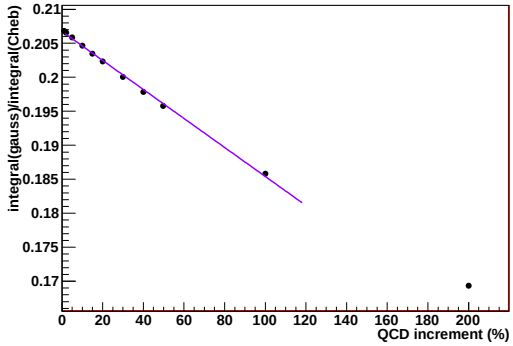

(a) Ratio of integrals for hadronic W

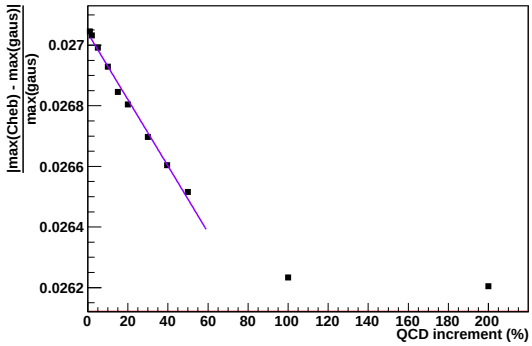

(b) Distance between maxima for hadronic W

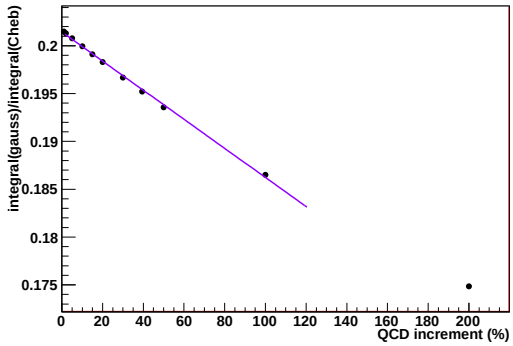

(c) Ratio of integrals for hadronic top

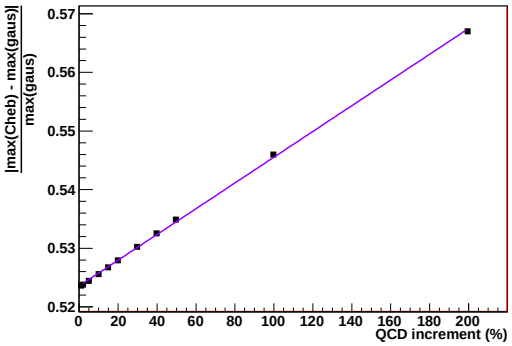

(d) Distance between maxima for hadronic top

Figure 4.19: Parameters extracted from the fit of the hadronic W and top distributions to a Gaussian (that represents the signal) plus a fourth order Chebyshev polynomial (that represents the physical background plus the combinatorial background), using the *Highest Jets - Highest b-Jet* strategy. The left plots show the ratio of the integral of the Gaussian distribution and the integral of the Chebyshev polynomial, while the plots at the right show the distance between the maximum of the Gauss and Chebyshev polynomial normalized by the value of the maximum of the Gaussian fit.

When data are analyzed, the measurement of these two parameters of the fits can be used as an indirect measurement of the amount of background present. Although the method is presented here as a measurement of the QCD background, as it is the process with the highest

uncertainty in the cross section, the fit method in fact measures the total amount of the SM background with the only asumption that the distributions of the invariant masses follow the same shape for all the SM background processes and that the combinatorial background of $t\bar{t}$ events is well described by the Monte Carlo. The electron channel (Section 4.11), which provides a higher signal and lepton purity will be used to validate the kinematics of the $t\bar{t}$ in Monte Carlo, and in particular the combinatorial background. This will be a benchmark for the quality of the MC and the associated systematic uncertainty.

4.9 Contribution of New Physics

If the supersymmetric partners of quarks and gluons, squarks and gluinos respectively, exist and are not very massive, they will be produced at the LHC with cross-sections that may be sufficiently large to compete with the $t\bar{t}$ cross section. In many supersymmetric models, the squarks and gluinos are unstable and will decay in a chain to energetic jets and leptons (see Section 1.2.3) and further lower-mass SUSY particles. If, in addition, R-parity is conserved (as there are strong arguments to believe), the lightest SUSY particle (LSP) will be stable and will scape the detector unseen, becoming an important source of $\not\!\!E_T$.

Thus, in this scenario, the general SUSY signature is composed by many energetic jets and significant missing transverse energy, possibly accompanied by one or more energetic, isolated leptons. This signature is very similar to the topology generated in a typical $t\bar{t}$ event. Therefore, the presence of new physics may be an important background to the $t\bar{t} \rightarrow (\tau\nu b)\ \ (q\bar{q}b)$ cross section analysis. Or seen the other way around, any excess of events observed in the $t\bar{t}$ analysis not predicted from the Monte Carlo might be an indication of new physics at the TeV scale.

It is not possible to discuss all the existing beyond the Standard Model models and the full range of their parameters space. Instead, it was chosen to quote the effects of a number of specific SUSY models. Each model is a separate different point in the mSUGRA framework. Together, these points give a flavour of how the presence of SUSY can affect the $t\bar{t}$ estimations. Table 4.9 lists the mSUGRA parameters of the samples under study, and their leading-order cross-sections, and Table 4.10 summarizes the generator and the number of events produced in the Monte Carlo simulation for the same samples.

Table 4.9: mSUGRA parameters of the SUSY samples under study. For all samples, $\mu > 0$.

Sample		$\mathbf{m_o}$(GeV)	$\mathbf{m_{1/2}}$(GeV)	$\mathbf{A_o}$(GeV)	$\tan\beta$	$\sigma^{\mathbf{LO}}$ **(pb)**	$\sigma^{\mathbf{NLO}}$ **(pb)**
SU1	coannihilation	70	350	0	10	8.15	10.86
SU2	focus point	3550	300	0	10	5.17	7.18
SU3	bulk	100	300	-300	6	20.85	27.68
SU4	low mass	200	160	-400	10	294	402
SU6	funnal	320	375	0	50	4.47	6.07
SU8	coannihilation	210	360	0	40	6.48	8.70

Table 4.10: Generators and number of events generated for each SUSY sample.

Sample	**Generator**	$\mathbf{N_{events}}$
SU1	IsaSUSY + HERWIG	200 K
SU2	IsaSUSY + HERWIG	50 K
SU3	IsaSUSY + HERWIG	500 K
SU4	IsaSUSY + HERWIG	200 K
SU6	IsaSUSY + HERWIG	30 K
SU8	IsaSUSY + HERWIG	50 K

The chosen samples provide a wide range of possible decay topologies. For all points, the gluino mass is less than 1 TeV, the ratio $M(\tilde{g})/M(\tilde{\chi}_1^o) = 6 - 8$, and $\mu > 0$. The SUSY event samples were generated with IsaSUSY (part of IsaJet [78]), interfaced to Herwig.

As shown in Table 4.9, the cross section for the supersymmetric process depends very much on the point chosen, varying from a few pico-barn up to the 400 pico-barn of the point SU4. Therefore the impact of the presence of new physics in the $t\bar{t}$ analysis will be very sensitive to the nature of the physics beyond the Standard Model.

In any case, even if the kinematics may also differ very much among the different points, the invariant masses extracted after applying the event selection, follow the same shape as the $t\bar{t}$ signal in all cases, as one can see in Figure 4.20 (for the hadronic W invariant mass) and Figure 4.21 (for the hadronic top invariant mass). This reduces the possibility of a clear discovery of new physics by comparing the experimental invariant masses with the Standard Model hipothesis, although one can expect an important excess in the number of events that pass the event selection if new physics processes have a large enough cross section, like is the case for the SU4 point.

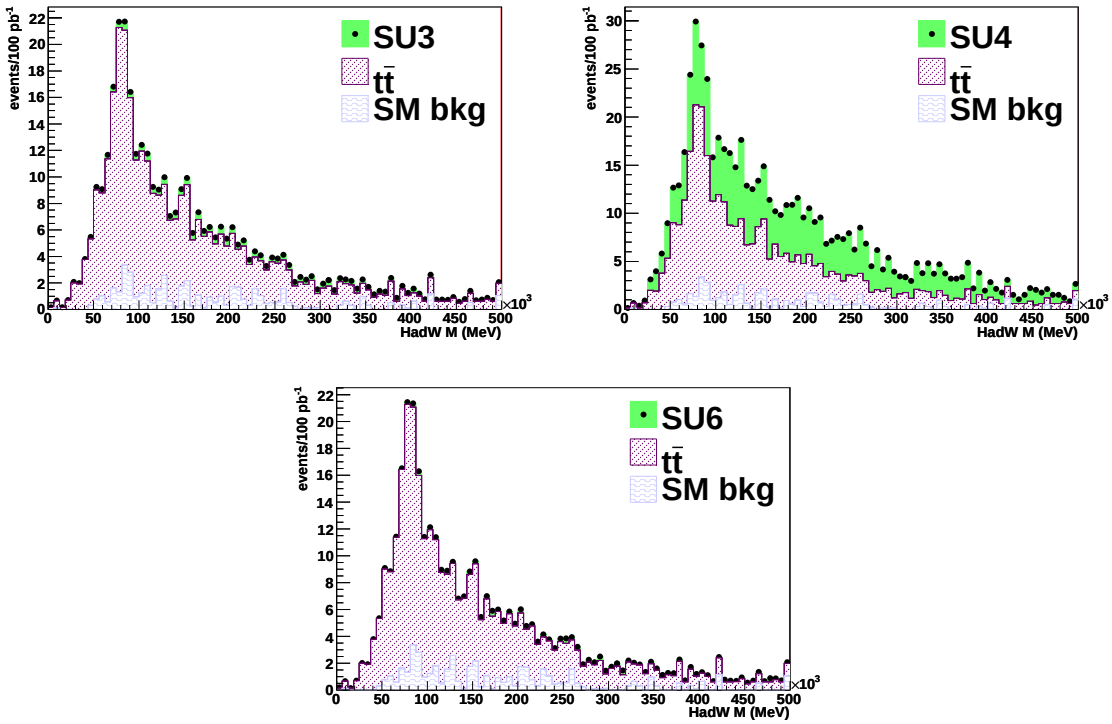

Figure 4.20: Hadronic W invariant mass distributions after event selection for $t\bar{t}$ signal, Standard Model background and different mSUGRA points. Only the mSUGRA points with a significant contribution in number of events are shown. Distributions are normalized to an integrated luminosity of 100 pb^{-1}.

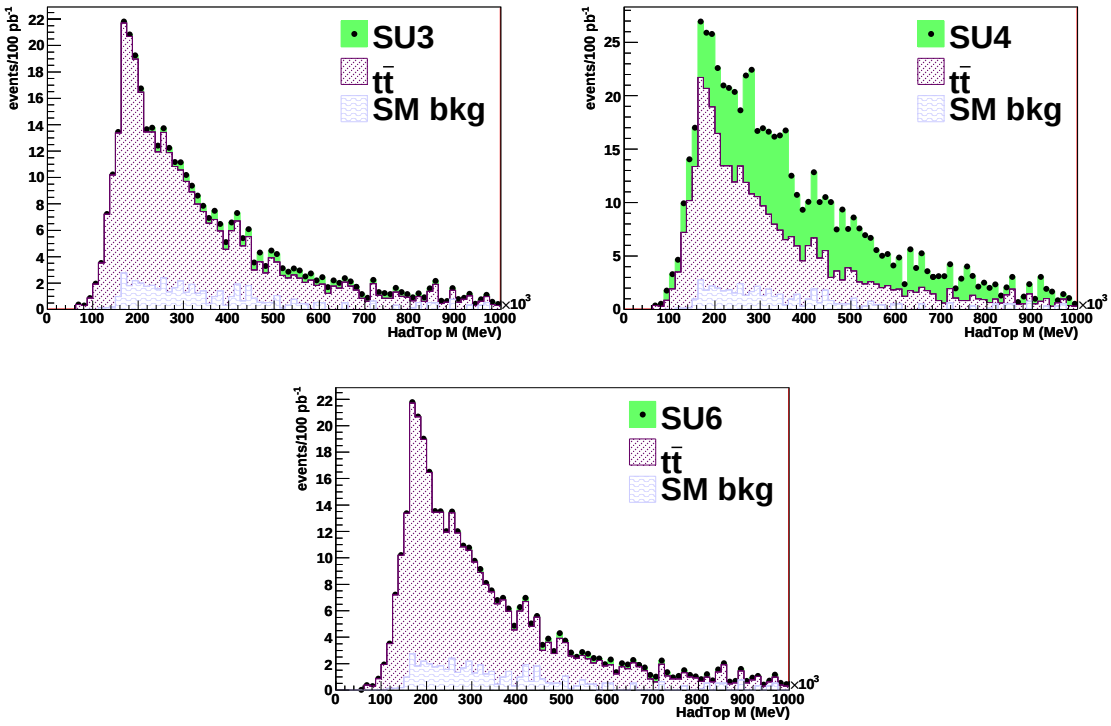

Figure 4.21: Hadronic top invariant mass distributions after event selection for $t\bar{t}$ signal, Standard Model background and different mSUGRA points. Only the mSUGRA points with a significant contribution in number of events are shown. Distributions are normalized to an integrated luminosity of 100 pb^{-1}.

Table 4.11: Number of events remaining after each selection for different points of the mSUGRA model. The event reconstruction was carried out with a loose b-tagging selection. Numbers are normalized to an integrated luminosity of 100 pb^{-1}. Errors quoted in this table correspond to the available MC statistics for a given sample (see Table 4.10). Numbers in parentheses are the S/B ratio for the each background.

	N_{evt} (100 pb^{-1})		
	SU1	**SU2**	**SU3**
no cut	1114 +- 5 [40]	729 +- 3 [62]	2788 +- 6 [16]
$\not\!\!E_T > 35$ GeV	1072 +- 5 [33]	483 +- 3 [72]	2706 +- 6 [13]
# of Light Jets > 1	992 +- 5 [31]	347.3 +- 2.3 [87]	2567 +- 6 [12]
τ $p_T > 25$ GeV/c	79.4 +- 1.4 [33]	26.2 +- 0.6 [99]	417 +- 3 [6.2]
# B Jets > 0	41.8 +- 1.1 [52]	10.2 +- 0.4 [2.1e+2]	215.2 +- 1.8 [10]
# B Jets > 1	20.3 +- 0.7 [49]	6.2 +- 0.3 [1.6e+2]	94.3 +- 1.2 [11]
e veto	16.5 +- 0.7 [54]	4.8 +- 0.3 [1.9e+2]	80.9 +- 1.1 [11]
μ veto	11.5 +- 0.6 [61]	2.68 +- 0.21 [2.6e+2]	60.2 +- 1.0 [12]
ΔR b Jets > 1.0	9.9 +- 0.5 [66]	2.37 +- 0.20 [2.8e+2]	52.9 +- 0.9 [13]
$\Delta\phi(\not\!\!p_{\mathrm{T}}, \mathrm{B}) > 0.5$	9.2 +- 0.5 [65]	2.12 +- 0.19 [2.8e+2]	48.2 +- 0.9 [12]
min $\Delta\phi(\not\!\!E_T$,jets) > 0.8	6.1 +- 0.4 [52]	1.30 +- 0.15 [2.4e+2]	30.4 +- 0.7 [10]

	N_{evt} (100 pb^{-1})		
	SU4	**SU6**	**SU8**
no cut	3.930e+4 +- 9e+1 [1.1]	672 +- 4 [67]	966 +- 4 [47]
$\not\!\!E_T > 35$ GeV	3.609e+4 +- 9e+1 [0.97]	650 +- 4 [54]	934 +- 4 [37]
# of Light Jets > 1	3.378e+4 +- 9e+1 [0.90]	616 +- 4 [49]	874 +- 4 [35]
τ $p_T > 25$ GeV/c	2109 +- 22 [1.2]	148.2 +- 1.9 [17]	116 +- 1.6 [22]
# B Jets > 0	1645 +- 20 [1.3]	95.7 +- 1.5 [23]	67.2 +- 1.2 [32]
# B Jets > 1	940 +- 15 [1.1]	53.2 +- 1.1 [19]	33.8 +- 0.9 [29]
e veto	825 +- 14 [1.1]	45.8 +- 1.0 [19]	30.4 +- 0.8 [29]
μ veto	637 +- 12 [1.1]	31.5 +- 0.9 [22]	22.0 +- 0.7 [32]
ΔR b Jets > 1.0	550 +- 11 [1.2]	27.6 +- 0.8 [24]	19.1 +- 0.6 [34]
$\Delta\phi(\not\!\!p_{\mathrm{T}}, \mathrm{B}) > 0.5$	500 +- 11 [1.2]	25.5 +- 0.8 [23]	17.8 +- 0.6 [34]
min $\Delta\phi(\not\!\!E_T$,jets) > 0.8	282 +- 8 [1.1]	16.6 +- 0.6 [19]	11.7 +- 0.5 [27]

The excess in number of events expected for every mSUGRA point after applying the event selection is summarized in Table 4.11 for an integrated luminosity of 100 pb^{-1}.

The topology of the SUSY events is quite similar to that of the $t\bar{t}$, with high jet-multiplicity, large $\not\!\!E_T$ and isolated leptons signatures. Therefore, in the case where the cross section is large enough, like in the SU4 point, the excess in the number of events is about the same order of magnitude than the signal, what would become a clear evidence of new physics, once the Standard Model background is well understood.

Although the shape of the invariant masses remains unchanged if SUSY is present, this is

not the case for the $\not\!\!E_T$ and the *Effective Mass* (MEff) variable, defined as the sum of the $\not\!\!E_T$ and all high p_T objects present in the event (jets, b-jets and leptons).

The $\not\!\!E_T$ and MEff distributions are shown in Figure 4.22 for the SU3 and SU4 points, which are the points that will produce the highest contamination. Although the shapes depend on the mSUGRA point, a general behaviour for all cases is an excess at the high $\not\!\!E_T$ and MEff tails compared to the Standard Model distributions. This excess can be used as a discovery tool once enough luminosity is collected (about 1 fb^{-1}). Similar excesses will be present in the electron and muon channel. While other inclusive *no lepton* mode SUSY searches will see larger excesses (due to less restrictive event selections) a nice feature of investigating the large $\not\!\!E_T$ tails in the $t\bar{t} \rightarrow \tau$ channel is that the Standard Model background can be completely neglected for $\not\!\!E_T$ above 200 GeV.

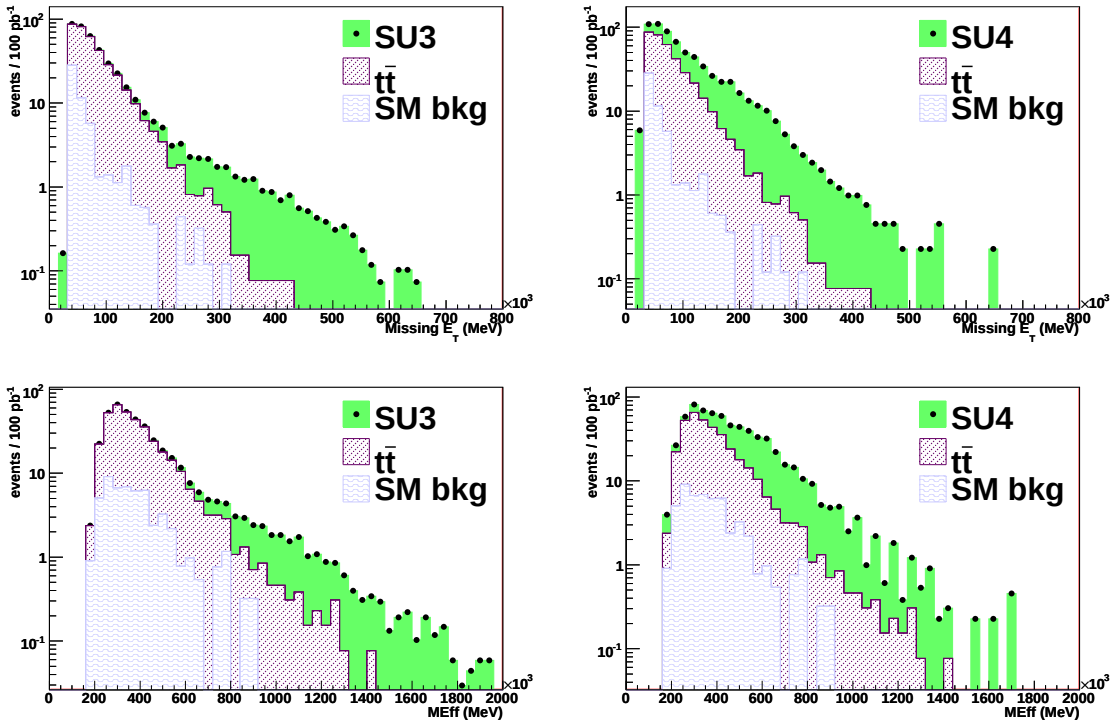

Figure 4.22: $\not\!\!E_T$ and Effective Mass distributions for the SU3 and SU4 SUSY points, normalized to 100 pb^{-1}. Accumulative distributions show the Standard Model background to the $t\bar{t}$ analysis, $t\bar{t} \rightarrow \tau$ signal and the SUSY events.

4.10 Trigger

The large multiplicity and variety of particles present in a $t\bar{t}$ event provide the possibility of triggering these events using various trigger menus. Semileptonic $t\bar{t}$ events with a hadronic tau can be triggered with multijet, τ, $\not\!\!E_T$ and b-jet triggers, or using them in combined menus in

order to allow lower E_T thresholds compared to standalone triggers, which typically need high E_T thresholds to keep the trigger rates low.

The following notation is used in this section to label the different trigger menus[2)]: j (jets), xe ($\not\!\!E_T$), tau (hadronically decaying τ) and b (b-jets). A prefix to the item determines the multiplicity of the trigger item while the suffix is the p_T threshold in GeV. If the presence of several trigger object types is required, the AND of these multiple object types is shown using an "_". As an example, tau20i_xe30 requires an isolated tau lepton with a p_T above 20 GeV and a $\not\!\!E_T$ above 30 GeV.

The initial LHC startup luminosity is expected to be approximately 10^{31} cm^{-2} s^{-1}. For this low luminosity, trigger menus will primarly be a combination of low p_T thresholds and loose selection criteria.

Table 4.12 shows the list of trigger menus (relevant for $t\bar{t}$ events with (qq', τ_{had})) planned for the initial luminosity of 10^{31} cm^{-2} s^{-1} and the rates estimated for the same luminosity with the prescales needed to keep them at reasonable levels so that the total trigger rate does not exceed 200 Hz. The rates have been estimated using seven million of non-difractive events with a cross section of approximately 70 mb generated with PYTHIA.

Table 4.12: List of proposed trigger menus for the LHC startup luminosity 10^{31} cm^{-2} s^{-1}. The first column shows the trigger item, the middle column shows the prescale for the item and the last column indicates the estimated trigger rate.

Menu	**Prescale**	**rate (Hz)**
single jet menu		
j10	42000	4
j18	6000	1
j23	2000	1
j35	500	1
j42	100	4
j70	15	4
j120	1	9
multijet menu		
4j23	1	7
tau menu		
tau60	1	10
tau25_XE30	1	3.5
other menu		
2b23	1	3.5

[2)] Trigger menus are tables of triggers that incorporate the signatures for various physics objects at each of the three trigger levels.

The first unprescaled single jet trigger places the p_T threshold at 120 GeV, too high to yield a reasonable acceptance for this analysis. Therefore, the most promising trigger menus will be the multijet triggers and the combination of tau and $\not\!\!E_T$ triggers. Although the startup LHC luminosity is 10^{31} cm^{-2} s^{-1}, the achievement of an integrated luminosity of 100 pb^{-1} will be reached with higher luminosities, like 10^{32} cm^{-2} s^{-1} . Experience with early running will allow further optimization of the trigger algorithms and menus and improve the ability to estimate rates in the high luminosity regime. As the LHC ramps up to its design luminosity, complex trigger signatures with multiple observables, higher pT thresholds and tighter selections will be deployed to maintain the output Event Filter rates at about 200 Hz.

Some of the trigger menus for 10^{32} cm^{-2} s^{-1} and the rates estimates are summarised in Table 4.13.

Table 4.13: List of proposed trigger menus for the LHC luminosity 10^{32} cm^{-2} s^{-1}. The first column shows the trigger item, the middle column shows the prescale for the item and the last column indicates the estimated trigger rate (for some of the trigger items, the rate has not been computed and therefore its inclusion in this table is merely orientative)

Menu	**Prescale**	**rate (Hz)**
single jet menu		
j20	3000000	1
j33	420000	1
j55	6000	1
j62	2000	1
j84	500	1
j120	100	1
j150	15	1
j200	1	10
multijet menu		
3j50	1	-
4j35	1	-
b-jet menu		
3b23_4j23	1	2
2b35_3j35	1	3
tau menu		
tau150	1	-
2tau35i	1	-
tau35i_xe40	1	-
tau25_4j23	1	-
$\not\!\!E_T$ menu		
xe70	1	-

The trigger menus configured with the Monte Carlo simulation in which this analysis was based do not match exactly the menus proposed for the initial luminosities (Tables 4.12 and 4.13),

based on results on trigger rates obtained later in time. Therefore, it was not possible to obtain the trigger efficiencies of the analysis for all the proposed trigger menus. On the other hand, new trigger menu combinations, like asymmetric jet triggers or multijet plus $\not\!\!E_T$ triggers were tested to motivate its inclusion as a new item in the trigger table.

Table 4.14 shows the Event Filter efficiencies for several trigger menus studied. Efficiencies are normalized to events that already passed the event selection (Section 4.4). While different multijet and tau trigger were considered, for b triggers only the b35 menu was available in the trigger simulation. The efficiencies for combined tau+b and tau+b+jet menus are obtained without considering overlap removal (not available in the simulation) among the different trigger objects.

Table 4.14: Event Filter trigger efficiencies for different menus (normalized to events that pass the event selection of the analysis -Section 4.4-).

Menu	**EF efficiency (%)**
multijet menu	
jet160	19
2jet120	11
2jet50+2jet20	70
2jet50+2jet20+$\not\!\!E_T$30	68
4jet20+$\not\!\!E_T$30	81
4jet50+$\not\!\!E_T$20	17
tau menu	
tau20i+$\not\!\!E_T$40	52
tau25i+$\not\!\!E_T$20	56
tau35i+$\not\!\!E_T$20	37
tau + b menu	
tau15i+b35	67
tau25i+b35	57
tau15i+b35+2jet20	67
tau15i+b35+2jet20+$\not\!\!E_T$20	65
Physics OR	95

In general, the four jet triggers provide very high efficiencies ($\sim 90\%$) and even in combination with $\not\!\!E_T$ keep efficiencies higher than 80 %. On the contrary, dijet trigger and single jet trigger, due to the large E_T threshold needed to keep an acceptable trigger rate, provide low efficiencies.

Figure 4.23 shows the ratio of events that pass a four jet trigger and all the events (normalized to the events that pass the event selection -Section 4.4-) versus the p_T of the reconstructed τ. The four jet trigger introduces a bias in the tau p_T spectrum due to the fact that in some events

that pass the 4 jet trigger one of the objects that fire the trigger may be a hadronically decaying tau. Increasing the threshold of the multijet trigger has the effect of increasing also the turn on curve of the bias observed in the tau p_T spectrum.

A combination of four jet triggers plus $\not\!\!E_T$ triggers allows us to reduce the jet p_T threshold of the multijet triggers and, as shown in Figure 4.24, will help reducing this bias in the tau spectrum, what will be important due to the low p_T spectrum of τ's in $t\bar{t}$ events. Another reason to use the four jet triggers in combination with the $\not\!\!E_T$ trigger is the fact that the 4 jet trigger efficiency decreases rapidly with the p_T threshold, as it is shown in Figure 4.25, and therefore, it is desirable to keep this threshold as low as possible and to increase the $\not\!\!E_T$ threshold if needed to keep the trigger rates at a reasonable level.

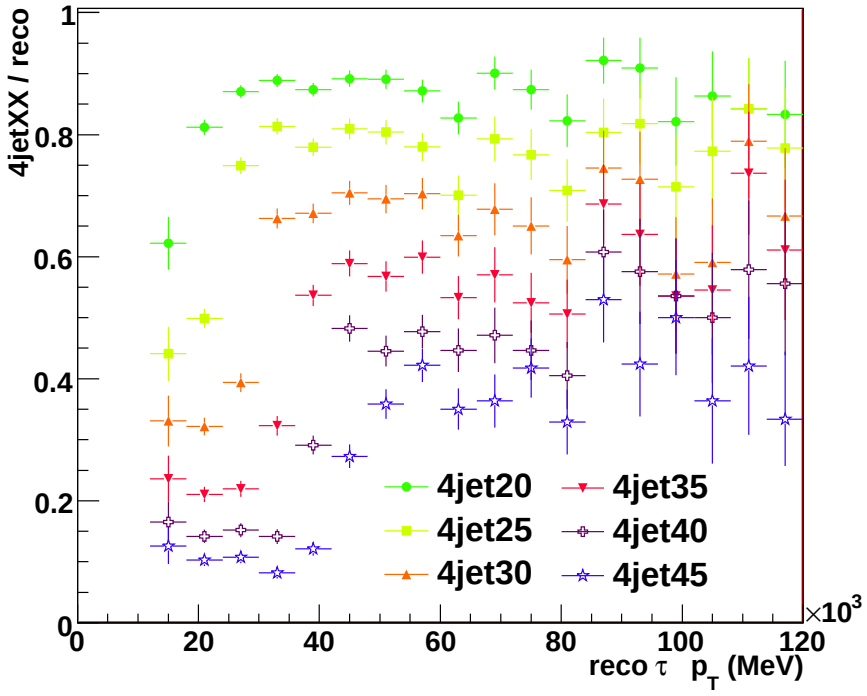

Figure 4.23: Ratio of $t\bar{t}$ events that pass a four jet trigger and all $t\bar{t}$ events, normalized to the events that pass the $t\bar{t}$ event selection, for different jet p_T thresholds.

Tau triggers (in combination with $\not\!\!E_T$ or b triggers) yield lower efficiencies compared to multijet triggers, but they complement them. The OR combination of all trigger menus shown in Table 4.14 yields a total efficiency of 95%.

Finally, Figure 4.26 shows the overlap between the different menus considered. It shows a large overlap between tau and multijet triggers, what will be useful to commission the trigger and to determine trigger efficiencies from data.

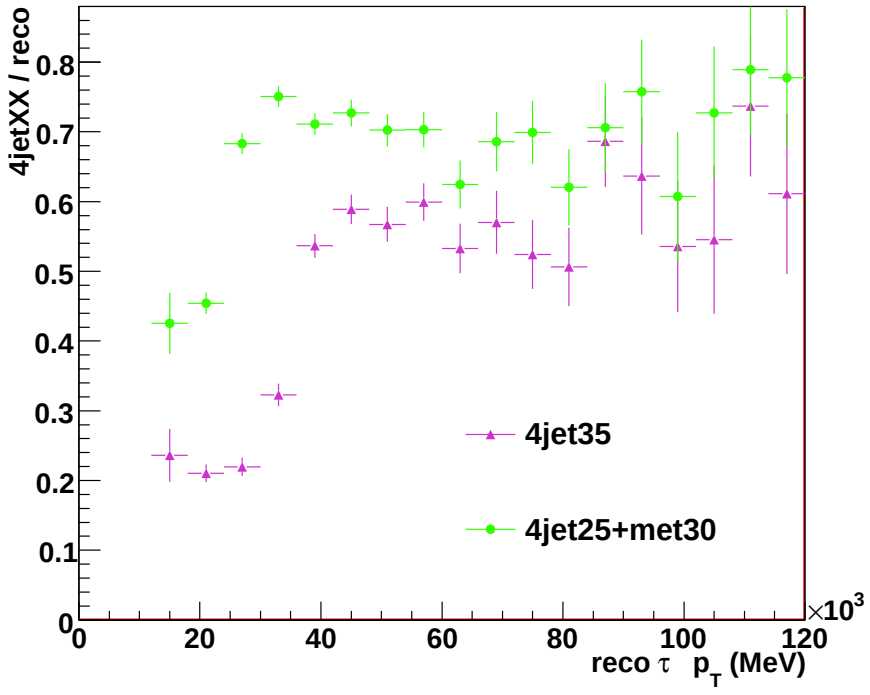

Figure 4.24: Ratio of $t\bar{t}$ events that pass a trigger menu and all $t\bar{t}$ events, normalized to the events that pass the $t\bar{t}$ event selection, for the trigger menus 4j35 and 4j25_xe30.

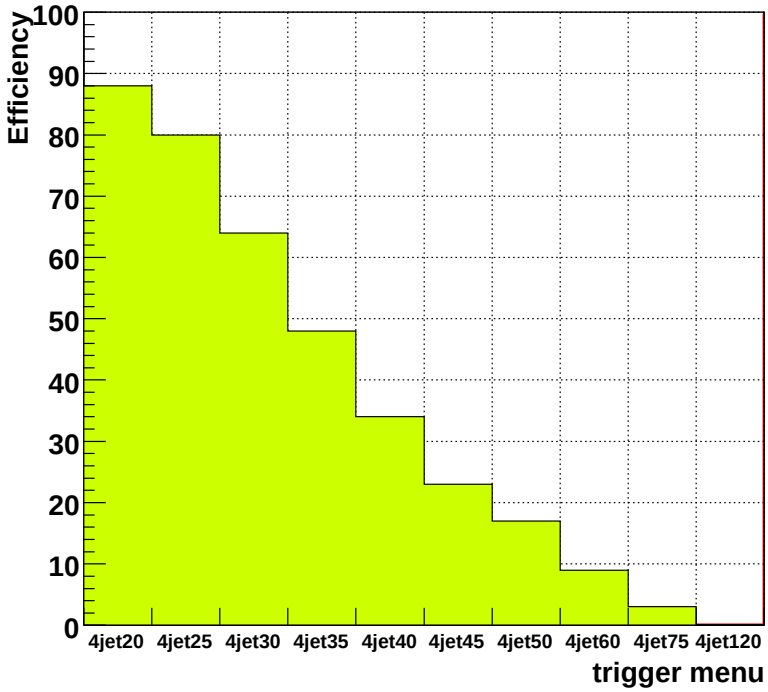

Figure 4.25: Trigger efficiencies of $t\bar{t}$ events for different four jet trigger menus. Efficiencies correspond to the last, Event Filter, trigger level and are normalized to events passing the $t\bar{t}$ event selection.

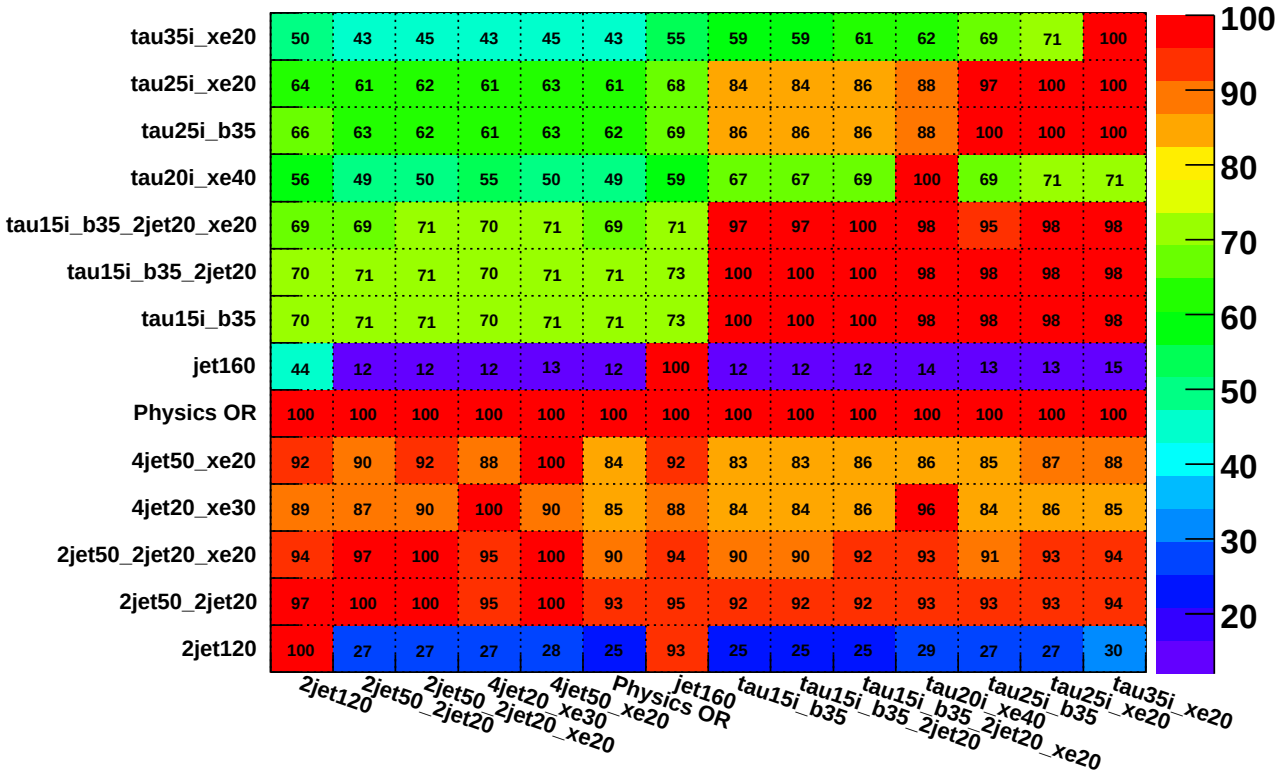

Figure 4.26: Trigger menus overlap for different menus evaluated for $t\bar{t}$ events. The event sample considered is composed only by the events that have passed the offline event selection. Percentage number at each bin shows the efficiency of passing the menu on the ordinate axis having previously passed the menu on the abscisa divided by the number of events having passed the menu on the abscissa.

4.11 Electron Channel

The experimental value of the branching ratio of a W boson decaying into an electron, $(10.75 \pm 0.13) \times 10^{-2}$, is almost equal to the branching ratio of decaying into a τ lepton, $(11.25 \pm 0.20) \times 10^{-2}$. The Standard Model does not make any difference between the two leptons while some models, like Supersymmetry, may favor in some regions of the parameters space the decay into τ leptons rather than electrons. In those models, the τ physics is generally quite different from that of electrons and muons.

Within the Standard Model hypothesis, the branching ratio between the electron (or muon) channel and the τ channel must be $r_\tau = \frac{t\to\tau\nu b}{t\to l\nu b} = 1$. Applying exactly the same event selection of the τ analysis to the electron channel, the branching ratio can be measured by just applying corrections due to the τ and electron (or muon) efficiencies (without the need to correct for the rest of cuts of the event selection). Any deviation of the experimental branching ratio r_τ from 1 would be an indication of presence of new physics at the TeV scale.

The only modification in the event selection with respect to the τ channel concerns the lepton identification and, of course, the lepton veto. The electron identification is based on the flag isEM (that corresponds to an optimized set of cuts on variables suitable for electron/gamma identification, see Section 3.3.2) and a cut on the isolation variable such that the transverse energy in a cone of size $\Delta R < 0.2$ around the electron object is not greater than 10 GeV.

The lepton veto criteria is restricted to the absence of an identified muon with p_T greater than 20 GeV.

Therefore, the full event selection for the electron channel is:

- $\not\!\!E_T$ should be larger than 35 GeV.
- At least 2 light jets (with $p_T > 20$ GeV).
- An identified electron with $p_T > 25$ GeV.
- At least 2 b-jets (with $p_T > 20$ GeV).
- No identified muon (with transverse momentum larger than 20 GeV) should be present in the event.
- The angular distance between the two selected b-jets, $\Delta R(\mathrm{b}, \bar{\mathrm{b}})$, should be larger than 1.
- The azimuthal angle between the missing momentum and the b-jet on the hadronic side, $\Delta\phi(\not\!\!p_T, B)$, should be larger than 0.5
- The minimum of the azimuthal angles between the missing momentum and the 3 leading jets in the event should be larger than 0.8

Due to the large rejection factor achieved by the electron identification algorithm, that is at least one order of magnitude larger than that of the tau algorithm, the fake rate in the

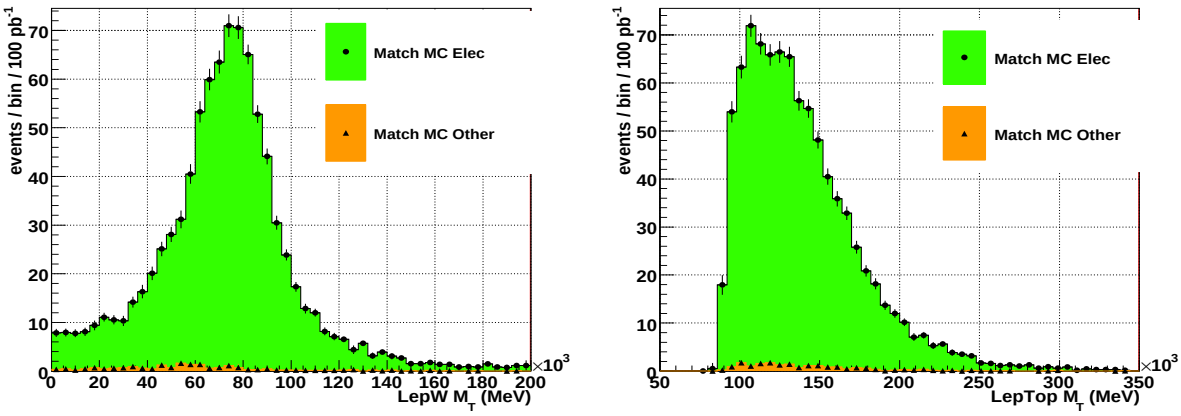

Figure 4.27: Distribution of the leptonic W (left) and top (right) transverse masses, normalized to an integrated luminosity of 100 pb^{-1}, computed as a combination of a reconstructed electron and missing transverse energy from Eq. 4.2. Each reconstructed electron was matched to a MC object, to investigate its origing. Cumulative distributions show reconstructed electrons matched to true electrons (green solid circles) and matched any other MC object (orange upward solid triangles).

electron sample of $t\bar{t}$ events is very small compared to that of the τ channel. Figure 4.27 shows the leptonic transverse masses reconstructed according to Equation 4.2 in the electron channel, normalized to an integrated luminosity of 100 pb^{-1}. Distributions show an insignificant amount of electron fakes, being the electron purity 97.8% (compared with the amount of tau fakes in the tau channel, 40%, as shown in Figure 4.9).

The expected number of events in the electron channel for 100 pb^{-1} is shown in Table 4.15 and the reconstructed invariant mass distributions of the hadronic side are presented in Figure 4.28. Due to lack of statistics in full simulation, QCD multijet processes were not included in this analysis. On the other hand the performance of the electron algorithm in the fast simulation was far from being comparable to that of the full simulation in order to estimate the QCD background for the electron channel. However, if in the τ channel QCD was shown to be under control (see Section 4.4) being the jet rejection of the τ identification algorithm at least one order of magnitude below the corresponding to the electron algorithms, there are good reasons to assume that the QCD process is not a problem for the electron channel analysis.

As expected, the analysis applied to the electron channel produces more signal events (about a factor 4) and larger S/B (about a factor 2) compared to the τ channel due to the higher lepton identification efficiency and jet rejection. The larger statistics of signal events (and lower presence of background events) in the electron channel may be used to understand and cross-check the invariant mass distributions of the hadronic side of the τ channel for which the limited statistics produces roughen distributions for 100 pb^{-1}.

Although the uncertainties on the cross section evaluation were not explicitely computed for this channel, one may expect lower values compared to the τ channel (Section 4.7). The

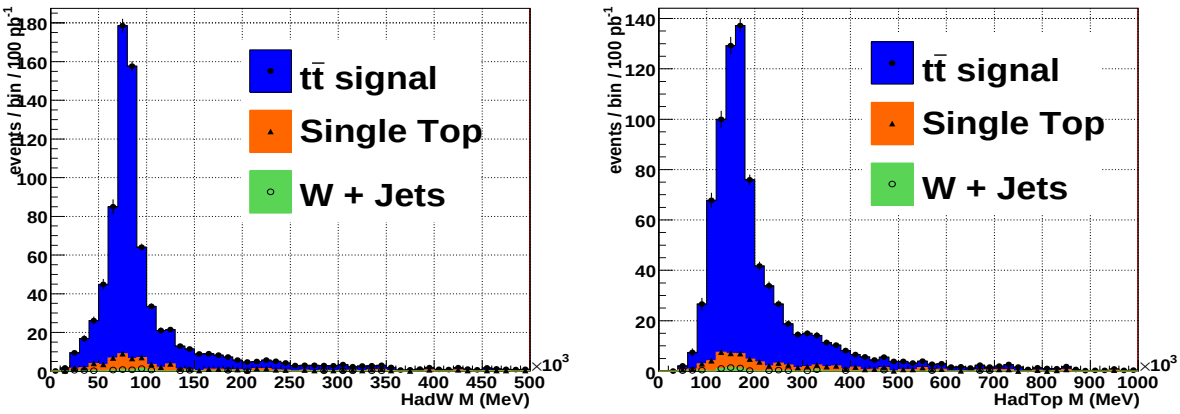

Figure 4.28: Invariant masses for hadronic W and hadronic top, reconstructed in the electron channel with the *Highest Jets - Highest b-Jet* strategy (see Section 4.2) after applying the full event selection. Plots are normalized to an integrated luminosity of 100 pb^{-1}. Distributions are shown in cumulative histograms for the different samples: W plus jets (open crosses), single top (upward triangles) and $t\bar{t}$ signal (circles). The hadronic $t\bar{t}$ sample is not shown in the plots for it has a negligible contribution to the total number of events. Errors shown for the sum of all the contributions are computed from the full statistics available in the simulation (Table 3.1).

statistical term of equation 4.4 is reduced to 3.5% due to the larger number of events that pass the event selection. Assuming the background can be estimated with a 20% uncertainty, this results in an uncertainty of the cross section of the electron channel of $\sim$ 2%. The systematics uncertainties that affect the electron channel will be similar to that of the τ channel except for the electron identification (as both analyses use the same event selection but for the lepton identification), for which lower uncertainties are expected compared to the 6% uncertainty due to the τ identification. Finally, the cross section uncertainty due to the luminosity, PDFs and ISR/FSR uncertainties should not change with respect to the analysis on the τ channel.

Table 4.15: Number of events remaining after each selection cut on the electron channel for signal and SM background samples, using a loose b-tagging selection for 100 pb^{-1}. The rightmost column shows the signal over background ratio. Errors quoted in this table correspond to the available MC statistics for a given sample (see Table 3.1). Numbers in parentheses are the S/B ratio for the each background.

	N_{evt} (100 pb^{-1})		
	Non hadronic $t\bar{t}$	**Hadronic $t\bar{t}$**	**Single top**
no cut	4.500e+4 +- 6e+1	3.852e+4 +- 1.4e+2 [1.2]	1.122e+4 +- 5e+1 [4.0]
$\not{E}_T > 35$ GeV	3.500e+4 +- 5e+1	4.86e+3 +- 5e+1 [7.2]	8.13e+3 +- 5e+1 [4.3]
# of Light Jets > 1	3.036e+4 +- 5e+1	4.80e+3 +- 5e+1 [6.3]	6.25e+3 +- 4e+1 [4.9]
El $p_T > 25000$	5726 +- 21	52 +- 6 [1.1e+2]	909 +- 16 [6.3]
# B Jets > 0	4687 +- 19	42 +- 5 [1.1e+2]	583 +- 12 [8.0]
# B Jets > 1	2004 +- 12	21 +- 4 [95]	146 +- 6 [14]
μ veto	1751 +- 12	19 +- 4 [92]	138 +- 6 [13]
ΔR b Jets > 1.0	1630 +- 11	18 +- 4 [91]	127 +- 6 [13]
$\Delta\phi(\not{p}_T, B) > 0.5$	1486 +- 11	13 +- 3 [1.1e+2]	113 +- 6 [13]
min $\Delta\phi(\not{E}_T$,jets) > 0.8	745 +- 8	2.6 +- 1.7 [2.9e+2]	65 +- 4 [11]

	N_{evt} (100 pb^{-1})	
	W+jet	**S/B**
no cut	2.415e+4 +- 7e+1 [1.9]	0.6
$\not{E}_T > 35$ GeV	1.518e+4 +- 6e+1 [2.3]	1.2
# of Light Jets > 1	1.477e+4 +- 6e+1 [2.1]	1.2
El $p_T > 25000$	5.85e+3 +- 4e+1 [0.98]	0.8
# B Jets > 0	517 +- 14 [9.1]	4
# B Jets > 1	27 +- 4 [74]	10
μ veto	26 +- 4 [67]	9.6
ΔR b Jets > 1.0	22 +- 4 [74]	9.8
$\Delta\phi(\not{p}_T, B) > 0.5$	22 +- 4 [68]	10
min $\Delta\phi(\not{E}_T$,jets) > 0.8	7.4 +- 2.2 [1.0e+2]	10

Chapter 5

Summary

The analysis presented shows the feasibility of a $t\bar{t} \rightarrow W(qq')W(\tau_{had}\nu)b\bar{b}$ cross section measurement with early data. Considering that a good understanding of the b-tagging identification may take some time (to calibrate, extract the likelihoods, etc) the analysis made use of a loose b-tagging selection, where the light jet rejection was about a factor 2 from its optimum value. The other two main ingredients of the analysis are the τ identification and the measurement of the missing transverse energy.

After the basic event selection is applied, the full $t\bar{t}$ event is reconstructed yielding two invariant masses on the hadronic side and two transverse masses on the leptonic side, corresponding to the top quarks and the W bosons. Finally to further reject the SM background (specially QCD) some cuts on topological variables were introduced.

The Monte Carlo for signal and background samples was generated with a detailed GEANT4 simulation of the ATLAS detector and with statistics enough for the 100 pb^{-1} luminosity scenario, except for QCD, for which, due to the large amount of events needed to cover that integrated luminosity a fast simulation has been used instead. Performance of τ and b-tagging identifications that do not agree with the full simulation were corrected.

The result of the analysis for 100 pb^{-1} of data yields 272 events with a τ purity of 60% for signal events. The S/B evaluated with all the SM backgrounds is about 4. The analysis was also prepared for 1 fb^{-1} of data yielding in this case 1330 ± 30 events with a S/B of about 8.

The contribution of new physics was studied in the case of the MSSM, considering several benchmark points of the mSUGRA model. Results show that the signature of the SUSY events is quite similar to that of the $t\bar{t}$ events, and therefore the analysis does not reject them. If the SUSY process has a large enough cross section as it is the case for the so called SU4 point, the new physics will contribute with a number of events of the same order of magnitude as the signal. Nevertheless SUSY events can still be distinguished as they will produce large $\not\!\!E_T$ tails compared to $t\bar{t}$.

To trigger the $t\bar{t} \rightarrow W(qq')W(\tau_{had}\nu)b\bar{b}$ events, several trigger menus were studied. The physics combination of all the triggers considered yields an efficiency of 95%.

The cross section of $t\bar{t} \rightarrow W(qq')W(\tau_{had}\nu)b\bar{b}$ can be estimated for 100 pb^{-1} with an expected

accuracy of

$$\frac{\Delta\sigma}{\sigma} = (6(\text{stat}) \pm 4(\text{bkg}) \pm 16(\text{sys}) \pm 5(\text{lumi}))\,\% \tag{5.1}$$

Once more data are acumulated and the detector better understood not only the statistical uncertainty but also the systematic uncertainty will be reduced.

Appendices

Appendix A

Event Selection for All Strategies

In the reconstruction of the $t\bar{t}$ event, four different strategies were studied to build the hadronic top and hadronic W boson from the basic particles identified in the detector: jets and b-jets. The strategies, so called *BestPDG - Closest* ΔR, *Highest Jets - Highest b-Jet*, *Highest composite particle* and *Highest composite (build hadronic top first)* were explained in detail in Section 4.2. The results shown in the document are based on the *Highest Jets - Highest b-Jet* strategy, chosen as the default strategy. This appendix presents a full comparison among the four strategies.

Figure A.1 shows the invariant mass for the hadronic top and W boson and the transverse mass for the leptonic top and W boson (even if the strategy is defined to build the hadronic side, the leptonic side will be indirectly affected by the selection, for a b-jet already chosen to form a hadronic top can not be considered in the leptonic side), for three strategies. The strategy *Highest composite (build hadronic top first)* is not present in the figure as its distributions follow very similar shapes to the *Highest composite* strategy.

The *BestPDG - Closest* ΔR strategy has the narrower distributions in the hadronic invariant masses, but introduces a bias in the distributions of the background (the combinatorial background and the physical background have the same Gaussian shape as the $t\bar{t}$ signal) that implies a loss of information crucial to determine the amount of background present in data (see Section 4.8). Although the rest of the strategies have similar behaviours, the *Highest Jets - Highest b-Jet* strategy has slightly spread hadronic invariant mass distributions. The most notable difference between the *Highest Jets - Highest b-Jet* and the *Highest composite particle* strategies is the p_T spectrum of the hadronic top and W boson (Figure A.2), higher in the *Highest composite particle* strategy with a shift of about 30 GeV in the hadronic top p_T compared to the *Highest Jets - Highest b-Jet* strategy.

Even if the reconstruction of the leptonic transverse masses might depend on the strategy selected to build the hadronic side of the event (for one b-jet that is selected as coming from the b quark decaying from the hadronic top will not be considered to compose the leptonic top), the bottom plots of Figure A.1 show that the distributions of the leptonic transverse masses are quite independent on the hadronic reconstruction strategy.

The expected number of events for each strategy with 100 pb^{-1} of data is summarized in

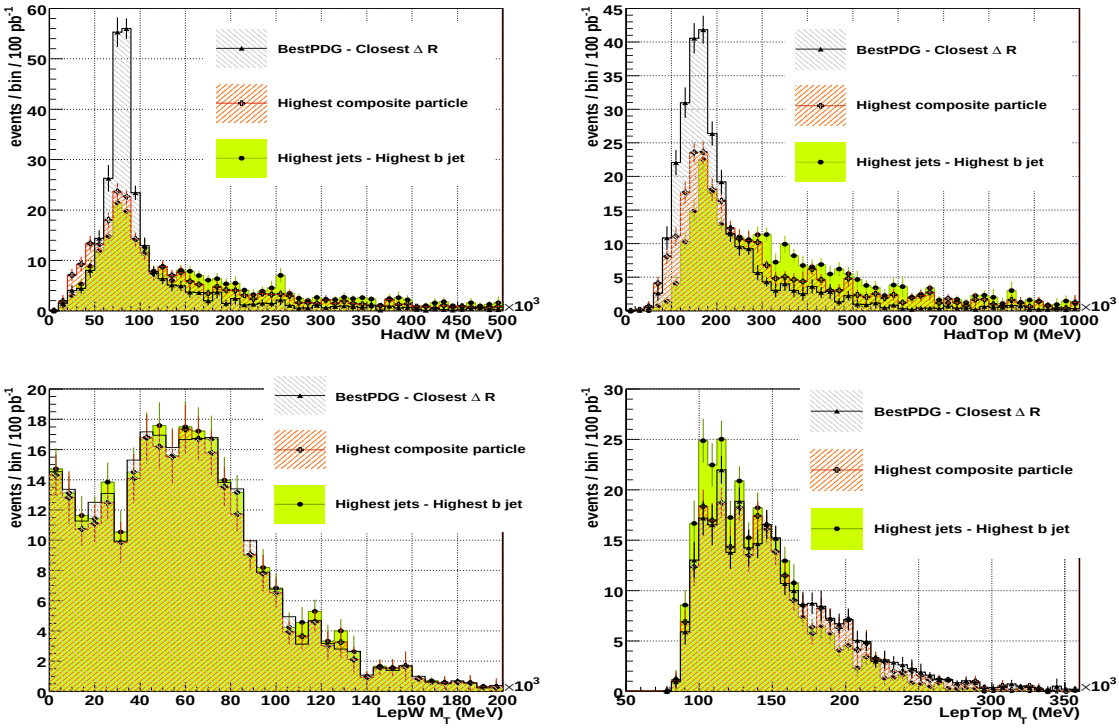

Figure A.1: Invariant masses for hadronic W, hadronic top, leptonic W and leptonic top, reconstructed with three different strategies: *Highest Jets - Highest b-Jet* (circles), *Highest composite particle* (open crosses) and *BestPDG - Closest* ΔR (triangles) -see Section 4.2-, after applying the full event selection. Distributions show the contribution of the $t\bar{t}$ signal plus the SM background for an integrated luminosity of 100 pb^{-1}. Errors shown for the sum of all the contributions are computed from the full statistics available in the simulation (Table 3.1).

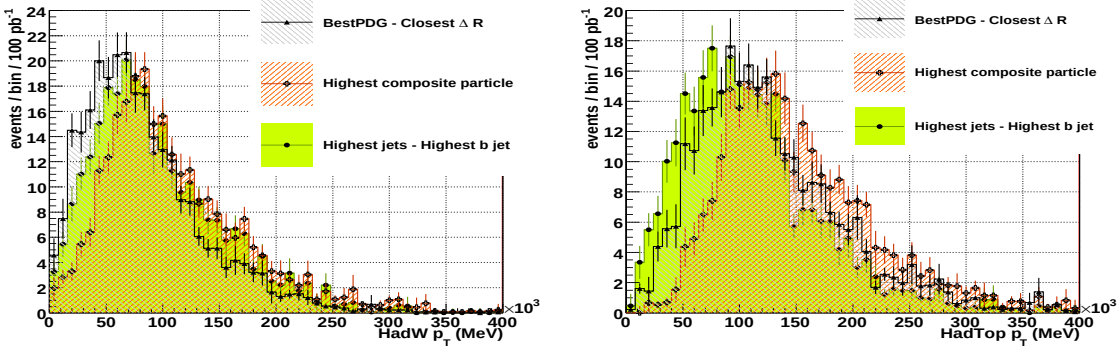

Figure A.2: p_T spectra of hadronic W and hadronic top, reconstructed with three different strategies: *Highest Jets - Highest b-Jet* (circles), *Highest composite particle* (open crosses) and *BestPDG - Closest* ΔR (triangles) -see Section 4.2-, after applying the full event selection. Distributions show the contribution of the $t\bar{t}$ signal plus the SM background for an integrated luminosity of 100 pb^{-1}. Errors shown for the sum of all the contributions are computed from the full statistics available in the simulation (Table 3.1).

Tables A.1, A.2 and A.3 (results for the default strategy *Highest Jets - Highest b-Jet* were already presented at Table 4.2 in the document). Although the number of expected events may vary slightly for the $t\bar{t}$ signal among the different strategies, the S/B ratio is about 4 in all the cases.

Table A.1: Number of events remaining after each selection requirement, for signal and Standard Model background samples, using a loose b-tagging selection for 100 pb^{-1} and the *BestPDG - Closest* ΔR strategy to reconstruct the hadronic W boson and top. The rightmost column shows the signal over background ratio. QCD simulation includes a filter requiring at least 2 identified jets and $\not\!\!E_T > 20$ GeV to increase the generation efficiency. Therefore, no expected number of events for the first cuts are shown in the table. Errors quoted in this table correspond to the available MC statistics for each given sample (see Table 3.1). Numbers in parentheses are the S/B ratio for the each background.

	N$_{evt}$ (100 pb^{-1})		
	Non hadronic $t\bar{t}$	**Hadronic $t\bar{t}$**	**Single top**
no cut	4.500e+4 +- 6e+1	3.852e+4 +- 1.4e+2 [1.2]	1.122e+4 +- 5e+1 [4.0]
$\not\!\!E_T > 35$ GeV	3.500e+4 +- 5e+1	4.86e+3 +- 5e+1 [7.2]	8.13e+3 +- 5e+1 [4.3]
# of Light Jets > 1	2.984e+4 +- 5e+1	4.79e+3 +- 5e+1 [6.2]	6.11e+3 +- 4e+1 [4.9]
τ $p_T > 25$ GeV/c	2161 +- 13	231 +- 12 [9.4]	323 +- 9 [6.7]
# B Jets > 0	1739 +- 12	208 +- 11 [8.4]	199 +- 7 [8.7]
# B Jets > 1	692 +- 7	106 +- 8 [6.5]	45 +- 4 [15]
e veto	622 +- 7	100 +- 8 [6.2]	42 +- 4 [15]
μ veto	484 +- 6	81 +- 7 [6.0]	35 +- 3 [14]
ΔR b Jets > 1.0	452 +- 6	77 +- 7 [5.9]	33 +- 3 [14]
$\Delta\phi(\not\!\!p_T, \mathrm{B}) > 0.5$	420 +- 6	53 +- 6 [7.9]	30 +- 3 [14]
min $\Delta\phi(\not\!\!E_T$,jets) > 0.8	206 +- 4	16 +- 3 [13]	14.4 +- 2.2 [14]

	N$_{evt}$ (100 pb^{-1})		
	W+jet	**QCD**	**S/B**
no cut	1992 +- 14 [23]	-	-
$\not\!\!E_T > 35$ GeV	1219 +- 11 [29]	-	-
# of Light Jets > 1	784 +- 9 [38]	-	-
τ $p_T > 25$ GeV/c	32.6 +- 1.9 [66]	-	-
# B Jets > 0	19.2 +- 1.5 [91]	-	-
# B Jets > 1	4.33 +- 0.82 [1.6e+2]	169 +- 8 [4.1]	2.1
e veto	4.33 +- 0.82 [1.4e+2]	169 +- 8 [3.7]	2.0
μ veto	4.05 +- 0.81 [1.2e+2]	169 +- 8 [2.9]	1.7
ΔR b Jets > 1.0	3.20 +- 0.74 [1.4e+2]	151 +- 8 [3.0]	1.7
$\Delta\phi(\not\!\!p_T, \mathrm{B}) > 0.5$	3.11 +- 0.73 [1.4e+2]	106 +- 7 [4.0]	2.2
min $\Delta\phi(\not\!\!E_T$,jets) > 0.8	1.40 +- 0.56 [1.5e+2]	22 +- 3 [9.4]	3.8

Table A.2: Number of events remaining after each selection requirement, for signal and Standard Model background samples, using a loose b-tagging selection for 100 pb^{-1} and the *Highest composite particle* strategy to reconstruct the hadronic W boson and top. The rightmost column shows the signal over background ratio. QCD simulation includes a filter requiring at least 2 identified jets and $\not\!\!E_T > 20$ GeV to increase the generation efficiency. Therefore, no expected number of events for the first cuts are shown in the table. Errors quoted in this table correspond to the available MC statistics for each given sample (see Table 3.1). Numbers in parentheses are the S/B ratio for the each background.

	N_{evt} (100 pb^{-1})		
	Non hadronic $t\bar{t}$	**Hadronic $t\bar{t}$**	**Single top**
no cut	4.500e+4 +- 6e+1	3.852e+4 +- 1.4e+2 [1.2]	1.122e+4 +- 5e+1 [4.0]
$\not\!\!E_T > 35$ GeV	3.500e+4 +- 5e+1	4.86e+3 +- 5e+1 [7.2]	8.13e+3 +- 5e+1 [4.3]
# of Light Jets > 1	2.984e+4 +- 5e+1	4.79e+3 +- 5e+1 [6.2]	6.11e+3 +- 4e+1 [4.9]
τ $p_T > 25$ GeV/c	2175 +- 13	232 +- 12 [9.4]	324 +- 9 [6.7]
# B Jets > 0	1751 +- 12	209 +- 11 [8.4]	199 +- 7 [8.8]
# B Jets > 1	697 +- 7	106 +- 8 [6.6]	46 +- 4 [15]
e veto	626 +- 7	100 +- 8 [6.3]	42 +- 4 [15]
μ veto	488 +- 6	81 +- 7 [6.0]	35 +- 3 [14]
ΔR b Jets > 1.0	457 +- 6	77 +- 7 [5.9]	33 +- 3 [14]
$\Delta\phi(\not\!\!p_T, B) > 0.5$	437 +- 6	59 +- 6 [7.4]	32 +- 3 [14]
min $\Delta\phi(\not\!\!E_T$,jets) > 0.8	210 +- 4	17 +- 4 [12]	15.5 +- 2.3 [14]

	N_{evt} (100 pb^{-1})		
	W+jet	**QCD**	**S/B**
no cut	1992 +- 14 [23]	-	-
$\not\!\!E_T > 35$ GeV	1219 +- 11 [29]	-	-
# of Light Jets > 1	784 +- 9 [38]	-	-
τ $p_T > 25$ GeV/c	32.8 +- 2.0 [66]	-	-
# B Jets > 0	19.4 +- 1.5 [90]	-	-
# B Jets > 1	4.51 +- 0.84 [1.5e+2]	45 +- 5 [15]	3.4
e veto	4.51 +- 0.84 [1.4e+2]	20 +- 3 [31]	3.8
μ veto	4.05 +- 0.81 [1.2e+2]	20 +- 3 [24]	3.5
ΔR b Jets > 1.0	3.20 +- 0.74 [1.4e+2]	20 +- 3 [23]	3.4
$\Delta\phi(\not\!\!p_T, B) > 0.5$	3.20 +- 0.74 [1.4e+2]	18 +- 3 [24]	3.9
min $\Delta\phi(\not\!\!E_T$,jets) > 0.8	1.50 +- 0.57 [1.4e+2]	14.8 +- 2.9 [14]	4.3

Table A.3: Number of events remaining after each selection requirement, for signal and Standard Model background samples, using a loose b-tagging selection for 100 pb^{-1} and the *Highest composite particle (build hadronic top first)* strategy to reconstruct the hadronic W boson and top. The rightmost column shows the signal over background ratio. QCD simulation includes a filter requiring at least 2 identified jets and $\not\!\!E_T > 20$ GeV to increase the generation efficiency. Therefore, no expected number of events for the first cuts are shown in the table. Errors quoted in this table correspond to the available MC statistics for each given sample (see Table 3.1). Numbers in parentheses are the S/B ratio for the each background.

	N_{evt} (100 pb^{-1})		
	Non hadronic $t\bar{t}$	**Hadronic $t\bar{t}$**	**Single top**
no cut	4.500e+4 +- 6e+1	3.852e+4 +- 1.4e+2 [1.2]	1.122e+4 +- 5e+1 [4.0]
$\not\!\!E_T > 35$ GeV	3.500e+4 +- 5e+1	4.86e+3 +- 5e+1 [7.2]	8.13e+3 +- 5e+1 [4.3]
# of Light Jets > 1	2.984e+4 +- 5e+1	4.79e+3 +- 5e+1 [6.2]	6.11e+3 +- 4e+1 [4.9]
τ $p_T > 25$ GeV/c	2175 +- 13	232 +- 12 [9.4]	324 +- 9 [6.7]
# B Jets > 0	1751 +- 12	209 +- 11 [8.4]	199 +- 7 [8.8]
# B Jets > 1	697 +- 7	106 +- 8 [6.6]	46 +- 4 [15]
e veto	626 +- 7	100 +- 8 [6.3]	42 +- 4 [15]
μ veto	488 +- 6	81 +- 7 [6.0]	35 +- 3 [14]
ΔR b Jets > 1.0	457 +- 6	77 +- 7 [5.9]	33 +- 3 [14]
$\Delta\phi(\not\!\!p_T, \mathrm{B}) > 0.5$	442 +- 6	61 +- 6 [7.2]	32 +- 3 [14]
min $\Delta\phi(\not\!\!E_T$,jets) > 0.8	213 +- 4	20 +- 4 [11]	15.5 +- 2.3 [14]

	N_{evt} (100 pb^{-1})		
	W+jet	**QCD**	**S/B**
no cut	1992 +- 14 [23]	-	-
$\not\!\!E_T > 35$ GeV	1219 +- 11 [29]	-	-
# of Light Jets > 1	784 +- 9 [38]	-	-
τ $p_T > 25$ GeV/c	32.8 +- 2.0 [66]	-	-
# B Jets > 0	19.4 +- 1.5 [90]	-	-
# B Jets > 1	4.51 +- 0.84 [1.5e+2]	45 +- 5 [15]	3.5
e veto	4.51 +- 0.84 [1.4e+2]	20 +- 3 [31]	3.8
μ veto	4.05 +- 0.81 [1.2e+2]	20 +- 3 [24]	3.5
ΔR b Jets > 1.0	3.20 +- 0.74 [1.4e+2]	20 +- 3 [23]	3.4
$\Delta\phi(\not\!\!p_T, \mathrm{B}) > 0.5$	3.20 +- 0.74 [1.4e+2]	18 +- 3 [25]	3.9
min $\Delta\phi(\not\!\!E_T$,jets) > 0.8	1.50 +- 0.57 [1.4e+2]	14.8 +- 2.9 [14]	4.1

Bibliography

[1] S. L. Glashow. *Partial-symmetries of weak interactions.* Nucl. Phys., **22**:579–88, 1961. http://www.osti.gov/energycitations/product.biblio.jsp?osti_id=4082455.

[2] S. Weinberg. *A model of leptons.* Phys. Rev. Lett., **19**(21):1264–1266, 1967. http://prola.aps.org/abstract/PRL/v19/i21/p1264_1.

[3] A. Salam. *Elementary Particle Physics Theory.* ed. N. Svartholm, Almqvist and Wiksell, Stockholm, page 367, 1968.

[4] J. Iliopoulos S. L. Glashow and L. Maiani. *Weak interactions with lepton - hadron symmetry.* Phys. Rev., **D2**:1285–1292, 1970.

[5] LEP Electroweak Working Group. http://lepewwg.web.cern.ch/LEPEWWG/Welcome.html.

[6] C. Amsler et al. (Particle Data Group). Phys. Lett. B667, 2008.

[7] Albert Einstein. *On the electrodynamics of moving bodies.* Annalen Phys., **17**:891–921, 1905.

[8] P. A. M. Dirac. *The Quantum Theory of the Electron.* Proceedings of the Royal Society of London A, **117**:610–624.

[9] E. Noether. *Invariante Variationsprobleme.* Nachr. D. König. Gesellsch. D. Wiss. Zu Göttingen, pages 235–257, 1918. http://www.physics.ucla.edu/ cwp/articles/noether.trans/english/mort186.html.

[10] H. David Politzer. *Reliable Perturbative Results for Strong Interactions?* Phys. Rev. Lett., **30**:1346–1349, 1973.

[11] G. Arnison et al. *Experimental observation of isolated large transverse energy electrons with associated missing energy at $\sqrt{s}$ = 540 GeV.* Phys. Lett., **B122**:103–116, 1983.

[12] G. Arnison et al. *Experimental observation of lepton pairs of invariant mass around 95* GeV/c^2 *at the CERN SPS collider.* Phys. Lett., **B126**:398–410, 1983.

[13] M. Banner et al. *Observation of single isolated electrons of high transverse momentum in events with missing transverse energy at the CERN anti-p p collider.* Phys. Lett., **B122**:476–485, 1983.

[14] P.W. Higgs. Phys. Rev. Lett., **13**:508–509, 1964.

[15] F. Englert and R. Brout. *Broken symmetry and the mass of the gauge vector mesons*. Phys. Rev. Lett., **13**:321–322, 1964.

[16] D. Ross. *Foundations of the Standard Model*. Prepared for 57th Scottish Universties Summer School in Physics: LHC Phenomenology (SUSSP 2003), St. Andrews, Scotland, United Kingdom, 17-29 Aug 2003.

[17] L. D. Faddeev and V. N. Popov. *Feynman diagrams for the Yang-Mills field*. Phys. Lett., **B25**:29–30, 1967.

[18] Nicola Cabibbo. *Unitary Symmetry and Leptonic Decays*. Phys. Rev. Lett., **10**:531–533, 1963. http://prola.aps.org/abstract/PRL/v10/i12/p531_1.

[19] Makoto Kobayashi and Toshihide Maskawa. *CP Violation in the Renormalizable Theory of Weak Interaction*. Prog. Theor. Phys., **49**:652–657, 1973. http://ptp.ipap.jp/link?PTP/49/652.

[20] Siegfried Bethke. *Experimental Tests of Asymptotic Freedom*. Prog. Part. Nucl. Phys., **58**:351–386, 2007.

[21] George Sterman and Steven Weinberg. *Jets from Quantum Chromodynamics*. Phys. Rev. Lett., **39**:1436, 1977.

[22] Benjamin W. Lee, C. Quigg, and H. B. Thacker. *Weak Interactions at Very High-Energies: The Role of the Higgs Boson Mass*. Phys. Rev., **D16**:1519, 1977.

[23] R. Barate et al. *Search for the standard model Higgs boson at LEP*. Phys. Lett., **B565**:61–75, 2003.

[24] S. Abachi et al. *Observation of the top quark*. Phys. Rev. Lett., **74**:2632–2637, 1995.

[25] F. Abe et al. *Observation of top quark production in $\bar{p}p$ collisions*. Phys. Rev. Lett., **74**:2626–2631, 1995.

[26] *A Combination of CDF and D0 Results on the Mass of the Top Quark*. 2008. http://arxiv.org/abs/0803.1683.

[27] Sven Moch and Peter Uwer. *Theoretical status and prospects for top-quark pair production at hadron colliders*. Phys. Rev., **D78**:034003, 2008.

[28] W. K. Tung et al. *Heavy quark mass effects in deep inelastic scattering and global QCD analysis*. JHEP, **02**:053, 2007.

[29] R.S. Thorne A.D. Martin, W.J. Stirling and G. Watt. *Update of Parton Distributions at NNLO*. Phys. Lett. B, **652**:292, 2007. http://arxiv.org/abs/0706.0459.

[30] Nikolaos Kidonakis and Ramona Vogt. *The theoretical top quark cross section at the Tevatron and the LHC*. Physical Review D, **78**:074005, 2008. http://arxiv.org/abs/0805.3844.

[31] T. Aaltonen et al. *First Observation of Electroweak Single Top Quark Production*. 2009.

[32] V. M. Abazov et al. *Observation of Single Top Quark Production*. 2009.

[33] V. M. et al. Abazov. *Evidence for production of single top quarks*. Phys. Rev., **D78**:012005, 2008.

[34] The CDF Collaboration. *Combination of CDF Single Top Quark Searches with 2.2 fb-1 of Data*. CDF Note 9251, Marc 2008.

[35] Nikolaos Kidonakis. *Higher-order soft gluon corrections in single top quark production at the LHC*. Physical Review D, **75**:071501, 2007. http://arxiv.org/abs/hep-ph/0701080.

[36] A. D. Martin, R. G. Roberts, W. J. Stirling, and R. S. Thorne. *Physical gluons and high-E(T) jets*. Phys. Lett., **B604**:61–68, 2004.

[37] Edward Witten. *Dynamical Breaking of Supersymmetry*. Nucl. Phys., **B188**:513, 1981.

[38] Romesh K. Kaul. *Gauge hierarchy in a supersymmetric model*. Phys. Lett., **B109**:19–24, 1982.

[39] Pis'ma Zh. Eksp. Tear. Fiz. Gol'fand Yu A, Likhtman E P. JETP Lett., **13**:323, 1971.

[40] D. V. Volkov and V. P. Akulov. *Is the Neutrino a Goldstone Particle?* Phys. Lett., **B46**:109–110, 1973.

[41] J. Wess and B. Zumino. *Supergauge Transformations in Four-Dimensions*. Nucl. Phys., **B70**:39–50, 1974.

[42] Michael Dine. *Supersymmetry and String Theory: Beyond the Standard Model*. Cambridge University Press, 2007.

[43] Savas Dimopoulos and Howard Georgi. *Softly Broken Supersymmetry and SU(5)*. Nucl. Phys., **B193**:150, 1981.

[44] ATLAS Collaboration. *Supersymmetry. Expected Performance of the ATLAS Experiment Detector, Trigger, Physics*. CERN-OPEN-2008-020, 2008.

[45] Ali H. Chamseddine, Richard L. Arnowitt, and Pran Nath. *Locally Supersymmetric Grand Unification*. Phys. Rev. Lett., **49**:970, 1982.

[46] Riccardo Barbieri, S. Ferrara, and Carlos A. Savoy. *Gauge Models with Spontaneously Broken Local Supersymmetry*. Phys. Lett., **B119**:343, 1982.

[47] Lawrence J. Hall, Joseph D. Lykken, and Steven Weinberg. *Supergravity as the Messenger of Supersymmetry Breaking.* Phys. Rev., **D27**:2359–2378, 1983.

[48] G. Aad et al. *The ATLAS Experiment at the CERN Large Hadron Collider.* JINST, **3**:S08003, 2008.

[49] A. Yamamoto et al. Nucl. Instrum. Meth., **A 584**:53, 2008.

[50] T.Sjstrand. Comput. Phys. Comm., **82**:74, 1994.

[51] F. Frixione and B. Webber. *Matching NLO QCD computations and parton shower simulations.* JHEP, **0206**(029), 2002. http://www.hep.phys.cam.ac.uk/theory/webber/MCatNLO/.

[52] R. Bonciani et al. *NLL resummation of the heavy-quark hadroproduction cross-section.* Nucl. Phys., page 424, 1998. http://citebase.org/cgi-bin/citations?id=oai:arXiv.org:hep-ph/9801375.

[53] B. P. Kersevan and R. W. Elzbieta. *The Monte Carlo Event Generator AcerMC version 3.4 with interfaces to PYTHIA 6.3, HERWIG 6.5 and ARIADNE 4.1.* arXiv, **hep-ph**(0405247), 2004.

[54] Z. Sullivan. *Understanding single-top-quark production and jets.* arXiv, **hep-ph**(0408049), 2004. http://arxiv.org/abs/hep-ph/0408049.

[55] J. Campbell and F. Tramontano. *Next-to-leading order corrections to Wt production and decay.* arXiv, **hep-ph**(0506289), 2005. http://xxx.lanl.gov/abs/hep-ph/0506289.

[56] L. M. Mangano. *Alpgen, a generator for hard multiparton process in hadronic collisions.* arXiv, **hep-ph**(0206293), 2002. http://arXiv.org/abs/hep-ph/0206293.

[57] R. K. Ellis J. Campbell and D. Rainwater. *Next-to-leading order QCD predictions for W+2 jet and Z+3 jet production at the CERN LHC.* arXiv, **hep-ph**(0308195), 2003.

[58] G. Corcella et al. *HERWIG 6.5: an event generator for Hadron Emission Reactions With Interfering Gluons (including supersymmetric processes).* JHEP, **01**:010, 2001.

[59] J. M. Butterworth, Jeffrey R. Forshaw, and M. H. Seymour. *Multiparton interactions in photoproduction at HERA.* Z. Phys., **C72**:637–646, 1996.

[60] A. Mesina B. Cooper and D. Waters. *Measurement of the inclusive* $W^{\pm} \rightarrow e^{\pm}\nu + n$ *jet cross section in* $p\bar{p}$ *collisions at* $\sqrt{s} = 1.96$ TeV. **CDF note**(8381), 2006.

[61] J. Alwall et al. *Comparative study of various algorithms for the merging of parton showers and matrix elements in hadronic collisions.* European Physical Journal C, **53**:473, 2008.

[62] S. Agostinelli et al. *GEANT4: A simulation toolkit.* Nucl. Instrum. Meth., **A506**:250–303, 2003.

[63] John Allison et al. *Geant4 developments and applications.* IEEE Trans. Nucl. Sci., **53**:270, 2006.

[64] D. Cavalli et al. *Performance of the ATLAS fast simulation* `ATLFAST`. ATLAS Notes, **ATL-COM-PHYS-2007-012**, 2007.

[65] K. Assamagan et al. *The ATLAS Monte Carlo Project.* ATL-COM-SOFT-2008-024.

[66] ATLAS Computing Group. *Technical design report.* ATLAS TDR, 2005. http://atlas.web.cern.ch/Atlas/GROUPS/PHYSICS/TDR/access.html.

[67] ATLAS Collaboration. *Tau Leptons. Expected Performance of the ATLAS Experiment Detector, Trigger, Physics.* CERN-OPEN-2008-020, 2008.

[68] W. Lampl et al. *Calorimeter Cluster Algorithms: Description and Performance.* ATLAS-LARG-PUB-2008-002, 2008.

[69] ATLAS Collaboration. *Detector level jet corrections. Expected Performance of the ATLAS Experiment Detector, Trigger, Physics.* CERN-OPEN-2008-020, 2008.

[70] G.C. et al Blazey. *Run II jet physics.* 2000. Preprint hep-ex/0005012v2.

[71] ATLAS Collaboration. *Expected Performance of the ATLAS Experiment Detector, Trigger, Physics.* CERN-OPEN-2008-020, 2008.

[72] ATLAS Collaboration. *b-tagging Calibration with $t\bar{t}$ Events. Expected Performance of the ATLAS Experiment Detector, Trigger, Physics.* CERN-OPEN-2008-020, 2008.

[73] ATLAS Collaboration. *The ATLAS Computing TDR.* 2004. http://atlas-proj-computing-tdr.web.cern.ch/atlas-proj-computing-tdr/PDF/Computing-TDR-final-July04.pdf.

[74] *parametrization provided by the b-tagging combined group.*

[75] A. Mapelli et al. *Development of a detector (ALFA) to measure the absolute LHC luminosity at ATLAS.* ATLAS Notes, **ATL-LUM-PUB-2007-006**, 2007.

[76] ATLAS Collaboration. *ATLAS Forward Detectors for Measurement of Elastic Scattering and Luminosity.* ATLAS TDR 18, **lhcc-2008-004**, 2008.

[77] ATLAS Collaboration. *Determination of the top quark pair production cross-section. Expected Performance of the ATLAS Experiment Detector, Trigger, Physics.* CERN-OPEN-2008-020, 2008.

[78] H. Baer et al. *A Monte Carlo Event Generator for pp, $p\bar{p}$ and e^+e^- Reactions.* http://www.hep.fsu.edu/isajet/.